CHEMICAL AND PHYSICAL BIOLOGY

# PHYSICAL BASIS OF ACOUSTO-OPTICAL IMAGING

CHRISTOPHER W. JARRETT

Dissertation under the direction of John C. Gore, Ph.D.

Acousto-Optical Imaging (AOI) is an emerging hybrid multi-modal imaging technique that combines the high spatial resolution of ultrasound with the versatile molecular sensitivity of optical detection to improve upon the limited spatial resolution of purely optical techniques. However, the precise mechanisms that contribute to the contrast in AOI have been relatively little explored, and the influence of several physical factors are not well understood. Kobayashi et al. previously reported observations of modulated fluorescence capable of locating fluorescent regions of interest within turbid media, suggesting the ability to use incoherent light for AOI. This research aimed to develop and extend such an approach for applications in biomedical imaging. We aimed to demonstrate the modulation of incoherent light by ultrasound and investigate what factors affect the magnitude of such effects. We proposed the following specific aims: (1) To design and develop instrumentation to detect and quantify Acousto-Optical interactions; (2) To evaluate the contributions of different mechanisms of ultrasonic modulation of fluorescence and the factors that influence these effects in turbid media like tissues; (3) To test a variety of fluorescent contrast agents to determine if their light output may be directly affected by ultrasonic modulation, which would suggest a novel approach to AOI. This work achieved these aim. We were successful in designing and developing an experimental apparatus capable of detecting and quantifying Acousto-Optical Interactions. We determined this signal scales linearly with squared ultrasound pressure but unlike the interpretation of

Kobayashi et al., we found the apparent modulated fluorescence is dominated by acoustic modulation of the excitation light. In addition, we report a novel finding that ultrasound can modulate incoherent light via modulation of tissue absorption and density, incidentally providing a new way to image sound fields. Lastly, we failed to detect direct acoustic effects on common optical agents but successfully observed the direct modulation of light output of ZnS and ZnCdS suspensions. We conclude the observations by Kobayashi cannot be reproduced, and the effects of the modulation of a coherent exciting source must be considered. The potential remains for designing agents whose optical output may be affected by sound fields.

Approved: John C. Gore, Ph.D. Date: October 24, 2014

# PHYSICAL BASIS OF ACOUSTO-OPTICAL IMAGING

By

Christopher W. Jarrett

Dissertation

Submitted to the Faculty of the

Graduate School of Vanderbilt University

in partial fulfillment of the requirements

for the degree of

DOCTOR OF PHILOSOPHY

in

Chemical and Physical Biology

December, 2014

Nashville, Tennessee

Approved:

John C. Gore, Ph.D.
Thomas E. Yankeelov, Ph.D.
Todd E. Peterson, Ph.D.
Henry C. Manning, Ph.D.
Wellington Pham, Ph.D.
Melissa C. Skala, Ph.D.

## DEDICATION

To my late grandfather, Norman Wimberly Fincher, although you are no longer here to guide me, my memory of you does so in every aspect of my life. You were an extraordinary man who loved and treated everyone with kindness and respect. Your commitment, to supporting my education and my pursuit of excellence in all things that I do, has shaped the man I have become. Your legacy will last through my life and all that I achieve.

To my wife, Erin, what a whirlwind the last few years have been! Thanks for standing by me while we lived halfway across the country from one another so I could finish this work! I know it was not easy to be apart, but the bond we developed during the trials and tribulations is unbreakable. I would never have finished this work without your encouragement and sacrifice. I love you!

To my family, Robert, Sylvia, Matt, and Hailey Jarrett, your love and support for all that I do shines through in all aspects of my life. I cannot thank you enough for pushing me to complete this phase in my education.

## ACKNOWLEDGEMENTS

This doctoral thesis not only represents the completion of many hours of typing in front of a keyboard, it is the completion to over a decade of education at Vanderbilt University. Although I started as an undergraduate in the School of Arts and Science in the fall of 2001, I completed my Bachelors in Engineering in December 2005 and continued on to receive a Masters in Engineering in 2008 and now a Doctorate in Chemical and Physical Biology in 2014. I have been surrounded the entire time by the best and brightest and I would not give up my multiple Vanderbilt degrees for the world.

This work would not have been possible without the scientific and personal relationships provided by my colleagues at the Vanderbilt University Institute of Imaging Science (VUIIS). In particular, I would like to thank my advisor and mentor, Dr. John C. Gore. Through his leadership of VUIIS, Dr. Gore has created a world-class institute of imaging research. The caliber of the faculty, scientists, students, and support staff the VUIIS attracts is unmatched and is displayed in the research produced and funding received. Vanderbilt is a better research university because of Dr. Gore and his VUIIS. I will cherish the friendship and mentorship I developed with Dr. Gore. He is a world-renowned researcher who took a chance on me at multiple points within my education and challenged me to become a better all-around student and researcher of the sciences. His willingness to encourage science research for the sake of progressing basic imaging science is what made my work possible. In a research climate dominated by what receives funding, it gives me faith in science that there are still scientists like Dr. Gore who encourage discovery not just for its promise of funding opportunities.

I would like to thank Dr. Charles F. Caskey for his role in helping me finish this work. Dr. Caskey joined the Imaging Institute in my last year at Vanderbilt and within that year I was more productive in my research than the first 3 years of my PhD combined. Charles met with me almost daily, providing a mentorship and experience that was crucial in the completion of my

work. In a single year, Charles helped drive my first publication. I can say that without his assistance this work would not have been completed. Vanderbilt and the Imaging Institute gained a promising young researcher who will provide many years to come of mentorship and successful scientific research.

I would like to thank my PhD committee. I appreciate Dr. Thomas Yankeelov for serving as my committee chair. Tom has been a force of positivity that is unparalleled at the Imaging Institute. He is a world class researcher who is humble and eager to help any of the students at Vanderbilt in any way he can. One cannot help to feel the pride Tom takes in his students and his research. He genuinely cares and has proven time and again to be an asset to my education. I would like to thank Dr. Todd Peterson who provided mentorship in both my Masters research and my PhD research. Todd is a brilliant scientist who relates to his students through friendship and his ability to simplify even the most complex scientific concepts. His knowledge of physics and imaging instrumentation has provided my work an expert who can challenge my experimental apparatus to be the best. Similarly, I would like to thank Dr. Charles Manning. Charles is successful in his research and mentorship of students because he is not afraid to put his nose to the grindstone and challenge the science being done to be better. I would also like to thank Dr. Wellington Pham and Dr. Melissa Skala. Dr. Pham joined my project early on with promising ideas for where my research could go. Although my research took a slight turn, Dr. Pham has been a force of positive encouragement as well as scientific expertise time and again. Dr. Skala provided my research an eye for detail in regards to optical imaging. She encouraged my work to be better and always kept an open mind to exciting new optical imaging ideas. In addition to providing my work with an expert in optical imaging techniques, Dr. Skala provided the immeasurable. In a committee full of people with busy schedules and countless time conflicts, Dr. Skala provided flexibility. She was always willing to adjust her schedule to help me achieve scheduling goals. Without her flexibility, this work would not have been finished. Finally, I would like to thank an honorary committee member, Nancy Hagans. Nancy serves as Dr.

Gore's assistant and without her the entire Imaging Institute would come to a screeching halt. There are very few things that can be done and done right at the Imaging Institute unless Nancy is involved. She has been a tremendous asset to this work without which I would have never finished.

Finally, I would like to thank my fellow students and colleagues at Vanderbilt and the Imaging Institute. Whether it was scientific ponderings, fantasy football discussions, or evening events at research retreats, the friendships you guys brought are what makes the Imaging Institute and my time at Vanderbilt so successful!

## TABLE OF CONTENTS

## LIST OF TABLES

## LIST OF FIGURES

## LIST OF ABBREVIATIONS

**AO**: Acousto-optic

**AOI**: Acousto-optic Imaging

**AOM**: Acousto-optic Modulation or Acousto-optic Modulation measured (see also UMF)

**AOT**: Acousto-optic Tomography

**CCD**: Charge Coupled Device

**CT**: Computed Tomography

**DPSS**: Diode-Pumped Steady-State laser

**Hb**: Deoxygenated Hemoglobin

**$HbO_2$** : Oxygenated Hemoglobin

**MRI**: Magnetic Resonance Imaging

**NIR**: Near-infrared

**PA**: Photoacoustic

**PACT**: Photoacoustic computed tomography

**PAE**: Photoacoustic Endoscopy

**PAI**: Photoacoustic Imaging

**PAM**: Photoacoustic Microscopy

**PAT**: Photoacoustic Tomography

**PET**: Positron Emission Tomography

**PEG-ICG**: Polyethylene Glycol – Indocyanine Green contrast agent

**PMT**: Photomultiplier Tube

**SNR**: Signal to Noise Ratio

**SPECT**: Single Photon Emission Computed Tomography

**UMF**: Ultrasound Modulated Fluorescence (see also AOM)

**UST**: Ultrasound Transducer

**VIS**: Visible light spectrum

# Chapter 1

## An Introduction to Acousto-Optical Imaging

This chapter discusses the background and significance of acousto-optical imaging techniques. It provides a brief overview of current optical and photoacoustic imaging techniques, highlighting the limitations of both modalities and thus provides some of the motivation for developing acousto-optical imaging. The chapter will conclude with describing the state-of-the-art of acousto-optical imaging techniques and will provide the specific aims for this research.

### 1.1 Introduction

Over the past decade there have been many advances in molecular imaging that are driving the use of small animal imaging techniques in preclinical research [1, 2], in particular, small animal imaging systems have been developed for every major imaging modality including MRI, CT, X-Ray, PET, SPECT, and ultrasound. However, with the exception of PET and SPECT, the majority of small animal imaging techniques focus mainly on non-specific imaging of physical, physiological, and metabolic macroscopic changes to distinguish disease and have poor specificity for assessing molecular events. There is a current push to develop small animal imaging techniques which are capable of highly specific, non-invasive imaging at the cellular and molecular level. The development of most of these techniques is outside the scope of this chapter but the reader is referred to the reviews cited for further discussion [2-8]. One technique that is particularly important to this study is the use of optical imaging to image molecular events.

### 1.2 Optical Imaging: Advantages and Disadvantages

Optical imaging techniques for small animal molecular imaging have been developed and used successfully in *in vitro* and *ex vivo* applications [4-11]. Techniques such as fluorescence

microscopy have thrived in the optical imaging realm. However, advances in probe technology, including the development of targeted probes, near-infrared fluorescent probes, activatable fluorophores, and red-shifted fluorescent proteins, have driven optical imaging towards *in vivo* applications [10].

The advantages of optical imaging techniques are abundant. Optical imaging is inexpensive when compared to techniques such as MRI. It is also highly sensitive and specific, capable of detecting nanomolar to picomolar concentrations of a molecular probe [12]. The use of different probes can allow for multi-spectral imaging which allows investigators to image multiple targets at once. Finally optical imaging is minimally invasive when using fluorescent contrast agents and non-invasive when using endogenous contrast sources. It is highly suited for molecular imaging and has shown considerable value in small animal molecular imaging [4, 8, 11, 13]. However, optical techniques are not without limitations.

Optical imaging suffers from high scattering of optical photons in tissue which limits the spatial resolution and penetration/imaging depth attainable [14]. This leads to optical imaging being inherently limited in the detection of deep lesions as spatial resolution declines with increased imaging depth [15]. Due to this scattering of optical photons, spatial resolution in current small animal optical imaging techniques is limited to around 1-3 mm [15] and in practice is often much lower. This leads to optical images overestimating the actual size of the region of interest. In whole animals, diffuse transport of photons also makes it difficult to reconstruct in three dimensions from projections because it is a poorly constrained inverse problem. Thus there is a need to improve upon the spatial resolution of optical imaging techniques while maintaining optical contrast sensitivity.

### 1.3 Ultrasound Mediated Optical Techniques

A recent trend to overcome the spatial resolution and depth penetration issues of optical imaging techniques uses a hybrid technique that combines optical and ultrasound imaging to

form ultrasound mediated optical images. This provides the ability to image with the sensitivity of optical techniques while maintaining the spatial resolution provided by ultrasound pulse echo techniques. Currently there are two separate fields of ultrasound mediated optical imaging, acousto-optical imaging and photoacoustic imaging [15]. We will now give a brief review of both photoacoustic and acousto-optical imaging, but the focus of this thesis is on acousto-optical imaging techniques and thus the reader is referred to the cited literature for a detailed background on photoacoustic imaging techniques [16-31].

### 1.31 Photoacoustic Imaging

Photoacoustic imaging has emerged as a very promising field that has the potential to image both small animals and humans with high contrast and high spatial resolution [31]. This technique is fundamentally based on the photoacoustic (PA) effect which is the generation of acoustic waves by the absorption of electromagnetic energy by a suitable absorber, usually in the form of optical wavelength or radio-frequency energy. The observation that sound can be generated from light absorption was first discovered by Alexander Graham Bell in 1881 when he was trying to develop a means to communicate wirelessly. Bell discovered that if a focused beam of light was rapidly interrupted and allowed to fall on a Selenium block, an audible signal could be picked up through a hearing tube [32]. Here the reader is referred to the earlier papers for the historical development of the photoacoustic effect [24, 33-42]. However, in the past ten years, photoacoustic imaging has accelerated as a promising practical mode of imaging due to major advances in laser technology [43-48].

The motivation for photoacoustic imaging (PAI) is to merge the high contrast and sensitivity due to optical absorption with ultrasonic resolution. This combination is significant because in pure optical imaging techniques scattering in tissues degrades spatial resolution with increased depth and pure ultrasound techniques have poor molecular specificity due to the fact that they are based on detecting variations in mechanical properties of tissues. Also, ultrasound,

unlike optical absorption, is not sensitive to changes in physiological properties such as oxygen saturation or the concentration of hemoglobin. The significance of the combination of optical and ultrasonic imaging techniques is that photoacoustic imaging overcomes the aforementioned problems and in turn yields images of high intrinsic optical contrast with high ultrasonic spatial resolutions.

The basis of photoacoustic signal generation can be seen in figure (1-1). Ultrafast pulsed laser light of a predetermined selected wavelength is projected onto the sample medium. Absorption of the laser pulse excites thermoelastic expansion and subsequent contraction of the irradiated medium, resulting in the generation of MHz range acoustic waves. These acoustic waves reach the surface of the sample tissue at various time delays based on the speed of sound within the medium. These waves are then received via ultrasound receivers [31]. Thus the researcher can acquire images with the high sensitivity of optical techniques while preserving the high spatial resolution of ultrasound imaging techniques. However, photoacoustic imaging techniques are not without limitations.

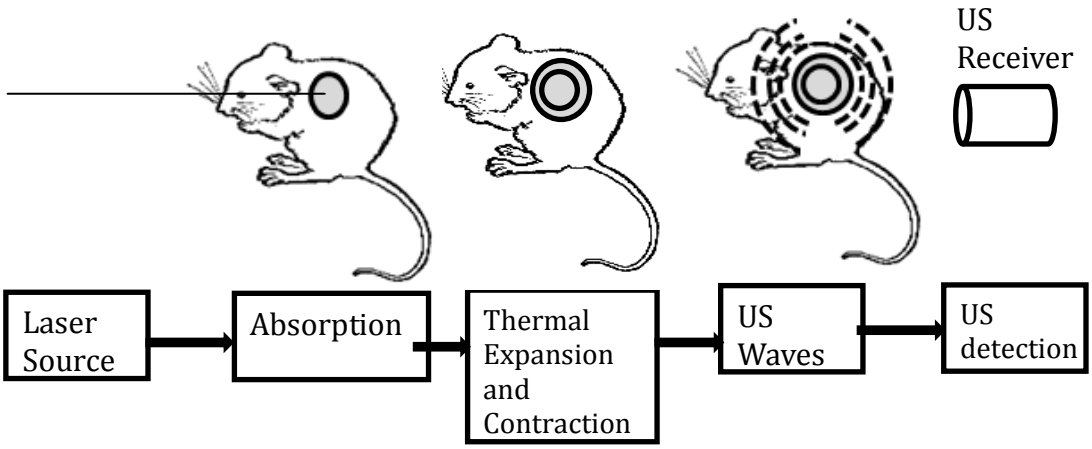


**Figure 1 - 1 Photoacoustic signal generation**

Although less expensive relative to MRI and nuclear techniques, photoacoustic techniques require the use of a two laser system that is relatively costly. In most circumstances,

a pump laser is required to pump an ultrafast near infrared laser to generate the excitation light characteristics required of photoacoustic techniques. The combination of these two lasers alone can cost in excess of $200k before the cost of the additional set-up. In addition to high starting costs, photoacoustic imaging techniques are also limited by optical scattering and absorption which affect the sensitivity and resolution.

As the generation of the photoacoustic signal is based on the amount of light absorption within the medium, photoacoustic imaging techniques are limited by optical scattering and absorption. PAI is limited currently by the depth penetration possible by light in tissues. It has been shown that light penetration can be as much as 5.2 cm with a resolution of a minimum of 780 μm [17]. However better resolution has been reported down in the range of 10s of microns with shallow targets. This leads to the need to increase the penetration depth of the excitation light in order to enhance photoacoustic imaging while maintaining high resolutions. Ideally, depth penetration should be a minimum of 10 cm or even approach the 20 cm possible with ultrasound. It has been shown that contrast agents can be used to enhance photoacoustic imaging techniques. Wang et al. showed that as little as 7 pM PEG-ICG contrast agent can be imaged using photoacoustic imaging techniques [17]. Although contrast agents can be used for photoacoustic contrast, the most successful source of contrast to date has been that provided by blood hemoglobin oxygenation [49, 50]. As the optical absorption coefficient in blood is dependent on the ratio between oxygenated ($HbO_2$) and deoxygenated hemoglobin (Hb), there is inherent photoacoustic contrast in tissue based on blood oxygenation in the region of interest [50]. Using this source of photoacoustic contrast, PAI and photoacoustic tomography (PAT) is currently emerging as a viable pre-clinical and clinical imaging modality with broad applications ranging from vascular biology to oncology [51]. This successful implementation of PAI techniques has spurred a myriad of sub-techniques including photoacoustic microscopy (PAM), photoacoustic computed tomography (PACT), and photoacoustic endoscopy (PAE). Furthermore, success in PAI research has translated to the development of dedicated pre-

clinical small animal imaging systems as well as the implementation of the first clinically viable PAI imaging devices [52] including the photoacoustic mammoscope capable of imaging human breast cancer *in vivo* [53].

### 1.32 Acousto-Optical Imaging

Different to PAI, in acousto-optical imaging techniques, an ultrasonic wave is focused in the imaged tissue and light (excitation or emission) passing through the focal zone is modulated based on the ultrasonic frequency. This modulation of the light theoretically allows for imaging at the spatial resolution of the ultrasound focal region while maintaining the contrast provided by the optical imaging technique.

Acousto-optical imaging began in the early 1990s when Marks et al. experimented with the ability of "tagging" light with ultrasound [23]. Lihong Wang was able to acquire images of tissues phantoms in the mid-1990s, while Leutz and Maret theoretically and experimentally analyzed the ultrasonic modulation of light [20, 25]. Since the mid-1990s, different modes of Acousto-Optical imaging have been developed and have reached a level where they are in close competition with photoacoustic imaging [15]. However, the majority of the development of Acousto-Optical imaging has utilized the ultrasonic modulation of only coherent light.

Until recently, ultrasonic modulation of incoherent light was believed to be too weak to observe experimentally [15]. Mahan et al. studied the modulation of the intensity of incoherent light produced by an ultrasound field [22]. They stated the modulation was due to modulation of the scattering coefficient in the medium surrounding the light source but they did not take into consideration the modulation of the absorption coefficient and the index of refraction [22]. Another theory proposed by Granot et al. asserts that the modulation of photon propagation is a tagging process and related this process to a formula taking into account the position of the ultrasound transducer in relation to the optical signal at the detector. However they did not define at what efficiency the tagging occurs. In 2005, Krishnan et al. proposed a theory to

explain ultrasonic modulation of incoherent light in turbid media [54]. This theory was based on the hypothesis that the ultrasonic waves cause a change in the optical properties of the tissue in the US focal zone. Specifically, it is postulated that the index of refraction of the tissue in the US focal zone is altered causing the modulation of the fluorescent light [54]. This approach is known as the acoustic lens model as the change in refractive index creates a “lens” capable of modulating the direction of light traveling through the ultrasound focal region. Most recently, Yuan et al. proposed the theory that the modulation mechanism is dominated in two situations, under non-quenching and quenching conditions. When fluorophore concentration is too low for quenching to occur, they postulate that the modulated fluorescence signal is in proportion to the fluorophore concentration in the ultrasonic focal zone. When fluorophore concentrations are high enough for quenching to occur, they state the modulation mechanism is due to a modulation of the quenching efficiency [55]. None of these proposed mechanisms completely coincide and thus the mechanism of modulation is still unclear.

Despite lacking a complete understanding of the modulation process, advances have been reported in the field of Acousto-Optical imaging. Kobayashi et al. reported it was possible to obtain 3D fluorescence tomography images, both in a water tissue phantom and a porcine tissue phantom, utilizing ultrasound modulation of incoherent light [56, 57]. These provocative results have stimulated others and motivated this work. Hall et al. have focused on improving detection methods utilizing a gain modulated, image-intensified, CCD camera. This was thought advantageous as the modulation of incoherent light is very weak and the majority of the signal received by the detector is signal from unmodulated photons [58]. The mechanism of modulation, as well as the ability to modulate with higher intensity, has yet to be fully determined. Moreover, at the inception of this work, no group had reported the use of ultrasound to directly modulate light output of a fluorophore, a third possible approach to AOI explored here.

### 1.4 Kobayashi Experiments

To date there have been a very limited number of groups that have reported success in detecting the ultrasonic modulation of incoherent fluorescent light. Kobayashi et al. has described a system to demonstrate the apparent ability to ultrasonically modulate fluorescent light and image tomographically [56, 57]. The system set-up for their first experiments can be seen below in figure 1-2(A). This system was modified in a second set of experiments to include a Ti:Sapphire laser which allowed the use of a near-infrared (NIR) wavelength. This system, with the modified components, can be seen in figure 1-2(B).

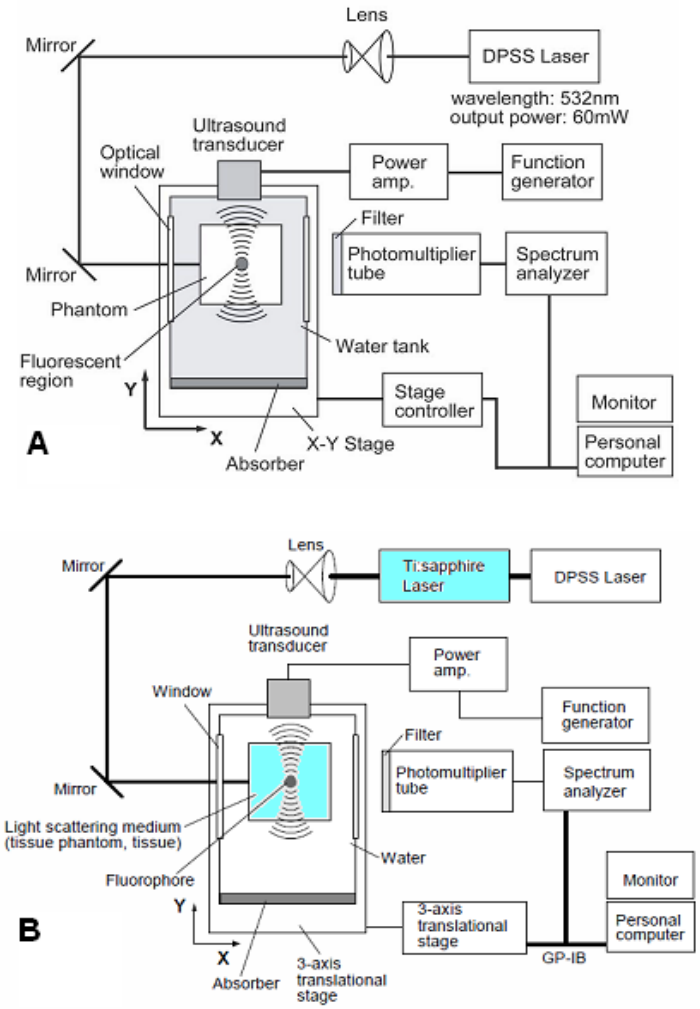


**Figure 1 - 2 Kobayashi et al. experimental apparati (A) Schematic of experimental set-up for 532 nm wavelength. (B) Schematic of the experimental set-up at 726 nm wavelength. Adapted from Kobayashi 2006 and 2007.**

Their first experiment involved the use of localized fluorescent regions embedded in a turbid media like tissue phantom. The tissue phantom was designed to occupy a 40x40x75 $mm^3$ volume. This was prepared by first diluting Intralipid in 5% agar to create an isotropic light-scattering media. The gel was then molded with a final volume concentration of Intralipid of 40 ml/l Intralipid in 5% agarose gel with water-glycerin (20%) solution. A fluorescent region consisting of fluorescent microspheres, with 530nm absorption peak and 590 nm emission wavelength, was embedded in a column of agarose gel 5mm long and 3 mm in diameter. The estimated reduced scattering coefficient of the phantom was 0.61 $mm^{-1}$ at 590 nm.

They illuminated the tissue phantom using a 532 nm diode pumped solid state (DPSS) laser at 60 mW beam intensity with a 1 mm diameter spot size. A 1 MHz focused ultrasound transducer with 38 mm focal length and 3 mm focal diameter was used as to modulate the light in the focal zone. The transducer was driven by a continuous sinusoidal wave and was directed into the side wall of the tissue phantom incident perpendicular to the incident laser light. A photomultiplier tube (PMT) was used as a detector and the signal was delivered to a spectrum analyzer and the intensities of the component frequencies were analyzed at 100 Hz bandwidth. They then obtained two-dimensional tomographic images of fluorescence intensity by mounting a water tank on a two-axis translational stage. The tissue sample was placed within the water tank. The tank was then translated in 500 μm steps in both the x and y directions to obtain two-dimensional tomographic images.

The results showed that the fluorescence modulation intensity increased with increasing sound pressure. This can be seen in figure 1-3(a). Furthermore they showed that fluorescence can be modulated and imaged tomographically. However they failed to explain their inference that the modulation mechanism is induced by density variations of the media located in the ultrasonic field. They stipulate that these density variations cause changes in the index of refraction as well as the optical scattering coefficient of the medium [56]. In the second experiment the excitation wavelength was altered from 532 nm to 726 nm by incorporating a

Ti:Sapphire laser as seen in figure(1-2(B). They also altered the final volume concentration of Intralipid in the tissue phantom from 40 ml/l to 80 ml/l and changed the fluorescent microspheres to 715 nm absorption peak and 755 nm emission peak. They also created a second phantom by placing porcine muscle in the sample holder in place of the isotropic light-scattering gel. The results were similar to that in the first study however they show that modulated fluorescent signals could be imaged up to 30 mm in depth, which is useful for both rats and mice. However once again they failed to explain further the modulation mechanism [57]. More importantly, they did not explain how they were able to remove modulated fluorescence created by the modulation of the coherent excitation light. Modulated fluorescence created by modulated coherent excitation light should be an expected signal which is orders of magnitude greater than modulation of fluorophore emitted incoherent light. This is due to the greater modulation depth or modulation efficiency of coherent versus incoherent light sources. Furthermore, modulated fluorescence created by modulated coherent excitation light is impossible to remove from the AOI signal as it should have the same wavelength and frequency as the modulated fluorophore emitted incoherent light. It is expected that the results reported by Kobayashi would be similar laterally but along the excitation axis would be a mapping of modulated fluorescence caused by modulated coherent light and falling off sharply after the fluorescent region of interest.

To date, no group has been successful in repeating the experimental results of Kobayashi et al. There have been a few attempts reported with the conclusions being that the signal is too weak to be recorded as Kobayashi observed and that adjustments to the experimental set-up should be made to improve upon the modulation depth [55, 59-62]. It is one goal of this research to attempt to repeat the Kobayashi experiments in order to shed light on the mechanism of the reported interaction.

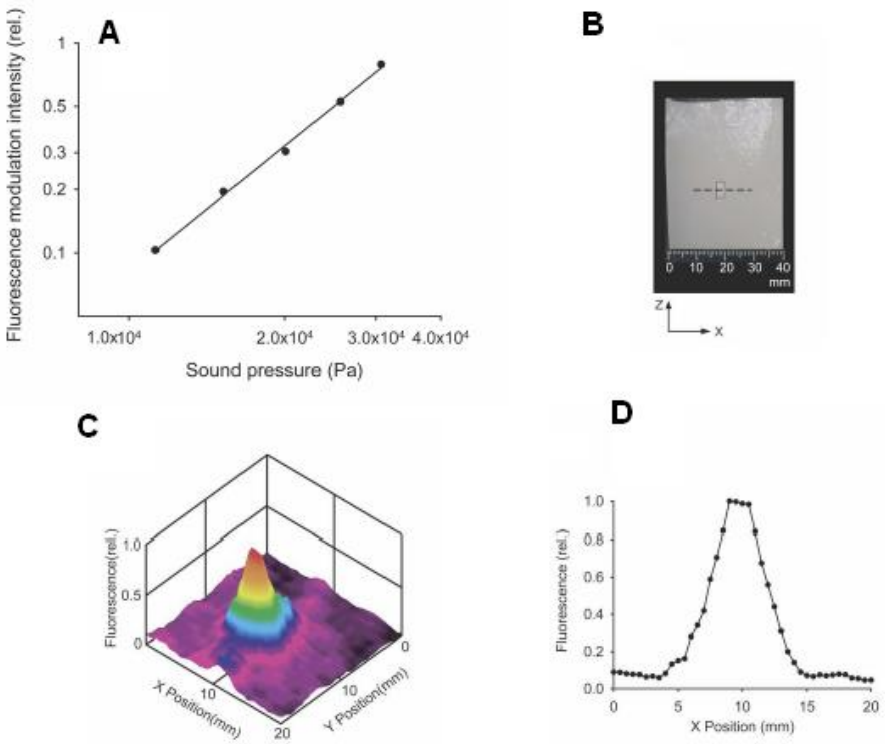


**Figure 1 - 3 Kobayashi et al. experimental results (A) Fluorescence modulation intensity as a result of increasing sound pressure. (B) Photograph of embedded fluorescent region in the tissue phantom. (C) 2-D tomographic image of modulated fluorescence intensity. (D) Fluorescent intensity along the x axis**

### 1.5 Specific Aims

Given the previous reports of developments in AOI, the proposed research will investigate ultrasonic modulation of incoherent light produced by fluorescence. **Overall, we aim to demonstrate the modulation of incoherent light by ultrasound and investigate what factors affect the magnitude of such effects.** In particular we proposed the following specific aims:

**Aim 1:** To design and develop instrumentation to detect and quantify Acousto-Optical interactions.

**Aim 2:** To evaluate the contributions of different mechanisms of ultrasonic modulation of fluorescence and the factors that influence these effects in turbid media like tissues

**Aim 3:** To test a variety of fluorescent contrast agents to determine if their light output may be directly affected by ultrasonic modulation, which would suggest a novel approach to AOI

Successfully achieving these aims will provide insight into the mechanism of ultrasonic modulation of incoherent light in tissues while potentially providing a technique better suited for detection of optical molecular imaging agents. This study will allow us to determine if this technique is a viable modality to be investigated for use in different applications.

### 1.6 Conclusion

The following chapters will provide a documentation of the research performed. Chapter 2 will provide an overview on the theory of Acousto-Optical Imaging. Chapter 3 will provide a detailed characterization and description of the developed AOI system. Chapter 4 will give a detailed account of the experimental results of our attempt to recreate the experimental observation of Kobayashi et al. Chapter 5 will report our experimental observations of acousto-optic modulation of an incoherent LED light source. Chapter 6 details our attempts to directly modulate a variety of contrast agents. Finally, chapter 7 will be a discussion of our conclusions and provide potential future directions for Acousto-Optical Imaging. Additionally, in appendix 1, we have provided a detailed System Operations Manual which allows future users to properly operate the developed system.

# Chapter 2

## An Introduction to Ultrasound Modulation of Light

This chapter discusses the theory behind the ultrasonic modulation of light within the field of acousto-optics. It provides a brief overview of light propagation in media, ultrasound propagation in media, and the interaction between ultrasound and coherent light sources. Finally, a description of the current understanding of the interaction between ultrasound and incoherent light sources is provided.

### 2.1 Light Propagation in Turbid Media

As mentioned in chapter 1, light scattering in a turbid media is a significant hindrance to imaging with high spatial resolution in optical imaging techniques. This chapter will discuss the mechanisms of light propagation in a turbid media.

### 2.11 Light Scattering in Turbid Media

In turbid media, scattering is the dominant mechanism of light attenuation when light propagates through the medium [27]. Light scattering occurs due to collisions between photons and scattering particles within the medium and manifests itself as a random change in direction of propagation. These changes in direction occur because the photons are refracted due to a difference in the index of refraction of the scattering particle versus the surrounding medium. Figure 2-1 depicts the change from straight path propagation of light to random steps size path due to scattering events within a homogeneous turbid medium.

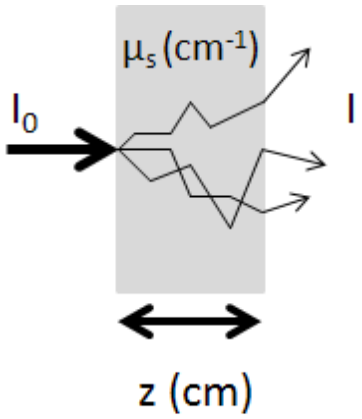


**Figure 2 - 1 Light scattering in a turbid medium**

Scattering within a turbid media is a property that depends on the optical wavelength of the light relative to the size and geometry of the scattering particles. This property is described by the scattering coefficient, $\mu_s$, which represents the probability a single photon is scattered within a medium per unit path length [27]. The scattering coefficient in a turbid medium per unit volume is given by:

$$\mu_s = N_s \sigma_s \tag{2-1}$$

Where $N_s$ is the number density of scattering particles within the medium; and $\sigma_s$ is the cross-sectional area of a single scatterer. The reciprocal of the scattering coefficient gives the scattering mean free path which defines the average path length between scattering events within a medium. Furthermore the probability of a photon propagating a medium without scattering is termed the ballistic transmittance, $T$, and is given as a function of path length $z$ by:

$$T(z) = e^{-\mu_s z} \tag{2-2}$$

As seen in figure 2-1, in a purely scattering medium the intensity of the light is decreased due to scattering events within the medium as a function of distance z traveled through the medium and is given by:

$$I(z) = I_0 e^{-\mu_s z} \tag{2-3}$$

The attenuation due to scattering within a medium can be calculated as:

$$A = \ln\left(\frac{I_0}{I}\right) = \mu_s z \tag{2-4}$$

Within turbid media such as biological tissue, light scattering is most often anisotropic and tends to forward scatter the incident light [27, 63]. Anisotropic scattering is based on the incident angle of the light and has a forward directionality as seen in figure 2-2.

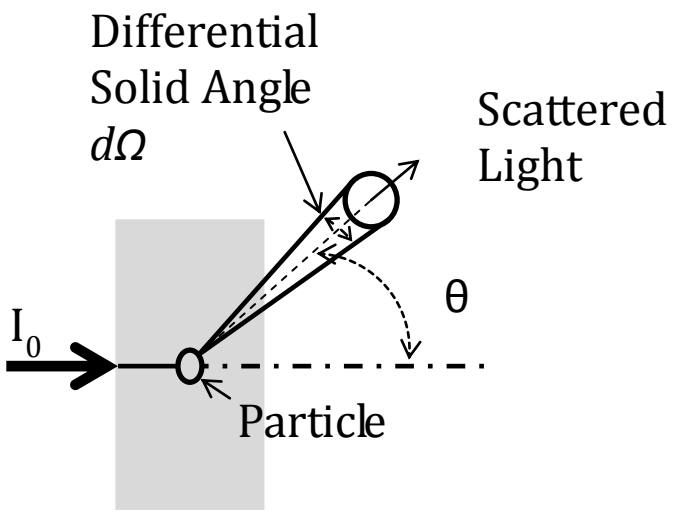


**Figure 2 - 2 Forward scattering of light depicting phase function of the scattering angle.**

Within a turbid medium, the measure of anisotropy is given by the anisotropy factor g and is calculated as:

$$g = \int_{\pi} \cos(\theta) p(\cos(\theta)) d\Omega \tag{2-5}$$

Where $p$ is the phase function representing the probability density function of scattering from the initial direction; and $\theta$ is the scattering angle. Anisotropy factor $g$ is measured from -1 to 1; where $g = 1$ is complete forward scattering and $g = -1$ is complete backward scattering. It is necessary to take into account the anisotropy factor into the scattering coefficient in a turbid media. The reduced scattering coefficient $\mu_s'$, corrects the scattering coefficient for the anisotropy factor g, and is given by:

$$\mu_s' = \mu_s(1-g) \tag{2-6}$$

### 2.12 Light Absorption in Turbid Media

The alternate interaction to scattering in turbid media is absorption. Absorption is the process of energy of a photon energy being transformed into internal energy of the absorbing medium. This

transfer of energy results in the attenuation of the intensity of the light wave that is propagating through the medium. This is seen in figure 2-3.

As with scattering, absorption is an optical property of a medium that is dependent on the wavelength of the light as well as the size, nature and geometry of the absorbers in the medium. The absorption coefficient, $\mu_\alpha$, represents the probability of photon absorption within a medium per unit path length. The absorption coefficient [27] is given by:

$$\mu_\alpha = N_\alpha \sigma_\alpha \tag{2-7}$$

Where $N_\alpha$ is the number density of absorbers in a medium; and $\sigma_\alpha$ is the cross-sectional area of absorbers in the medium. The reciprocal of the absorption coefficient gives the mean absorption length or the distance a photon travels before absorption.

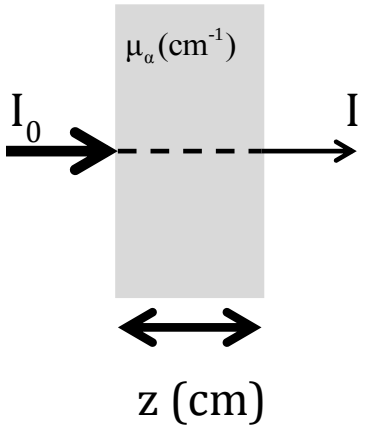


**Figure 2 - 3 Light absorption in a purely absorbing medium**

As seen in figure 2-3, in a purely absorbing medium, light is attenuated based on the absorption over the length of the medium, $z$. The light intensity, as a function of distance z through the medium, is given by Lambert's law:

$$I(z) = I_0 e^{-\mu_a z} \tag{2-8}$$

Where $I_0$ is the initial light intensity [27]. The transmittance, $T$, through the medium is given by:[27]

$$T(z) = \frac{I(z)}{I_0} \tag{2-9}$$

The transmittance represents the probability of a photon not being absorbed over the distance z. The attenuation, A, over the distance, z, is thus given by:

$$A = \mu_\alpha z \tag{2-10}$$

### 2.13 Extinction Coefficient in Turbid Media

In reality, a turbid media consists of absorbing and scattering materials and thus both phenomena occur concurrently as displayed in figure (2-4).

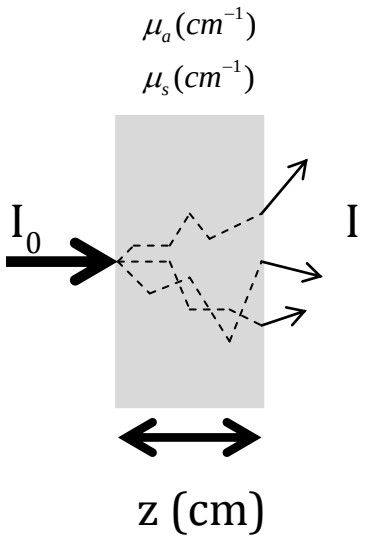


**Figure 2 - 4 Turbid media consisting of both absorbing and scattering phenomena**

It is thus necessary to define the extinction coefficient also known as the total attenuation coefficient $\mu_t$. The extinction coefficient of a medium is given by the sum of $\mu_a$ and $\mu_s'$ or:

$$\mu_t = \mu_a + \mu_s' \tag{2-11}$$

The reciprocal of $\mu_t$ is the total mean free optical path.

Light is attenuated based on the extinction coefficient, $\mu_t$, over the length of the medium, $z$. The light intensity as a function of distance through the medium is given by:

$$I(z) = I_0 e^{-\mu_t z} \tag{2-12}$$

However, in a highly scattering medium ($\mu_s \gg \mu_\alpha$) such as biological tissue, each photon undergoes many scattering events diffusively before being absorbed and thus the light intensity, $I$ as a function of distance $z$, is more complex than that shown in (equation 2-12). The effects of multiple scattering on diffuse photon transport may be modeled using methods such as Monte Carlo modeling. For further information on the modeling of light interactions within a turbid media, the reader is referred to Wang's Biomedical Optics: Principles and Imaging [27].

### 2.2 Ultrasound Propagation in Media

In addition to describing light propagation in tissue, it is necessary to describe ultrasound propagation in tissue for Acousto-Optical imaging. This section will discuss ultrasound propagation in a turbid media.

#### 2.21 Principles of Ultrasound Propagation

Ultrasound is defined as sound waves with frequencies exceeding 20 kHz. More specifically, ultrasound in medical imaging techniques is applied at frequencies between 1-20 MHz. These sound waves propagate through a medium as a longitudinal mechanical pressure or stress wave that induces mechanical perturbations of the particles comprising the medium. The mechanical perturbations are comprised of induced displacements from the resting position of the particles comprising the medium. In a compressible, elastic medium, these displacements

are transmitted step by step to successive regions of the medium and present themselves as alternating regions of compression and rarefaction [64].

The speed at which the ultrasound waves propagate through the medium depends on the material properties of the medium. For low amplitude waves, the speed of sound depends on the acoustic characteristics of the medium and is independent of the amplitude of the ultrasonic wave. The speed of sound $c$ in a medium is predicted by:

$$c = \sqrt{\frac{M_e}{\rho_e}} \tag{2-13}$$

where $M_e$ is the effective elastic modulus of the medium; and $\rho_e$ is the effective mass density (kg/m$^3$) of the medium. The effective elastic modulus is a measure of the elastic and geometric characteristics of the medium and represents the stiffness of the medium in regards to a given type of wave.

As materials differ in elastic modulus and density, there is an expected variation in the speed of sound through varying materials. This variation in speed of sound can lead to reflections and/or refractions of ultrasonic wave propagation through an inhomogeneous medium. Thus it is necessary to compare the acoustic properties of various materials to understand the characteristics of ultrasonic wave propagations through varying regions of differing acoustical properties. This is done by the calculation of the acoustic impedance $Z$ (rayls) and is given by:

$$Z = \rho c \tag{2-14}$$

In a layered medium, depending on the degree of mismatch of $Z$ between two adjacent layers, ultrasound can be transmitted and the percentage that is not transmitted is reflected as seen in figure 2-5.

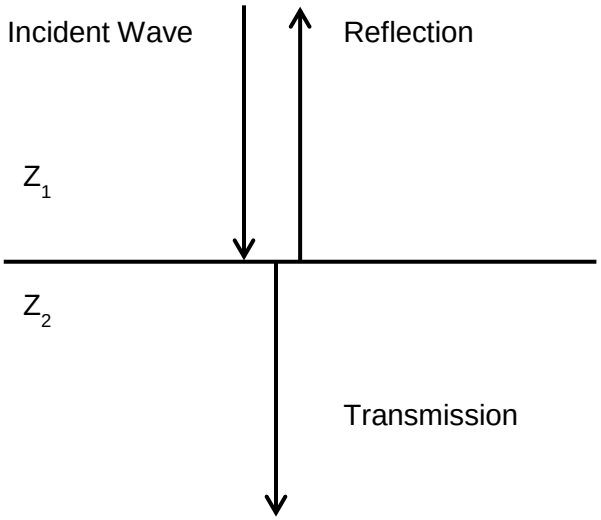


**Figure 2 - 5 Incident ultrasound wave encountering a medium of differing impedance causing reflection and transmission of the wave.**

For a plane wave normally incident on a planar interface, the reflected wave amplitude is:

$$R = \frac{Z_2 - Z_1}{Z_1 + Z_2} \tag{2-15}$$

Where $Z_1$ is the impedance of the initial medium and $Z_2$ is the impedance of the encountered medium. The transmitted wave amplitude is then given by:

$$T = \frac{2Z_2}{Z_1 + Z_2} \tag{2-16}$$

Table 2-1 shows the ultrasound velocity and acoustic impedance of selected biological materials.

| Substance | *c* (m/s) | *Z* ($10^6$ kg/m$^2$s) |
|---|---|---|
| Air (25°C) | 346 | 0.000410 |
| Fat | 1450 | 1.38 |
| Water (25°C) | 1493 | 1.48 |
| Soft Tissue | 1540 | 1.63 |
| Liver | 1550 | 1.64 |
| Blood (37°C) | 1570 | 1.67 |
| Bone | 4000 | 3.8 to 4.7 |

**Table 2 - 1 Ultrasound velocity and acoustic impedance of selected biological materials [64]**

As an ultrasonic wave propagates through a medium, the particles or material elements within the medium are displaced at a velocity $v$ that is related to the sound pressure and acoustic impedance of the material and is given by:

$$v = \frac{p}{Z} \tag{2-17}$$

Where $p$ is the sound pressure in Pascals (Pa) and is given by (2-19):

$$p = Zv \tag{2-18}$$

Using the peak pressure, $p_{peak}$, the acoustic intensity can be calculated, which is the energy transmitted by the ultrasonic wave per unit time and per unit area (W/cm$^2$). For a plane harmonic wave, the sound intensity is related to the peak pressure and the acoustic impedance of the medium and is given by:

$$I_{peak} = \frac{p_{peak}^2}{2Z} \tag{2-19}$$

The peak ultrasonic intensity $I_{peak}$ can then be combined with the cross sectional area $A$ of the irradiated region to determine the peak ultrasonic power which is given by:

$$P_{peak} = I_{peak} A \tag{2-20}$$

As the ultrasonic wave propagates through the medium, the peak pressure is attenuated due absorption and scattering. The absorption and scattering are properties of the medium and depend strongly on the frequency of the ultrasound. The peak pressure at a given distance z into the medium can be determined by:

$$P_{peak} = P_0 e^{-\alpha z} \tag{2-21}$$

Where $P_0$ is the initial peak pressure (Pa); $\alpha$ is the acoustic attenuation (Np/cm) at acoustic frequency $f$ , and is the sum of the acoustic absorption and scattering coefficients of the medium; and $z$ is the propagated distance.

**2.22 Ultrasound Induced Particle Displacement within a Medium**

Within a medium, ultrasonic wave propagation can induce particle displacement of absorbers and scatterers in the direction of the propagation. These particle displacements occur as an oscillation about the mean position of the particle as the sound wave propagates. If visualized, the particle displacement would represent regions of alternating compression and rarefaction based on the distance along the propagating wave (fig. 2-6). The maximum particle displacement $\xi_a(m)$ is related to the peak ultrasound pressure $P_{peak}$ and is shown in:

$$\xi_a = \frac{P_{peak}}{2\pi f_a \rho c} \tag{2-22}$$

Where $f_a$ is the acoustic frequency; $\rho$ is the density of the medium; and $c$ is the speed of sound in the medium.

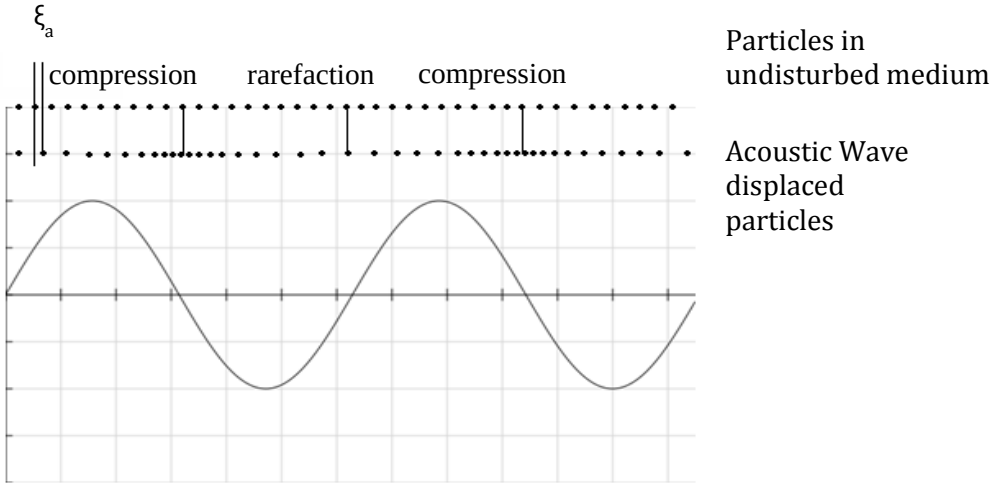


**Figure 2 - 6 Particle displacement within a medium along a propagating wave**

The velocity of this displacement is given by:

$$v = \frac{d\xi}{dt} \tag{2-23}$$

and the peak velocity is:

$$v_a = 2\pi f_a \xi_a \tag{2-24}$$

Finally, the peak particle displacement velocity can be represented in terms of peak pressure by combining equations (2-22) and (2-24). Thus peak particle displacement velocity is given by:

$$v_a = \frac{P_{peak}}{\rho c} \tag{2-25}$$

Using equations (2-14) – (2-25), calculations can be made on both the ultrasound at the focus as well as the effects of the ultrasound on a particle within the focus. For example, given a tissue with density of 1000 kg/m$^3$ and a speed of sound of 1540 m/s, the tissue impedance can be calculated from equation (2-14) giving a z = 1.54x10$^6$ kg/m$^2$s. Next, measurement of a 1 MHz ultrasound transducer with a hydrophone measured peak ultrasound pressure at the focal zone of 42 kPa, the ultrasound intensity can be calculated using equation (2-20) which gives I = 588 W/m$^2$. The particle velocity can be calculated as 0.027 m/s using equation (2-18). Finally, the

maximum particle displacement can be calculated using equation (2-22) giving a $\xi$ = 4.34 nm. Using measurements such as maximum particle displacement, the researcher can understand the movements of particles within a medium in an attempt to understand the influence of ultrasound waves on acousto-optic regions of interest.

### 2.23 Ultrasound induced changes in optical refractive index within a medium

As previously described, the ultrasonic wave propagation creates alternating regions of compression and rarefaction of the medium and its acoustic absorbers and scatterers. These alternating regions create regions of differing local density that act as regions of varying optical index of refraction when illuminated. The change in refractive index $\Delta n$ is given by:

$$\Delta n = \frac{T_{PE} n_0^3 \xi \kappa_a}{2} \tag{2-26}$$

Where $T_{PE}$ is the photoelectric tensor of the material; $n_0$ is the background refractive index; $\xi$ is the particle displacement (m); and $\kappa_a$ is the acoustic wave number ($m^{-1}$) given by:

$$\kappa_a = \frac{2\pi}{\Lambda} = \frac{2\pi f_a}{c} \tag{2-27}$$

Léon Brillouin first proposed this relationship in 1922 [65]. Brillouin modeled the sound wave as a sinusoidal spatial variation of refractive index that acts as an optical diffraction grating [65]. As sound travels at a much slower speed than light, the alternating regions of compression and rarefaction appear to stand still in relation to light traveling through the region. Brillouin essentially predicted what is now called acoustic Bragg diffraction, which is analogous to X-ray diffraction in crystals. This effect can be seen in figure 2-7(b) [66].

This theory describes a critical angle of light incidence, $\pm\alpha_B$, which generates a new beam with direction $2\alpha_B$. This critical angle is known as the Bragg angle and is given by:

$$\sin \alpha_B = \frac{\lambda}{2\Lambda} \tag{2-28}$$

Where $\lambda$ is the wavelength of light in the medium and $\Lambda$ is the acoustic wavelength [66].

Debye and Sears as well as Lucas and Biquard made further refinements of Brillouin's theory in 1932 in which they predicted and observed multiple orders of diffraction and not just the critical angles predicted by Brillouin. The observation of multiple orders of diffraction is demonstrated in figure 2-7(a).

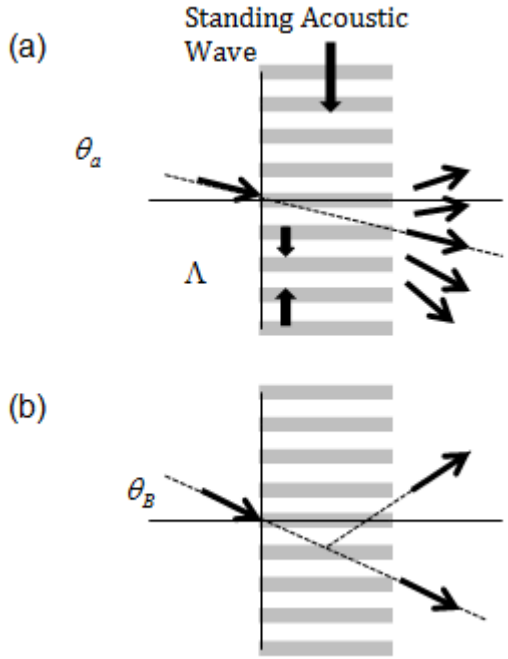


**Figure 2 - 7 Theory of acousto-optic diffraction (a) Raman-Nath (b) Bragg**

Despite their experimental observations, Debye-Spears and Lucas-Biquard were unable to explain the multiple orders of diffraction. In 1935 and 1936, Raman and Nath were able to derive the relations between the multiple orders of diffraction and provided the Raman-Nath equations used currently [67-70]. The observations of acoustic Bragg diffraction (Brillouin) and multiple orders of diffraction (Debye-Sears, Lucas-Biquard, Raman-Nath) have since been

characterized into two optical grating by ultrasound regimes known as the Raman-Nath [67] and Bragg [71] effects. The Raman-Nath regime relates to the observation of multiple orders while the Bragg regime relates to the single order diffraction of incident light specified by the Bragg angle. The separation in the two regimes depends on the acoustic beam width and the wavelength of the acoustic wave. The characterization into each regime is defined using the Klein-Cook parameter given by:

$$Q = \frac{2\pi\lambda_0 d}{n_0 \Lambda^2} \tag{2-29}$$

Where $\lambda_0$ is the optical wavelength (m); $d$ is the ultrasound beam diameter (m); $n_0$ is the refractive index of the medium; and $\Lambda$ is the acoustic wavelength (m) [71]. When diffraction occurs under low acoustic wavelength and thick grating $(Q \gg 1)$, it results in single order diffraction characterized in the Bragg regime. The Raman-Nath regime requires a large acoustic wavelength and thin grating $(Q \ll 1)$ [71, 72]. The Raman-Nath regime dominates acousto-optic imaging interactions in relation to this work, and unless otherwise noted, it is the assumed regime for this study.

### 2.3 Ultrasonic Modulation of Light in a Scattering Media

As discussed in chapter 1, acousto-optical imaging involves the ultrasonic modulation of light and the subsequent detection of modulated optical signal. This ultrasonic modulation is well understood for ultrasound interactions with coherent light sources but the interaction with incoherent light has not been well described. This section will discuss the mechanisms of ultrasonic modulation of light, both coherent and incoherent.

### 2.31 Mechanisms of Ultrasonic Modulation of Light in a Scattering Media

There are currently three proposed mechanisms for the ultrasonic modulation of light in a scattering medium:

1. *Ultrasound induced variations in the optical properties of the media*. This mechanism is due to the formation of regions of compression and rarefaction by the propagating ultrasonic wave. These regions of compression and rarefaction are regions of varying density and effectively modulate, in space and time, the absorption coefficient ($\mu_\alpha$), reduced scattering coefficient ($\mu_s^{'}$), and the index of refraction ($n$). For a light beam passing through a region, this mechanism results in the variation of the detected light intensity at the frequency of the ultrasonic wave. The interaction can affect both coherent and incoherent light sources.
2. *Variations in optical phase due to ultrasound induced displacement of scatterers*. The displacement of the optical scatterers is assumed to follow the acoustic pressure wave and thus the optical path length is modulated. The result is a variation in speckle intensity at the frequency of the ultrasonic wave. This mechanism was first modeled by Leutz and Maret but is valid only when the scattering mean free path $\left(\frac{1}{\mu_s^{'}}\right)$ is much greater than the acoustic wavelength [20]. This mechanism is valid only for coherent light sources [73].
3. *Variations in optical phase in response to the ultrasonic modulation of the index of refraction*. Due to the ultrasonic modulation of index of refraction within a medium, the optical phase between consecutive scattering events is modulated at the frequency of the ultrasonic wave. As light is multiply scattered along its path, it accumulates modulated phases resulting in the variation of the speckle intensity. This mechanism is again valid only for coherent light sources [73].

As this research focuses solely on the modulation of incoherent light sources, the second and third mechanisms are not relevant for this work. We will thus focus our discussion on the first

mechanism the *ultrasound induced variations in the optical properties of the medium*. For a detailed review of the second and third mechanisms, the reader is referred to the following: Leutz and Maret, Kempe et al., Mahan et al., and Wang [20, 22, 73, 74].

### 2.32 Ultrasonic Modulation of Incoherent Light within a Scattering Media

Until recently, the ultrasonic modulation of incoherent light within a scattering media was thought to be too weak to measure experimentally [73, 75]. This mechanism was first analytically modeled by Mahan et al. in a slab geometry and is valid only when the scattering length within the medium is small compared with the acoustic wavelength [22]. Initial experimental attempts to observe ultrasonic modulation of incoherent light were unsuccessful by Wang. Subsequent experiments by Kobayashi et al. were able to observe ultrasonic modulation of incoherent light in a scattering medium although attempts to repeat these observations have been unsuccessful [54, 55, 59, 60, 76-78]. Despite proposed theories by Krishnan et al. and Yuan et al., the mechanism of this interaction is still not previously understood [54, 55, 76, 77]. Liu et al., and Bal et al. have proposed models of the modulation of incoherent fluorescent light that are built upon the mechanisms suggested by Krishnan et al. and Yuan et al. These theories will now be discussed.

Krishnan et al. modeled the ultrasonic focal zone within the medium as an “acoustic lens” capable of altering the optical properties of the medium [54]. They suggest that local pressure variations due to the ultrasound wave alter the refractive index of the medium within the ultrasound focal zone. As seen in figure (2-8), as the pressure varies with time, the ultrasound focal region alters the path of photons and thereby creates a spatio-temporal variation in the fluorescent intensity at a detector at the frequency of the ultrasonic wave.

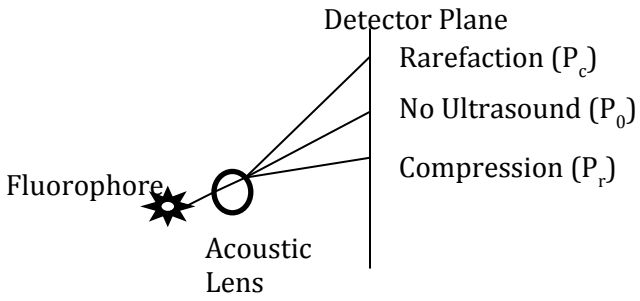


**Figure 2 - 8 Acoustic lens model proposed by Krishnan et al.**

The acoustic focal spot is modeled as a spherical lens with a time varying refractive index. As the index of refraction varies in relation to pressure, the focal region does not have a uniform refractive index but would in reality have a refractive index gradient. For the purposes of simplicity, Krishnan et al. modeled the acoustic lens as a region of uniform refractive index. The diameter $d$ of the focal spot is given by:

$$d = \frac{1.02Lc}{fD} \tag{2-30}$$

Where $L$ is the focal length of the ultrasound transducer; $c$ is the speed of sound in the medium, $f$ is the ultrasonic frequency, and $D$ is the diameter of the transducer. A fluorophore may be considered a point source emitting an optical power $P$. When the ultrasonic focal zone is located between the source and the detector, the peak-to-peak modulated optical signal $P_{FS}$ is given by:

$$P_{FS} = \frac{P_c - P_r}{P_o} \tag{2-31}$$

Where $P_c$ and $P_r$ represent the optical power at the detector at the peak of compression and rarefaction respectively; and $P_0$ is the optical power in the absence of ultrasound. Furthermore, the intensity $I$ measured at the detector plane is related to the fluorophore intensity, and the solid angles subtended by the fluorophore, and is given by:

$$I \propto I_0 \cos\theta_1 \cos\theta_2 \tag{2-32}$$

where $I_0$ is the intensity of the point source, and $\theta_1$ and $\theta_2$ are the angles subtended by the point source and a point at the detector at the acoustic lens (See fig. (2-9)).

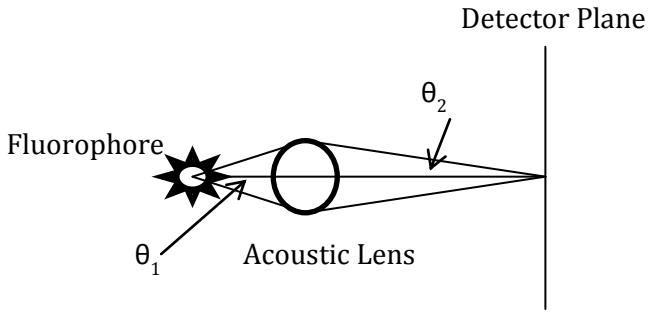


**Figure 2 - 9 Source-detector geometry in relation to the acoustic lens**

Krishnan et al. further modeled this proposed acoustic lens mechanism and named it "FluoroSound" [54]. They based their model on the optical diffusion equation for a scattering dominated medium with spatially varying refractive index and continuous wave light excitation. The optical diffusion equation is given by:

$$\nabla\bullet\left[D_x(r)\nabla\varphi_x(r)\right]+\frac{2D_x(r)}{n_x(r)}\nabla n_x(r)\bullet\nabla\varphi_x(r)-\mu_{a_x}(r)\varphi_x(r)=\frac{E(r)}{4\pi} \tag{2-33}$$

Where $\varphi_x$ is the complex excitation fluence, $\mu_{a_x}$ is the absorption coefficient, $D_x$ is the optical diffusion coefficient, and $n_x$ is the index of refraction at position *r* and *E* is the source distribution. Transport of the emission light from a fluorophore in the same regime is given by:

$$\nabla\bullet\left[D_x(r)\nabla\varphi_x(r)\right]+\frac{2D_x(r)}{n_x(r)}\nabla n_x(r)\bullet\nabla\varphi_x(r)-\mu_{a_m}(r)\varphi_x(r)=-\eta\mu_{a,x-m}\varphi_x(r) \tag{2-34}$$

Where $\eta$ is the quantum yield of the fluorescent emission source, $\mu_{a,x-m}$ is the absorption coefficient of excitation light for absorption by the fluorophore, and $\mu_{a_m}$ is the absorption coefficient of the emission light [54].

Based on this model, Krishnan et al. predicted that the maximum intensity of modulated light would occur when the acoustic lens is located closest to the fluorophore or the detector [54, 55]. However, these findings do not agree with the Kobayashi et al. experiments where the maximum ultrasound modulated fluorescence was reported when the acoustic lens/ultrasound focal zone was in close proximity to the maximum fluorophore concentration [56, 57]. Furthermore, Krishnan et al. considered only the effect of the acoustic lens on the index of refraction within the diameter of the focal zone but they failed to include the effect of the acoustic lens on the scattering and absorption properties within the same region.

In an attempt to model the findings of Kobayashi et al., Yuan et al. proposed a mathematical model for the mechanism of ultrasonic modulation of fluorescence based on variations of local fluorophore concentration within the ultrasound focal zone under both non-quenching conditions and quenching conditions [55]. Here, we will focus on the proposed mechanism under non-quenching conditions.

Yuan et al. inferred from the findings of Kobayashi et al. that the observations of modulation of fluorescence in relation to local fluorophore concentration could only be a result from the physical interaction between the ultrasound focal zone and the fluorophore located within the focal zone. Their hypothesis was that the ultrasonic waves interact with the scattering particles within the focal zone, thus modulating the fluorophore concentration and subsequently the fluorescent intensity. They start with the modulation of microsphere concentration as Kobayashi et al. used fluorescent microspheres as their fluorescent target. Microsphere movement within an ultrasound field is well studied and understood. There are three

mechanisms for the movement of microspheres within an ultrasound field that include [55, 79-84]:

1) Oscillation of particle position, driven by the pressure wave
2) Motion caused by the steady radiation force
3) Oscillation of microsphere radius, driven by the pressure

The first and third types of microsphere motion were considered by Yuan et al. to be possible contributors to the modulated signals observed by Kobayashi et al. They first derived the oscillation of microsphere particle concentration, which is given by:

$$n(r,t) = n_0 + n_1 e^{i(kr-\omega_s t+\varphi_{con})} + c.c. \tag{2-35}$$

where $n_0$ is the average microsphere concentration of the medium, $n_1$ is the modulation amplitude of the microsphere concentration, $k$ and $\omega_s$ are the wave vector and angular frequency of the ultrasound, $\varphi_{con}$ is the initial phase, and c.c. is the complex conjugate. From the oscillation of microsphere particle concentration, they derived the oscillation of fluorescent molecule concentration in the focal zone which is given by:

$$N(r,t) = N_0 + N_1(r)e^{-i\omega_s t} + N_1(r)e^{i\omega_s t} \tag{2-36}$$

where $N(r,t)$ is the fluorophore concentration at the time t and the position r in the focal zone, $N_0$ is the average fluorophore concentration in the focal zone, and $N_1(r)$ is the complex modulation amplitude of the fluorophore concentration at position *r*. This complex modulation amplitude is expressed as a function of amplitude of the ultrasound pressure $P_1$ which is given by:

$$N_1(r) = K' N_0 P_1 e^{ikr} \tag{2-37}$$

where $K'$ is the factor from the curled parenthesis in the equation for the oscillation of microsphere concentration given by:

$$n_1^{'} = \left\{ \frac{k}{\rho_0 c(kv_0 - \omega_s)} \bullet \frac{1+\varepsilon - i\left[\varepsilon + \frac{2}{3}\varepsilon^2\right]}{1+\varepsilon - i\left[\varepsilon + \frac{4}{9}\left(\rho + \frac{1}{2}\right)\varepsilon^2\right]} + \beta \right\} n_0 P_1 \qquad (2\text{-}38)$$

where $k$ is the ultrasound wave vector; $\rho_0$ is the average density of the fluid; $c$ is the speed of sound in the fluid, $v_0$ is the average velocity of the microsphere; $\omega_s$ is the angular frequency of the acoustic wave, $\varepsilon$ is the radius of the microsphere; $\rho$ is the ratio between the density of the microsphere and the average density of the fluid; and $\beta$ is the compressibility of the fluid [55].

Yuan et al. arrived at equation (2-38) by multiplying (2-39) by the scaling factor *M* to convert the microsphere concentration to fluorescent molecule concentration *N*. *M* represents the number of fluorescent molecules per microsphere and thus the number of fluorescent molecules is given by:

$$N = nM \qquad (2\text{-}39)$$

They find that when *M* is held at a constant level, the oscillation of the macroscopic concentration is correlated with oscillation of the density of microspheres within the region and thus the concentration oscillation and subsequently the modulation of fluorescence is dominated by the first mechanism of particle motion within an acoustic field (oscillation of fluorescent particles). Furthermore their model indicated that the modulated fluorescence is proportional to the average fluorophore concentration in the focal zone. They continued by quantifying the modulated signal strength that corresponded to a modulation depth (ratio of modulated fluorescence signal to unmodulated fluorescence signal) of $10^{-4} - 10^{-6}$ with ultrasound pressures in the focal zone in the order of $10^{-5} - 10^{-6}$ Pa [55]. Despite this signal strength being detectable by current detection technologies, Yuan et al. have stated they cannot repeat the results reported by Kobayashi et al. and have questioned the validity of the capability of measuring the interaction [55].

## 2.4 Conclusion

Currently, the interactions observed by Kobayashi et al. have not been replicated and thus have not been explained. This research designed, developed and implemented a state-of-the-art acousto-optic imaging system capable of observing the acousto-optic interactions studied by Kobayashi et al. We repeated the experiments of Kobayashi et al. to determine if the results could be replicated in order to elucidate the mechanism of the interactions between ultrasonic waves and incoherent light. The following chapters will discuss the development of the imaging system, the repetition of the Kobayashi et al. experiments, and our attempts at improving the modulation of a fluorophore's output directly.

# Chapter 3

## Design and Evaluation of a System for Quantification of Acousto-Optical Modulation

### 3.1 Introduction

Here we describe the design and development of a state-of-the-art imaging system capable of measuring Acousto-Optical (AO) Interactions in an effort to further the understanding of the physics that influence these interactions. Recently, Hall et al. and Yuan et al. have designed similar systems to quantify the effects reported by Kobayashi et al. [55, 58-62, 78, 85, 86].

Although there are previous descriptions of AOI systems, it is useful to describe the system from the start. All existing systems are custom built by research groups interested in studying this phenomenon. The ability to tag light via AO interactions was developed by Marks et al. [23], Leutz and Maret [87], Wang et al. [25], and was patented by Dolfi and Micheron [88]. An example of an AO system can be seen in figure 3 - 1. This system was designed by Wang et al. to image objects in turbid media using continuous wave ultrasonic modulation of scattered

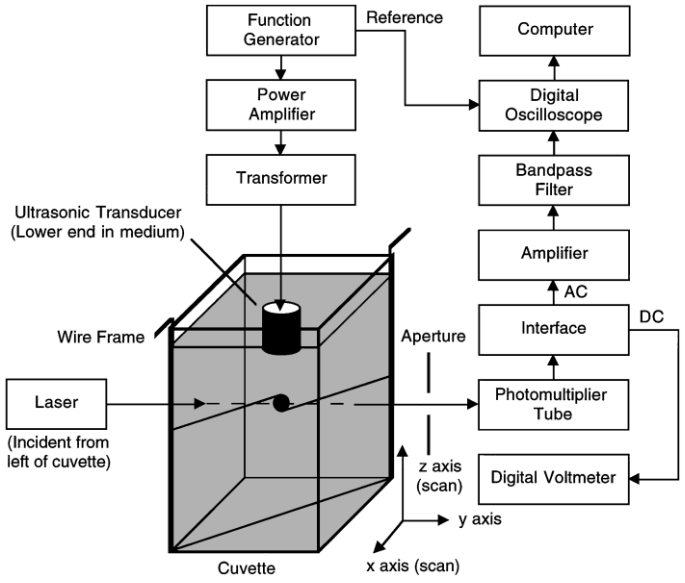


**Figure 3 - 1 Typical setup of an Acousto-Optical Imaging system. Adapted from Wang 1995.**

laser light [25]. Like other AO systems, a sample is illuminated with coherent laser light which is allowed to pass through a focal region of acoustic waves supplied by an ultrasound transducer. After passing through the focal zone and being modulated, the excitation photons can either be transmitted, absorbed, scattered, or can interact with optical fluorophores within the sample. In all cases, a detection system is used to record these interactions. Of particular interest are the interactions of these modulated excitation photons with fluorophores within the sample. A fraction of these interactions can create modulated optical emissions which are detected with the detection system. The interaction between acoustic waves and light has been studied by numerous groups.

Although a large portion of AOI research has been focused on the modulation of coherent excitation light, a few groups have developed systems designed to understand the AO interaction of ultrasound with incoherent light such as the emissions from a fluorophore [56, 58, 59]. Kobayashi et al. were the first to design a system specifically to generate, observe, and record these acousto-optic interactions[56].

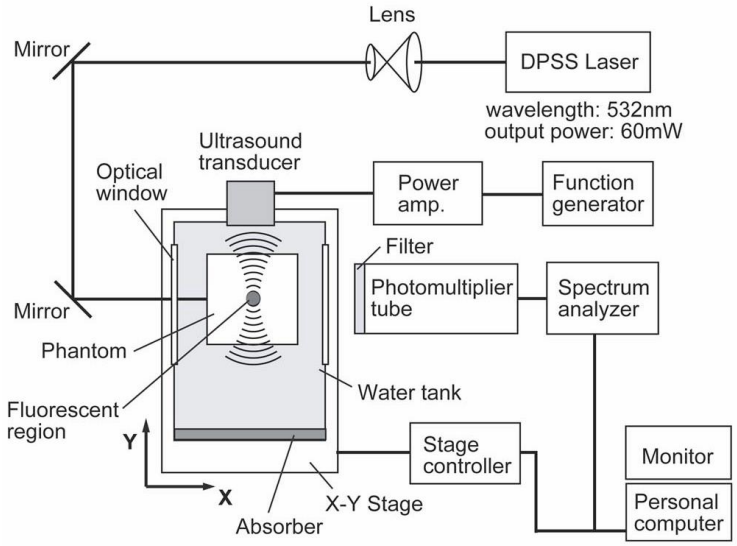


**Figure 3 - 2 Initial experimental acousto-optical modulation setup used by Kobayashi et al. 2006.**

Their system (figure 3-2) consisted of a Diode-pumped Solid-State (DPSS) green laser (Verdi V-6; Coherent, Inc.) with 532 nm wavelength and maximum power output of 6 W but was attenuated to 60 mW. High output lasers such as the Verdi V-6 have a more stable output when operating at higher power which can then always be attenuated. Also, greater than 100 mW excitation is unnecessary. Excitation light was focused

and delivered into a sample box containing a water bath and sample. The water bath is necessary for ultrasound transmission and matches the acoustic impedance of the immersed ultrasound transducer (UST) allowing unaltered acoustic waves to enter the sample. An ultrasound transducer (V314-SU; Olympus-NDT) with a 38 mm focal length, 3 mm focal diameter, was driven by a power amplifier receiving a continuous sinusoidal signal from a 1 MHz function generator. The sound field was introduced perpendicular to the excitation light source and allowed to travel through the sample. The measured sound pressure in the focal region was 41 kPa in water. All light signals were filtered and detected by a photomultiplier tube (PMT) and transmitted to a spectrum analyzer where a 100 Hz bandwidth filter was used to isolate the intensities of the modulated frequencies. Finally, a computer was used for data recording and analysis.

Using this system, Kobayashi et al. were capable of imaging a gelatin tissue phantom containing two separate regions of fluorescent microspheres in both two and three dimensions (figure 3-3). Furthermore, they were able to repeat this experiment in a porcine tissue sample with embedded fluorescent microsphere regions. However because of the scattering of light in tissues affecting depth penetration they modified their system to include a Ti:Sapphire laser pumped by the DPSS laser of the first system [57]. This allows excitation in the near-infrared (NIR) region and they chose specifically 726 nm with an intensity of 40 mW. Because of the absorption characteristics of tissue, NIR light can penetrate deeper into tissue than light in the visible (VIS) spectrum such as that from the DPSS 532 nm laser. This setup can be seen in figure 3 - 4.

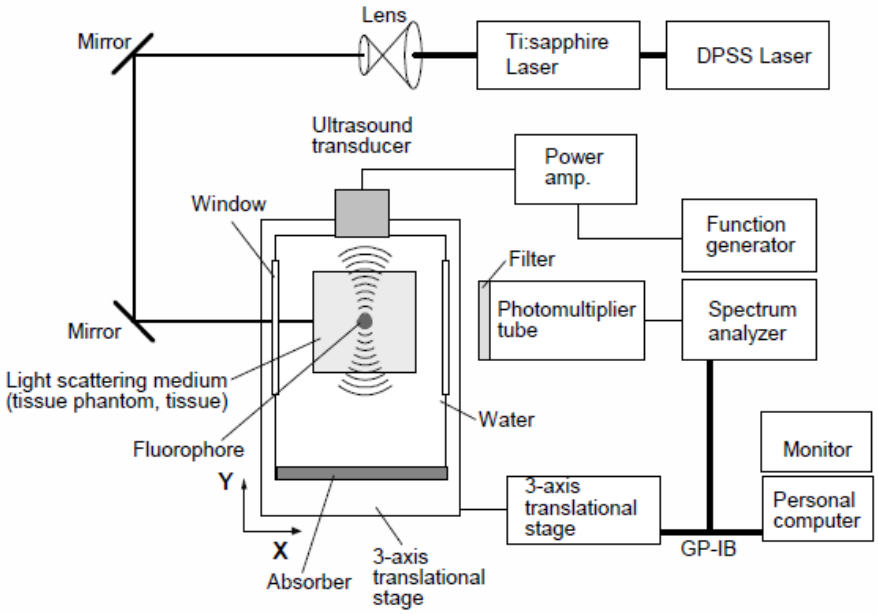


**Figure 3 - 3 Alternate experimental setup used by Kobayashi. Incorporating a Ti:Sapphire laser (732 nm) with an output power of 40 mW.**

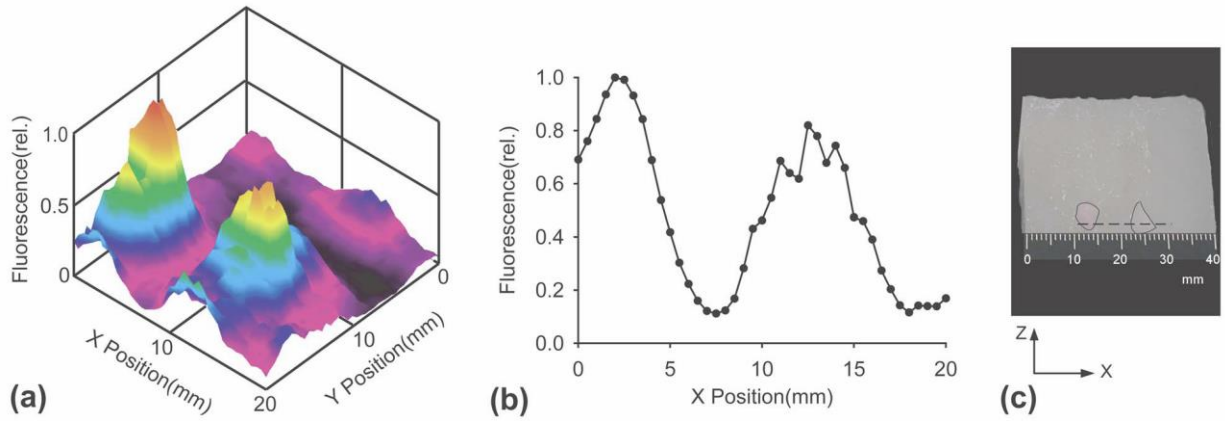


**Figure 3 - 4 Experiments by Kobayashi showing two embedded regions of fluorescent microspheres in a gelatin phantom. This is seen in (a) 3D and (b) 2D; and (c) show the photograph of the regions in the phantom.**

Guided by previous work, we designed an AOI system to quantify different sources of AOI effects. The prominent features of all systems to date are the incorporation of a coherent light source, a sample holder, an ultrasound transducer, and a detection system. The detection system is comprised of filters, a light detector, and a computer or oscilloscope to display and record data received from the light detector. However, there is not an optimized checklist for these components as the requirements of each component vary depending on the research involved. For example, the coherent light source can be optimized for a given fluorescent contrast agent, for depth penetration, or it can be switched off completely for phosphorescent samples. The system must be able to generate, observe, and record AO interactions to be successful.

We first identified a list of characteristics and measurable properties that we desired in a system to facilitate our study of AO interactions. These characteristics are:

1) Broad range of excitation light sources
2) Ability to readily and easily alter system geometry to modify interactions
3) Broad range of Ultrasound Transducer Sources
4) Capable of measuring standard and modulated light signals
5) High sensitivity and SNR

A broad range of excitation light sources allows the study of a range of endogenous and exogenous optical contrast agents as well as the ability to image using varying depths of penetration. The ability to readily and easily alter the system geometry allows for a broad range of sample sizes and types as well as various experimental setups to facilitate maximum AO signal generation and recording. A broad range of USTs allows for the study of the effect of frequency changes as well as acoustic pressure changes on AO interactions. The ability to measure standard and modulated light signals adds the ability to image with and without ultrasonic interaction. Finally, a system of high sensitivity ensures that the study of these interactions can be performed quickly and accurately with the ability to compare studies over

time. We have designed and tested a system meeting our required characteristics. The details of the design and testing process follow.

### 3.2 Acousto-Optical Imaging Apparatus

A schematic of the designed system can be seen in figure 3 - 5 below. Similar to previous systems, a laser excitation source (Sprout-G 6W, Lighthouse photonics) is focused via a 10x Galilean beam expander (BE10M, Thorlabs) to a 1.9 mm spot size. The laser light enters a custom built water bath. An ultrasound transducer (V314-SU-F, Panametrics/Olympus-NDT) is positioned perpendicular to the laser beam and is driven by a continuous sinusoidal wave generated by a function generator (Model 166, Wavetek), FG. A reference signal is also sent to a lock-in amplifier (SR844, Stanford Research Systems). An RF amplifier (Model 200L, Amplifier Research) is used to power the UST. The flexibility of our system allows the movement of the stages (XY Stages, TSB60-I, Zaber Technologies, Z Stage, Microkinetics) in three dimensions. We can move either the ultrasound transducer or the sample using custom designed holders. Signal is focused, filtered, and collected after the custom built water tank. A lens focuses the signal on a dichroic mirror, DF, (Di01-T488/532/594/638, Semrock) which transmits 95% of the excitation light (532 nm) and reflects light at the wavelength of the fluorophore (550-575 nm). Further emission/excitation filtering is performed to exclude any additional excitation light from the signal reaching the PMT. The Ems/Exc filter includes a 550 nm long-pass filter (NT47-617, Edmund Optics) and a band-pass filter (FF01-572/28, Semrock) which has a 572 nm center frequency with a 28 nm bandwidth. The PMT (H5783-20, Hamamatsu) collects the signal which is amplified by the accompanying 20 dB transimpedance amplifier (Hamamatsu C6438). Then the amplified signal is delivered to the lock-in amplifier (LIA). The signal is then displayed on an oscilloscope (54503A, Hewlett Packard) and recorded by a custom LabVIEW program on a dedicated custom computer server (Windows 7, Intel Core 2 Duo, 3.0 GHz, 3 GB RAM). A detailed list of system components can be found in table 3 - 1.

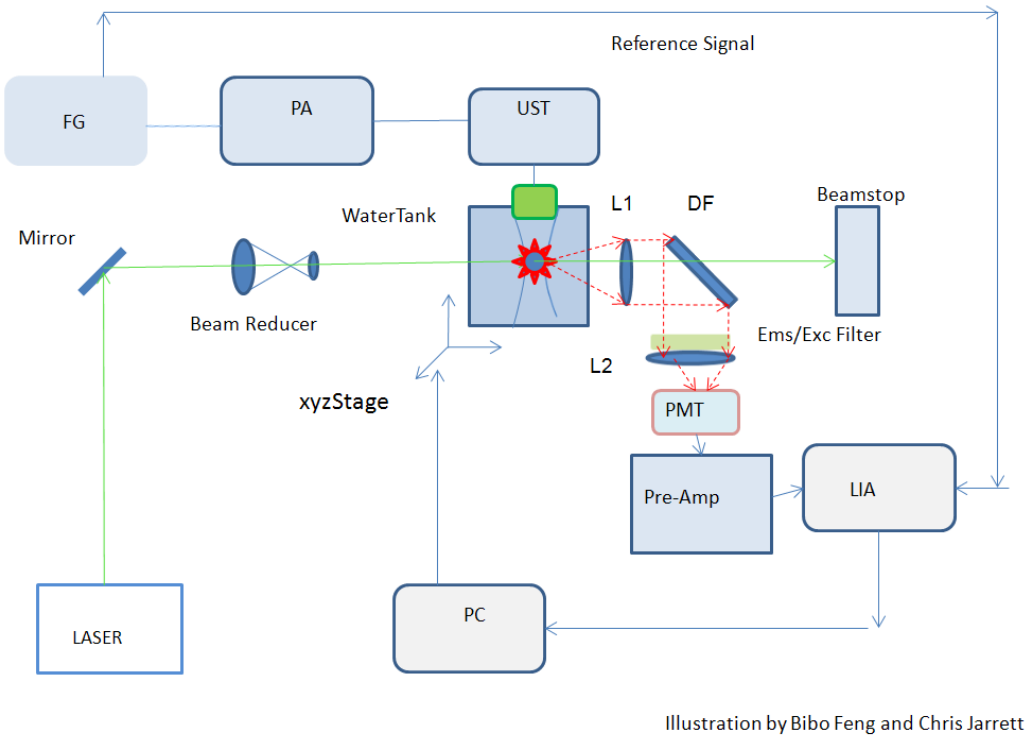


**Figure 3 - 5 Schematic of the custom designed AOI system used for this research**

**Table 3 - 1 List of System Components**

| Abbreviation | Component | Model | Information |
|---|---|---|---|
| Laser | Light Source | LightHouse Photonics, Sprout-G 6W | DPSS 532nm laser, 6 W maximum power |
| FG | Function Generator | Wavetek, Model 166 | 0-50 MHz freq. range, 15 V p-p @50 Ω |
| PA | RF Power Amp. | Amplifier Research, Model 200L | Used at 0-8 W, capable of 200 W |
| UST | Ultrasound Transducer | Olympus-NDT, V314-SU-F | 1.5” Focus |
| Beam Reducer | Laser Beam Reducer | Thorlabs, BE10M | 10x Galilean Beam Reducer |
| XY Stage | XY Motion Control | Zaber Technologies, | 60 mm travel, 0.01 µm resolution |
| Z Stage | Z Motion | Microkinetics | 100 mm travel, 100 µm res. |
| Water Tank | Sample Tank | VUIIS, Ken Wilkens Custom | 130x180x100 mm, 5 windows for various .75” – 2” inserts |
| L1 | Focus Lens | Thorlabs, | 20 mm focal length |
| DF | Filter | Semrock, Di01-T488/532/594/638 | Transmits exc. light @532 nm reflects signal to the PMT |
| Ems/Exc Filter | Filter | Semrock, FF01-572/28 band pass filter | Transmits 558-586 nm signal |
| | | Edmund Optics, 550 nm Long pass Filter OD>2.0 | Transmits >550 nm signal |
| L2 | Focus Lens | Thorlabs, | 150 mm focal length |
| PMT | Light Detector | Hamamatsu, H5783-20 | Sens. 72 mA/W @532 nm |
| Pre-Amp | Signal Amplification | Hamamatsu, C6438 Amp, C7169 Power Supply | 20 dB gain, 0-1.2 V control |
| LIA | Lock-In Amplifier | Stanford Research Systems, SR844 | 25kHz – 200 MHz freq. range, 80 dB Dynamic range |
| Oscilloscope | Signal Viewing | Hewlett-Packard, 54503A | dc-500 MHz, 1 mV/division |
| PC | Computer | Custom Server | Win. 7, 3.0 GHz, LabView Control |

### 3.3 System Testing

The measurement capabilities and performance of the system have been evaluated. The system characteristics directly affecting signal creation and signal detection are the ultrasound transducer's focal zone geometry, laser spot geometry, optical power loss in the system, and detector sensitivity. In order to ensure the system was capable of making AO measurements, we measured the optical power loss through the system, ultrasound focal zone geometry, laser spot geometry, and detector linearity and sensitivity. A description of the measurements and the implications on the system's abilities will now be discussed.

### 3.31 Ultrasound Focal Zone Characterization

The size, location, and pressure of the focal zone produced by the ultrasound transducer used in the imaging system affect the ability to create Acousto-Optic interactions. Measurements were performed using the setup shown in figure 3 - 5. The water tank was built such that an UST can be placed into the end of the tank and held in place via O-rings and a clamping system. The O-rings ensured that the tank was watertight. A hydrophone (Onda HNC-0200) was hung from the stage motion system and was used to scan in three dimensions the output ultrasound field from the V314 transducer located in the side of the tank. The UST in the side of the tank was placed on continuous output and the hydrophone received the output and converts the signal to an output voltage that is read on an oscilloscope. Voltage output from the hydrophone is delivered as RMS measurement ($V_{rms}$) and then converted to peak-to-peak ($V_{p\text{-}p}$).

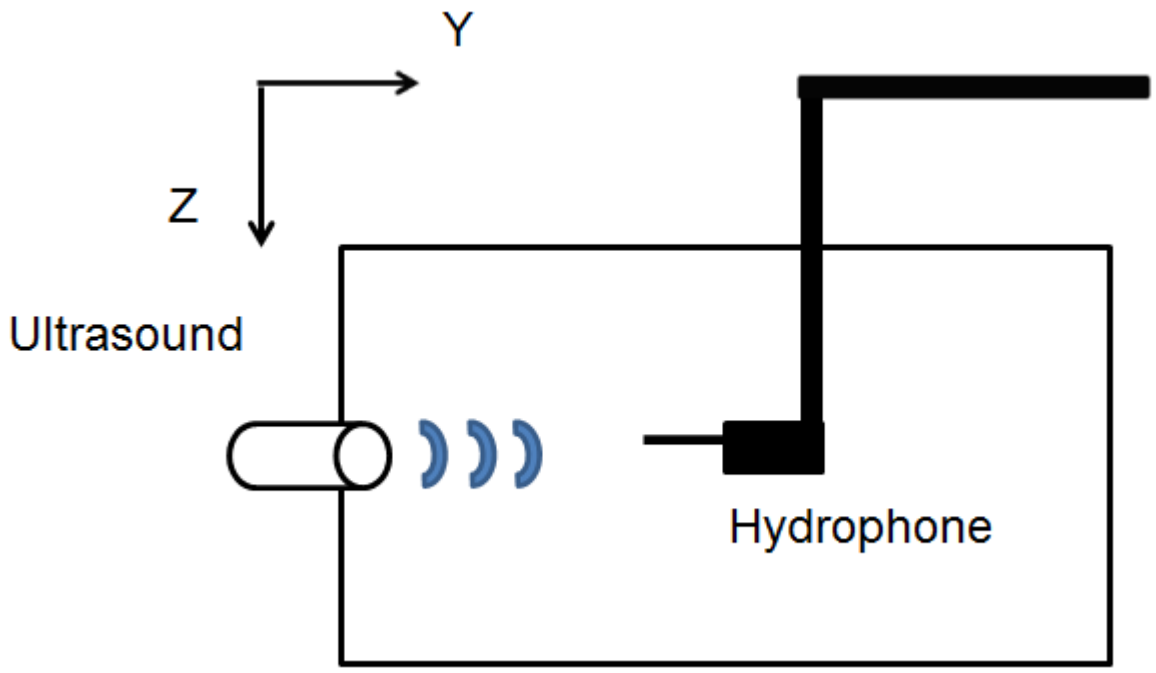


**Figure 3 - 6 Characterization of the US field using a hydrophone.**

Calibration of RF Amplifier Output in relation to Hydrophone Output Voltage

An initial set of measurements was designed to calibrate the RF amplifier output to the US transducer. To relate the RF amplifier's output to the pressures produced by the US transducer, the hydrophone was scanned in three dimensions to determine the location of peak ultrasound signal. The hydrophone was then positioned such that the tip was located at the center of the location of peak ultrasound signal. Next the RF amplifier input voltage was ramped from 0-100 Volts peak-to-peak in 5 V increments. The limit of peak-to-peak voltage was chosen at 100 $V_{p\text{-}p}$ to protect the US transducer from damage as specified by the manufacturer. The hydrophone output voltage was then converted to US pressure utilizing the following equation:

$$M_L(f) = G(f) M_c(f) \frac{C_H}{C_h - C_A} \tag{3-1}$$

where $M_L(f)$ is the sensitivity of the hydrophone and pre-amp combination; $G(f)$ is the amplifier gain as a function of frequency (measured at 19.36 dB @ 1 MHz); $M_c(f)$ is the

sensitivity of the hydrophone as provided by the manufacturer $\left(\frac{V}{Pa}\right)$ reported at $2.48x10^{-8}\frac{V}{Pa}$ @ 1 MHz; $C_H$ is the capacitance of the hydrophone (66.1 pF); and $C_A$ is the capacitance of the amplifier (7 pF).

The hydrophone output voltage was recorded at the oscilloscope and a calibration curve was created using the calculation that $M_L(F)$ @ 1 MHz is 4.34 x $10^{-7}$ $\frac{V}{Pa}$. The calibration curve can be seen below.

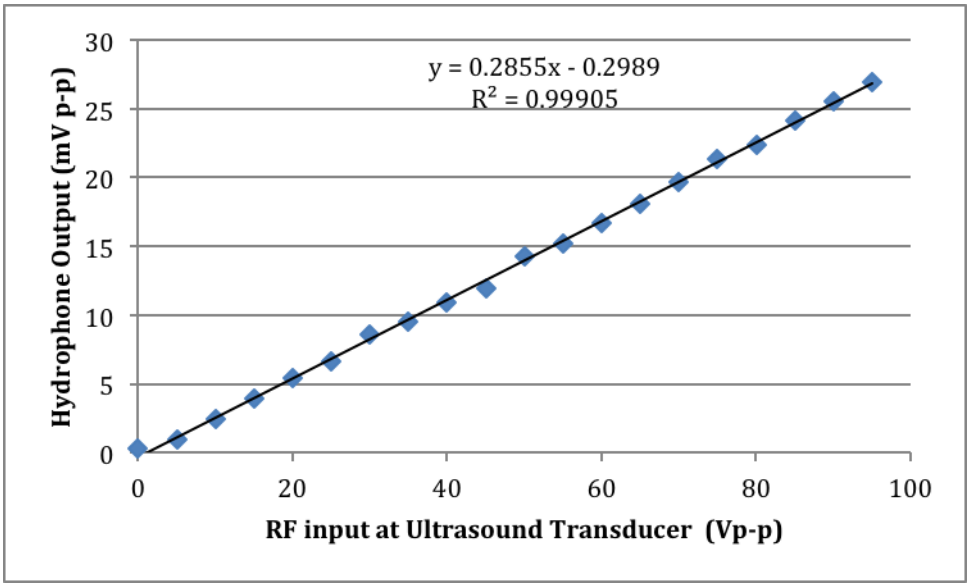


**Figure 3 - 7 Calibration curve of RF output voltage at the US transducer versus hydrophone output voltage.**

Of particular note is the hydrophone output when the US transducer is set at 60 $V_{p-p}$ as this voltage was reported by Kobayashi et al. and is necessary to compare our measurements with their research [56, 57]. With equation 3 - 1 and the calibration curve data, the RF output to the US transducer can be converted to a measured US pressure, figure 3 – 8. This was important because both Kobayashi et al. and Yuan et al. reported US pressures of ~40 kPa at 60 $V_{p-p}$ transducer input [56, 57, 59, 78]. As can be seen in figure 3 - 8, the US transducer produces

roughly 40 kPa of pressure output at a 60 $V_{p-p}$ RF input power which corresponds to the other groups using an identical US transducer.

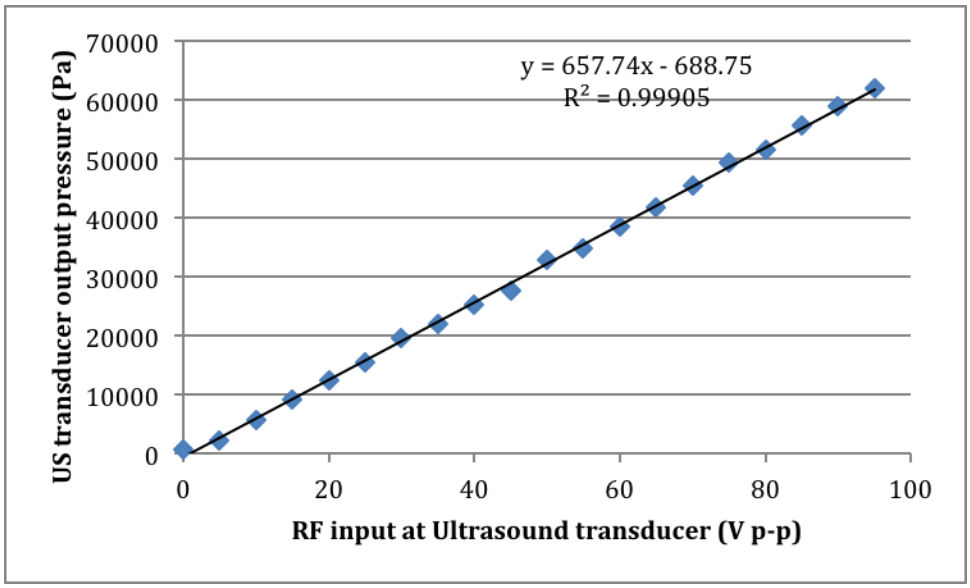


**Figure 3 - 8 RF input versus US transducer pressure output**

Characterization of the Ultrasound Focal Zone

Along with knowledge of the ultrasound pressure in the focal zone, an accurate understanding of the size and shape of the focal zone is crucial to performing AO experiments. Using the side looking set-up shown in figure 3 - 9, a side receiving pencil type ultrasound transducer (V3591, Panametrics) was scanned in three dimensions to determine the location of peak ultrasound signal. The US transducer used was a focused transducer with a 1.5" focal length. The US transducer was driven with a 60 $V_{p-p}$,1 MHz sinusoidal

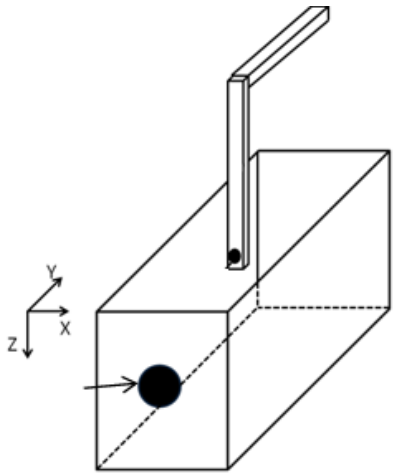


**Figure 3 - 9 Experimental setup of US field characterization using a side receiving US transducer**

waveform. This voltage was chosen as it mimics the experimental methods used by other groups.

To obtain an accurate position of the focal length, the pencil tip transducer was scanned along the axial (Y) direction at the center of the lateral plane. The results are shown in figure 3 - 10. Next the pencil type UST was positioned with the tip located in the Y plane of maximum ultrasound intensity and scanned in the XZ dimensions to create a map of the Ultrasound focal region in the lateral plane of peak US intensity. A two dimensional scan with the hydrophone was performed in the XZ plane to measure the peak shape and location of the US focal zone. The results can be seen in figure 3 – 11 (top). Next, the peak intensity was plotted along the lateral (x) axis and a full-width half maximum intensity measurement was made of the diameter of the focal zone and compared to the predicted diameter from the equation [89]:

$$BD(-6dB) = \frac{1.02Fc}{fD} \tag{3-2}$$

where $BD$ is the beam diameter, $F$ is the focal length; $c$ is the material sound velocity; $f$ is the ultrasound frequency; and $D$ is the element diameter. Assuming a focal length of 38.1 mm, material sound velocity of 1540 m/s, an Ultrasound frequency of 1 MHz, and a 19.05 mm element diameter reported by the manufacturer of the Olympus-NDT V314-SU-F transducer, the predicted beam diameter in the focal region is 3.14 mm. Our measured full width at half maximum intensity was 3.75 mm which is slightly larger than predicted. This value was measured at the maximum axial intensity location identified in figure 3 - 11(bottom). The maximum axial intensity occurred at 27 mm axial scan distance. The scan stage was limited in the axial direction of travel to 60 mm and thus the scan was initiated at 11 mm from the face of the transducer. The combination of the 27 mm focus intensity and the additional 11 mm distance from the transducer provides a 38 mm focal length which is 99.7% of the manufacturer provided focal length of 38.1 mm.

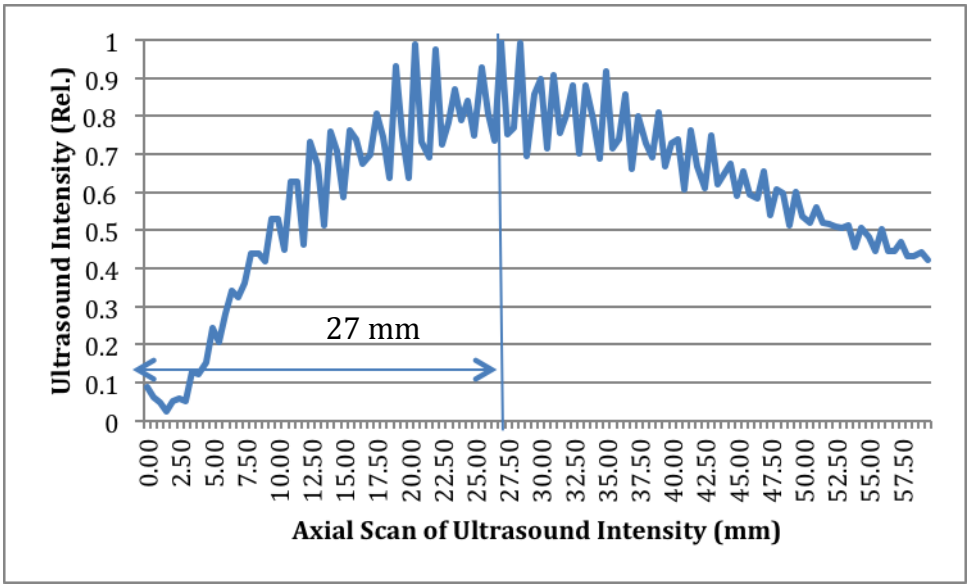


**Figure 3 - 10 Axial (Y) scan of ultrasound focus of the V314-SU-F 1.5" focused transducer.**

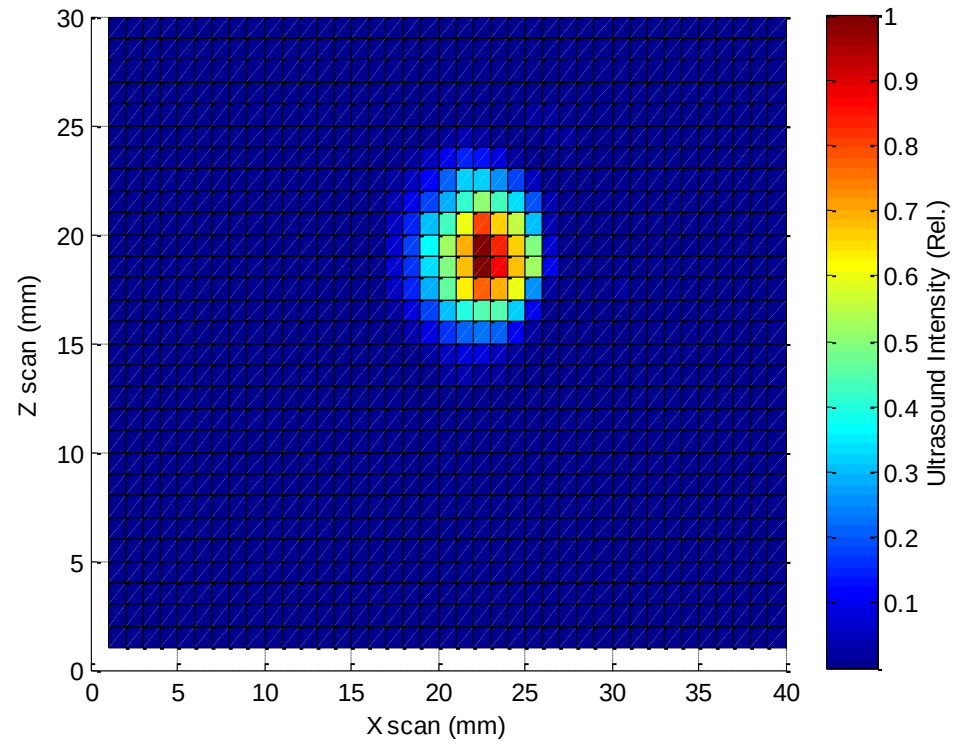


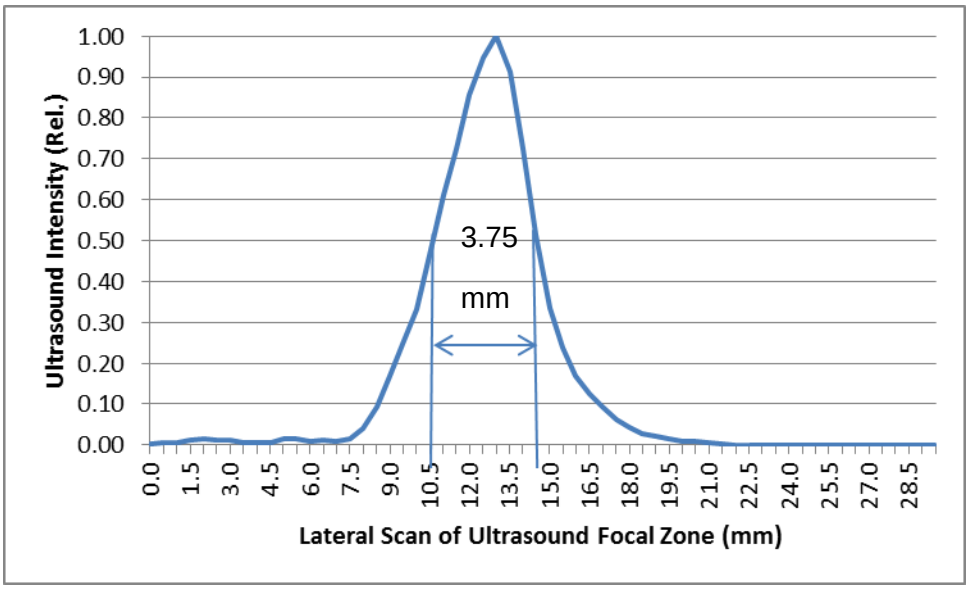


**Figure 3 - 11 Characterization of lateral ultrasound field. (top) 2D intensity plot of the ultrasound focal zone (bottom) Peak intensity profile of the US focal zone.**

### 3.4 Laser Spot Size

The laser beamwidth determines the field of laser excitation and thus the region of Acousto-Optical interaction. Laser spot size was measured using the setup shown in figure 3 - 12. This experiment has been shown to accurately measure the diameter of the laser beam [90]. A knife-edge is stepped across the laser beam in an appropriate step size determined by the anticipated spot size and Nyquist sampling theorem.

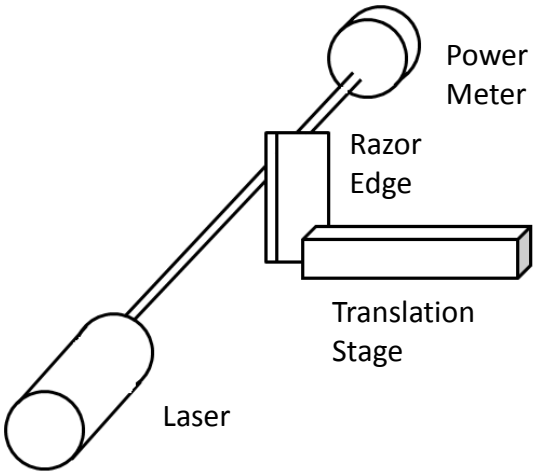


**Figure 3 - 12 Knife edge laser spot size measurement**

As the knife-edge is stepped, measurements of the laser power behind the knife-edge are recorded and plotted against distance, similar to figure 3 - 13. Using this plot and equations 3 - 3 and 3 - 4 below, the maximum laser power can be used to determine the spot size by measuring the distance at which the power meter reads 90% maximum power and 10% maximum power. The approximation of the beam radius is

$$\beta^{-1} = 0.552(\chi_{10} - \chi_{90}) \tag{3-3}$$

where $\beta^{-1}$ is the approximation of the beam radius; $\chi_{10}$ is the x position where laser power falls to 10% maximum; and $\chi_{90}$ is the x position where laser power falls to 90% maximum. The diameter, d, can be calculated as

$$d = 2\sqrt{2\beta^{-1}} \tag{3-4}$$

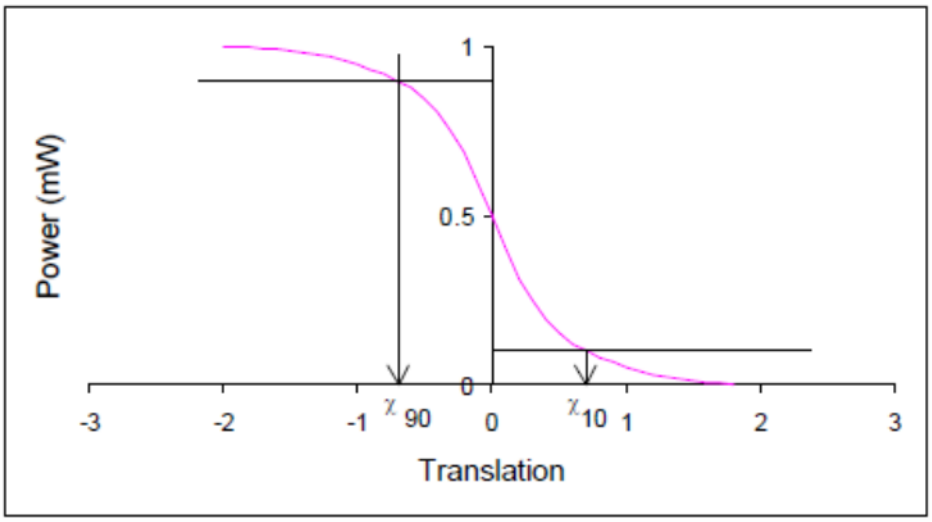


**Figure 3 - 13 Knife-Edge Experiment displaying points of 10% and 90% maximum laser power**

Knife-edge experiments were performed with and without collimation of the laser beam. To provide maximum accuracy of excitation of a region, all subsequent experiments are performed using the collimated setup unless described elsewise. In the collimated setup, a 10x Galilean beam reducer (Thorlabs, BE10M) was used to minimize the spot size. The results of the non-collimated and collimated laser spot size measurements can be seen in figure 3 - 14 below. The laser was attenuated to 5 mW and can be seen to reduce slightly in the collimated setup due to optical power loss in the lenses of the beam expander. The knife-edge was stepped across the beam in 20 μM steps and the transmitted laser power was recorded using an optical power meter.

As expected, the non-collimated knife-edge data shows an obviously larger spot size. Using the data collected in figure 3 - 14, it was shown that the laser spot size pre- and post-collimation was 3.22 mm and 1.9 mm respectively.

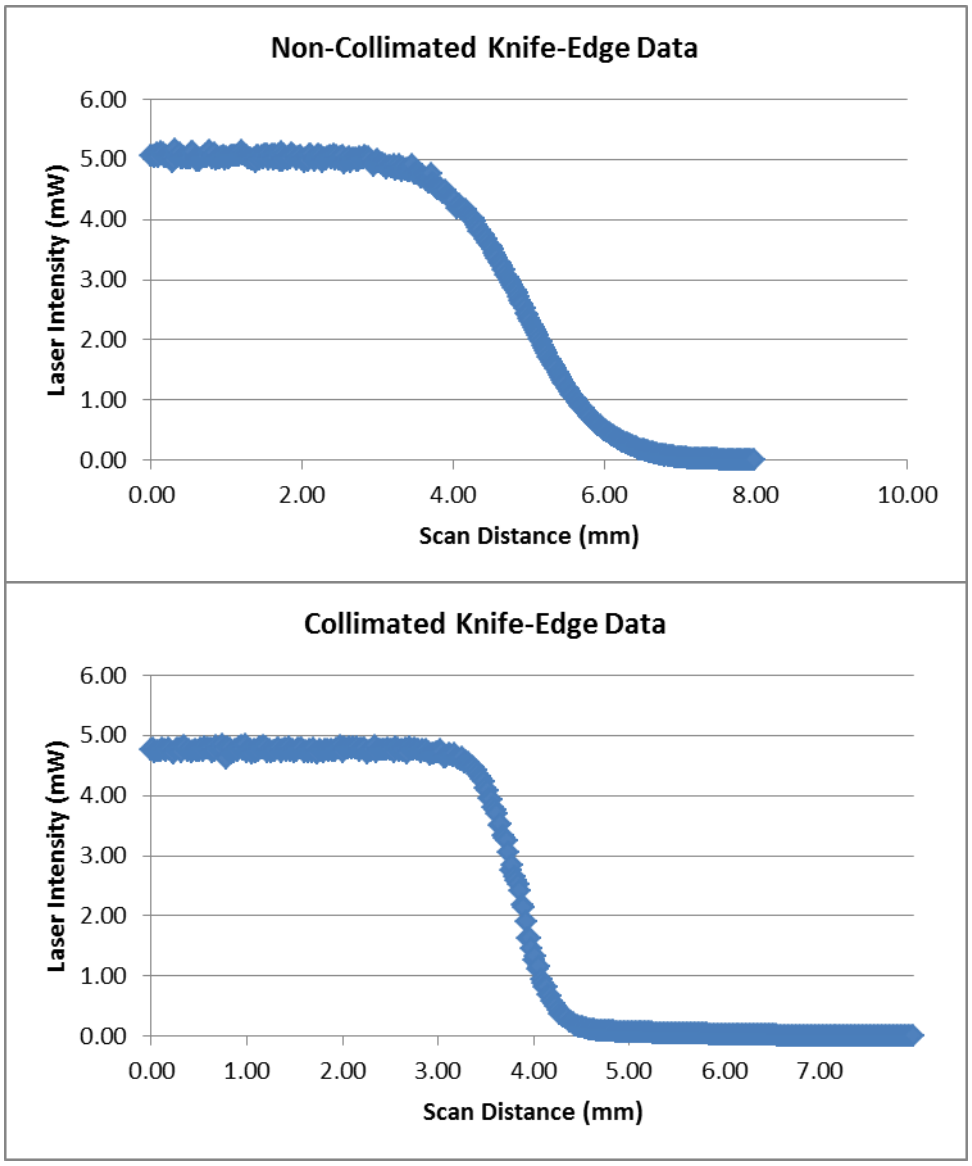


**Figure 3 - 14 Knife-Edge Laser Spot Measurement (top) non-collimated (bottom) collimated**

### 3.5 Optical Power Loss

It is also necessary to understand the potential losses of optical power inherent throughout the system. Each surface that light passes through in the system leads to a loss in optical signal due to reflections on both surfaces of each optical component. A diagram of the optical components and thus sources of loss can be seen in figure 3 - 15.

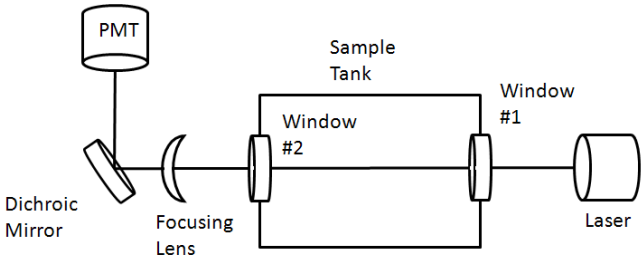


**Figure 3 - 15 Optical system setup**

We measured the optical loss of each optical component by placing continuous wave (CW) 532 nm laser light into the system and taking measurements of the laser power before and after each component in the system. The total losses are needed to predict the expected signal output of the system after all optical components before the light enters the photomultiplier tube.

The experimental setup consisted of 25.1 mW, 532 nm laser light shone through the system with the PMT covered and powered off. Table 3 - 2 gives the measured power loss for each component and the system as a whole. Of note, the total optical power loss for the system is 41 % as the power loss was measured at 10.3 mW. This number is useful when measuring the laser power directly but the system is designed to measure emitted fluorescence light from a source and thus only the optical power loss of the system starting from inside the tank is then relevant. The potential points of power loss in this instance are window 2, focusing lens, and dichroic mirror. This power loss is measured at 29.9% (6.3 mW).

**Table 3 - 2 Optical Power Loss of the System and the optical elements within the system.**

| Component | Laser Power After (mW) | Percent Loss (25.1 mW starting) |
|---|---|---|
| Window 1 | 21.1 | 15.9 |
| Window 2 | 17.3 | 18.0 |
| Focusing Lens | 16.1 | 6.9 |
| Dichroic Mirror | 14.8 | 8.1 |
| Total System | 14.8 | 41 |
| Sample Emission Loss | 14.8 | 29.9 |

### 3.6 Signal Detection

The system characteristics of ultrasound focal zone, laser spot size, and optical power loss all contribute to the amount of signal generated or the amount of signal that reaches the detector. The sensitivity for detecting optical signals is the other key feature of the system. In order to understand the abilities of the system to detect signal, we performed direct measurements of the characteristics of the PMT detector's linearity and noise equivalent power/sensitivity. These two measurements are of particular interest because they explain the limit to which a signal can be detected by the detector and to what extent the detector stays true in its output for a given signal level.

#### 3.61 Photomultiplier Linearity

Ideally, the photomultiplier tube will have a linear response in output voltage as input power rises or falls [91, 92] and therefore the linearity of the detector response to an input was measured. The setup of the procedure can be seen in figure 3 - 16. Laser light (4 mW, 532 nm was transmitted through a series of neutral-density (ND) filters (#1.0, 2.0, 3.0, and 4.0) and the output of the optical power meter and the PMT was recorded for comparison. The power meter head was used to measure the laser power output just before entering the PMT. Laser power

entering the PMT was recorded after each change of the ND filter and then the power meter head was removed to allow recording of the power via the PMT detector. The maximum PMT value was estimated at 10 times the value of 919 mV measured with the ND #1.0 filter. This was done to reduce the risk of damage to the PMT detector. The results can be seen in Figure 3 - 16. The PMT showed good linearity over five decades of laser power input. It was unnecessary to exceed the 4 mW laser power input to the detector as no signals we will measure will reach that level and anything larger might damage the PMT detector.

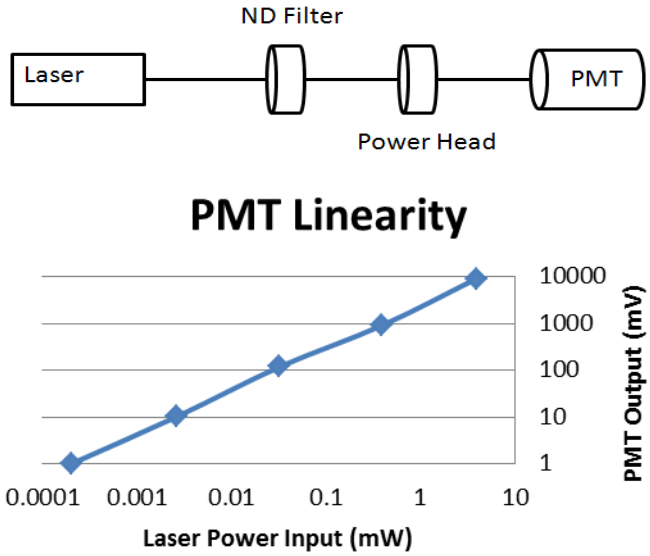


**Figure 3 - 16 Characterization of PMT linearity (Top) Experimental Set-up for PMT Linearity measurement. (Bottom) PMT Linearity Data.**

### 3.62 PMT Detector Sensitivity

The sensitivity of the PMT detector was also quantified. Sensitivity can be explained using two definitions, responsivity and noise equivalent power (NEP) [91, 92]. In our application, noise equivalent power is more indicative of the sensitivity of the detector, as the recording of AO signal is done with an abundance of noise. Thus, we report NEP as our measure of detector sensitivity.

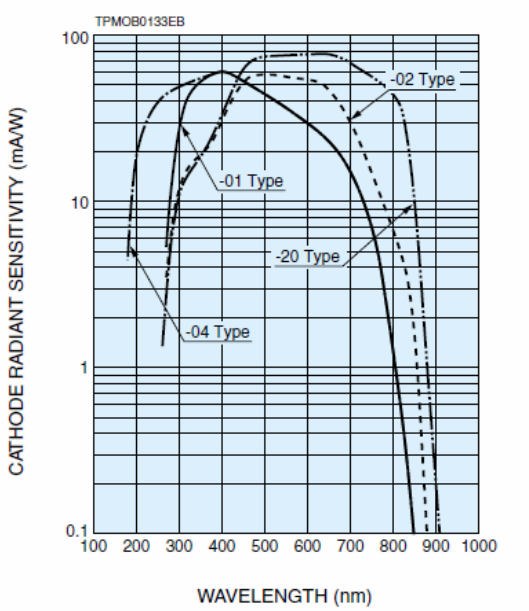


**Figure 3 - 17 Responsivity curve for the Hamamatsu H5783 -20 PMT detector.**

### 3.63 Responsivity

Detector responsivity is a measurement of the output of the detector per unit input, usually reported in A/W [91-93]. It describes the effectiveness of the detector in its conversion of light input to electrical output. Responsivity is useful in converting the detector's output to the power of the signal that is being input on the face of the detector. Changes in excitation wavelength, bias voltage, and temperature can all affect the measured responsivity of a PMT detector. The H5783-20 detector used in our set-up generates a voltage output, the responsivity of which is described by the equation:

$$R = \frac{V}{E_e A} \tag{3-5}$$

where $V$ is the RMS signal voltage output of the detector; $E_e$ is the incident irradiance $\frac{W}{cm^2}$; and A is the irradiated area of the detector $\left(cm^2\right)$. Measurement of responsivity requires a broadband source or a multitude of sources that cover the detection wavelength range of the

PMT. Here the responsivity of the PMT detector was assumed to be 78 mA/W, in the responsivity curve provided by Hamamatsu shown in figure 3 - 17.

### 3.64 Noise Equivalent Power/Sensitivity

In AO imaging, the modulated acousto-optical signal must be separated from a variety of noise sources including excitation light and unmodulated fluorescent light, as well as the standard noise sources inherent to all optical imaging techniques [94]. Thus sensitivity connotes ability to observe significant signal relative to random background noise. Noise Equivalent Power (NEP) can be defined as the input optical power at which the SNR of the detector is unity [93]. Thus NEP gives the value at which the power of the signal measured is equivalent to the noise in the system [91, 92]. It allows a prediction of the smallest signal that can be detected by the PMT. The NEP can be estimated as

$$NEP = \frac{E_e A_d}{\frac{V_s}{V_n}} \tag{3-6}$$

where $E_e$ is the irradiance on the detector surface $\left(\frac{W}{cm^2}\right)$; $A_d$ is the sensitive area of the detector $\left(cm^2\right)$; $V_s$ is the RMS signal voltage at the output of the detectors; and $V_n$ is the RMS noise voltage of the output of the detector. Using equation 3 - 6 and the experimental set-up in figure 3 - 18, NEP was measured for the system. Laser light was attenuated to 1 mW and transmitted through a neutral-density #1.0 filter allowing a 0.108 mW laser power to enter the system. The laser light was then modulated at 1 MHz using an acousto-optical modulator (AOM) and allowed to shine on the PMT detector. The output of the detector was connected to a signal analyzer (N9010A ExA Signal Analyzer, Agilent Technologies) with a center frequency of 1 MHz and a bandwidth of 9.1 kHz. The RMS voltage was measured using the signal analyzer and the NEP was calculated. Noise voltage was recorded with the PMT blocked and then signal voltage

at 1 MHz was recorded. Using the signal analyzer, the power peak was measured at the 1 MHZ signal peak. Next the laser power was doubled and the NEP power peak at the 1 MHz signal peak was measured as the NEP of the system [91]. The measured NEP for the PMT was 125.8 pW. However, the PMT sensitivity does not take into account the lock-in detection scheme and the corresponding minimum detectable fluorescence of the entire system.

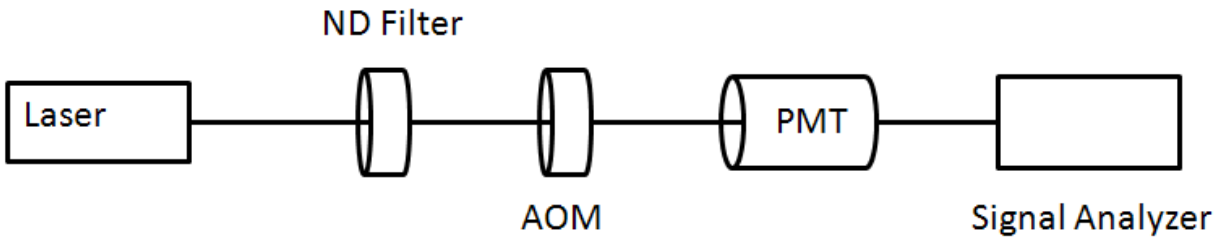


**Figure 3 - 18 Noise Equivalent Power Measurement Experimental Set-Up**

### 3.7 System Validation

A final step in system evaluation was validation of the system's ability to measure fluorescent signals as well as acousto-optical signals. Two initial experiments were performed to measure both of these abilities separately.

#### 3.71 Fluorescent Imaging

The system set-up for measuring fluorescent signals bypasses the lock-in amplifier (seen in figure 3 - 5) and the fluorescent signal is allowed to enter the PMT and is recorded at the oscilloscope. The experimental set-up used to validate the system's ability to measure fluorescence can be seen in figure 3 - 19 (left). Laser light was shown into a sample tank perpendicular to the direction of the PMT detector. A falcon tube filled with 10 µM Rhodamine B fluorophore was attached to the sample arm holder and immersed in deionized water within the tank. Next the sample was stepped in the x direction across the laser beam excitation and the

fluorescent emission was recorded taking 10 samples per step. The data were then plotted against the scan distance and can be seen in figure 3 - 19 (right).

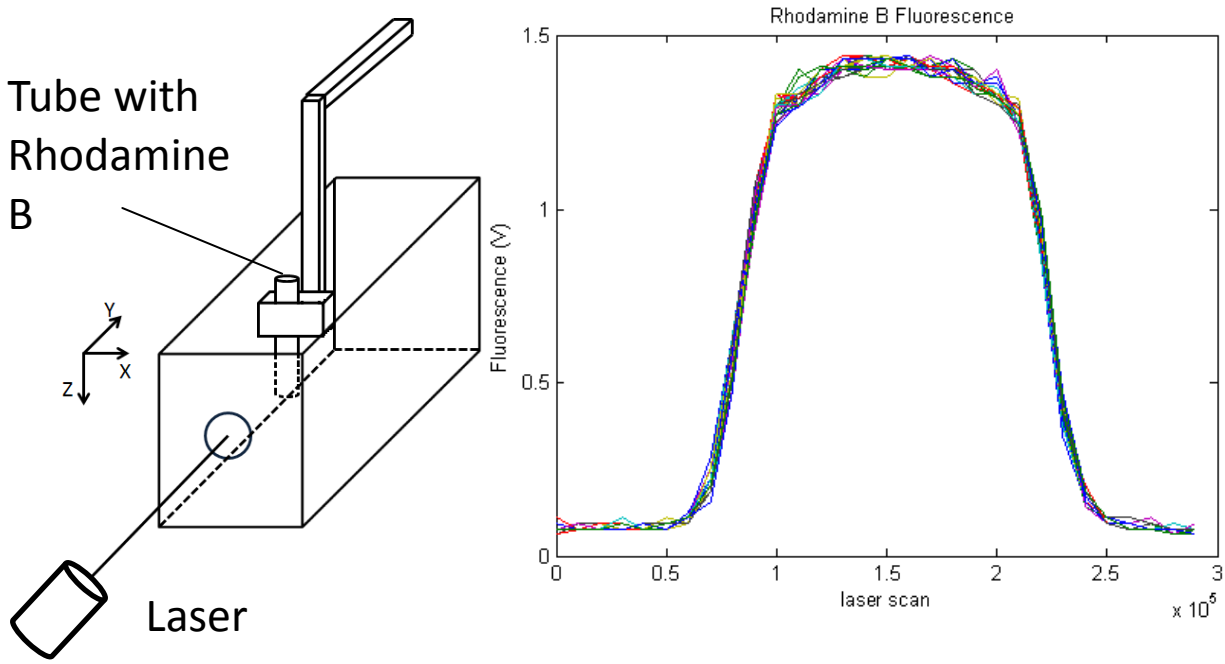


**Figure 3 - 19 Experimental validation of the ability to detect fluorescence with the designed system (left) Experimental Set-up for Falcon Tube scan of Rhodamine B fluorophore. (right) Fluorescence Data of 30 mm Scan of the Falcon Tube.**

### 3.72 Minimum Detectable Fluorescence Concentration

Using the experimental set-up in figure 3 - 19, the minimum detectable Rhodamine B concentration was measured. The laser light was modulated using an Acousto-Optic Modulator driven at 1.041 MHz with a 60 $V_{p\text{-}p}$ Sinusoidal signal. The PMT was connected to the lock-in amplifier allowing the ability to greatly improve the SNR and reduce the noise bandwidth. At a given time constant T, the lock-in detection bandwidth can be calculated as:

$$BW = \frac{1}{\kappa T} \tag{3-7}$$

where K is dependent on the specified filter selected between -6 dB, -12 dB, -18 dB, and -24 dB. These values represent the point at which the input signal is reduced by the specified dB and

the lock-in amplifier cuts off any signal after that point. For the SR844 Lock-In Amplifier, the BW can be determined based on the following:

**Table 3 - 3 Bandwidth (BW) in relation to the designated filter on the SR844 Lock-In Amplifier**

| Filter | Bandwidth |
|---|---|
| -6 dB | $\frac{1}{4T}$ |
| -12 dB | $\frac{1}{8T}$ |
| -18 dB | $\frac{3}{32T}$ |
| -24 dB | $\frac{5}{64T}$ |

The bandwidth can be greatly reduced by selection of the appropriate time constant and filter roll-off. As the filter roll-off is increased from -6 dB to -24 dB, the detection bandwidth is reduced. The detection bandwidth can also be significantly reduced by the selection of the time constant. This can be seen in figure 3 - 20.

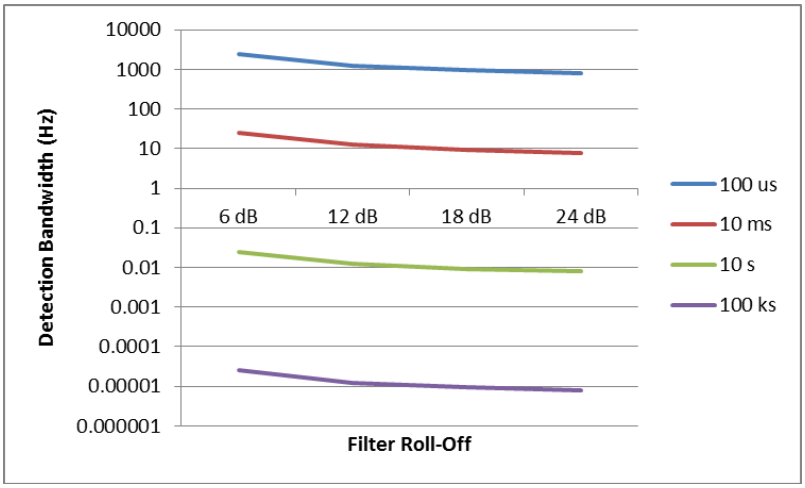


**Figure 3 - 20 Lock-In Detection Bandwidth versus filter roll-off and time constant**

The calculated detection bandwidth can be used to calculate the equivalent noise in the detection bandwidth (ENBW) which allows the calculation of the minimum detectable signal for the lock-in amplifier. ENBW can be calculated as:

$$ENBW = input\ noise \times \sqrt{Bandwidth(Hz)} \times gain \tag{3-8}$$

Where the input noise is $\frac{2nV}{\sqrt{Hz}}$ as specified by the manufacturer and the gain is 20 dB. As seen in figure 3 - 21, the noise within the detection bandwidth can again be significantly reduced as by selection of the appropriate time constant and filter roll-off. However as the time constant is increased, the system response time is greatly affected and the need to compromise between maximum sensitivity and experiment length arises. For all subsequent experiments we selected a 10 s time constant and -12 dB filter unless otherwise noted. This selection provides a 12.5 Hz detection bandwidth with noise in the detection bandwidth equaling 22.4 nV.

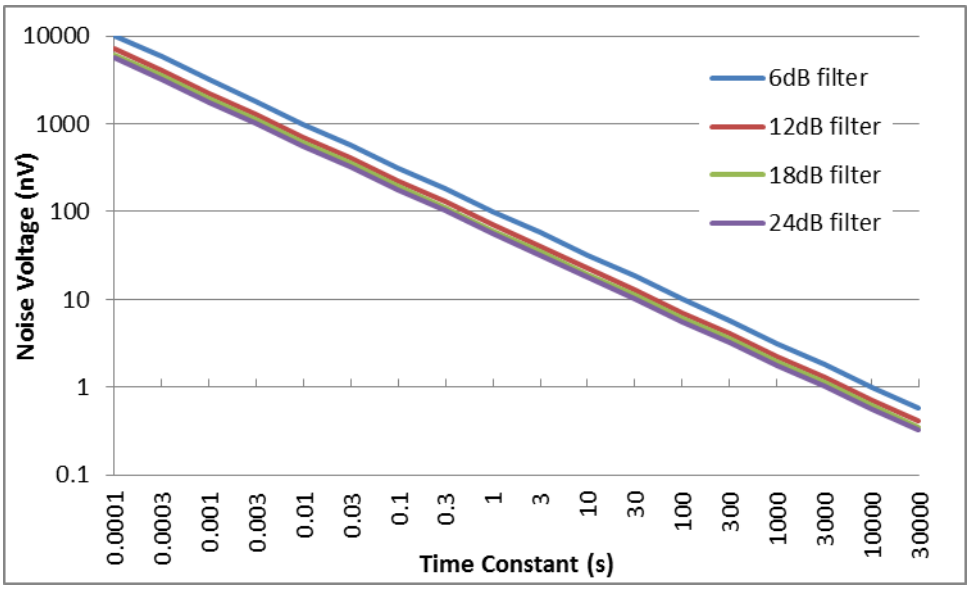


**Figure 3 - 21 Lock-In Noise in the Detection Bandwidth versus filter roll-off and time constant**

With the selection of an appropriate time constant and filter roll-off, the minimum detectable concentration was calculated as follows. Serial dilutions of Rhodamine B ranging from 4.43 nM

to 221.5 nM were placed in 1 cm cuvettes and fluorescence signal amplitude was measured for each dilution individually using the experimental set-up in figure 3 - 19 using a 1 mW excitation power. The results can be seen in figure 3 - 22. A linear fit of the data shows an $r^2$ value of 0.963. Furthermore, the y intercept of the linear fit gives a reasonable expectation of the noise voltage recorded with no fluorophore within the system. The measured amplitude of the system noise was 86.76 nV. Assuming a detection limit at SNR equal to 1, the amplitude can be placed in the equation of the linear fit and the minimum detectable concentration of Rhodamine B can then be calculated. The result is a minimum detectable concentration of 6.18 pM at the specified 10 s time constant equating to a 12.5 Hz bandwidth. This minimum detectable concentration can then be decreased or increased based on selection of the time constant.

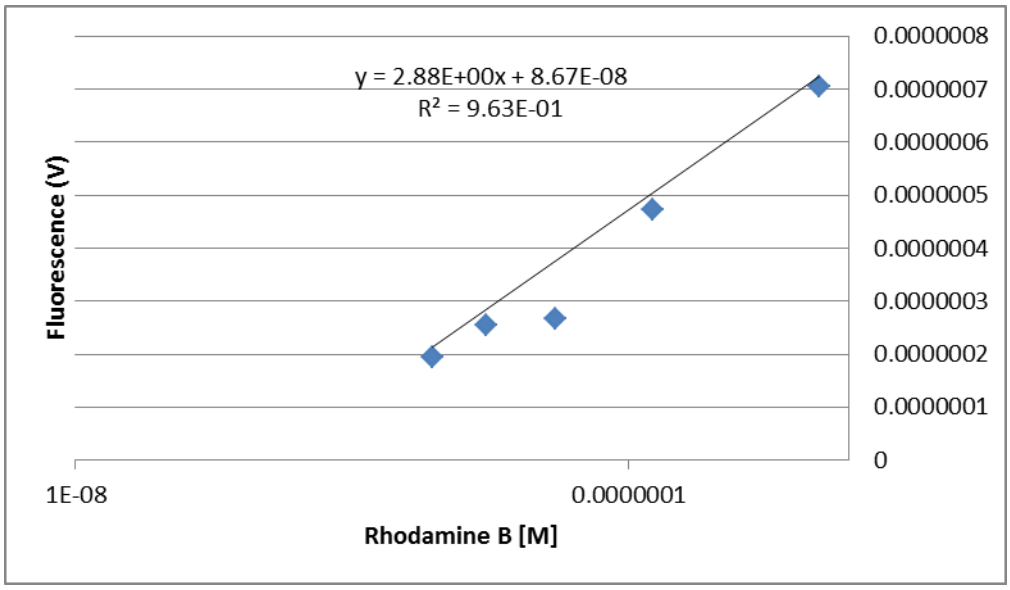


**Figure 3 - 22 Linear fit of Rhodamine B concentration to determine minimum detectable Rhodamine B [M]**

### 3.8 Acousto-Optic Imaging

To measure modulated acousto-optical signals, the modulation frequency is supplied to the lock-in amplifier via the waveform generator and the lock-in amplifier detects any modulated signal at the same frequency being received from the PMT detector.

Using the experimental set-up shown in figure 3 - 5, we focused the ultrasound focal zone and laser light source at the intersection of the inner diameter of a silicon tube running through the sample tank (figure 3 – 23). In this set-up, the laser traveled in the direction perpendicular to the PMT detector face such that emission light could be recorded with minimal excitation noise. Next the voltage (and thus acoustic pressure) supplied to the transducer was stepped in an increasing fashion and AO signal/Ultrasound Modulated Fluorescence (UMF) was recorded with the lock-in amplifier.

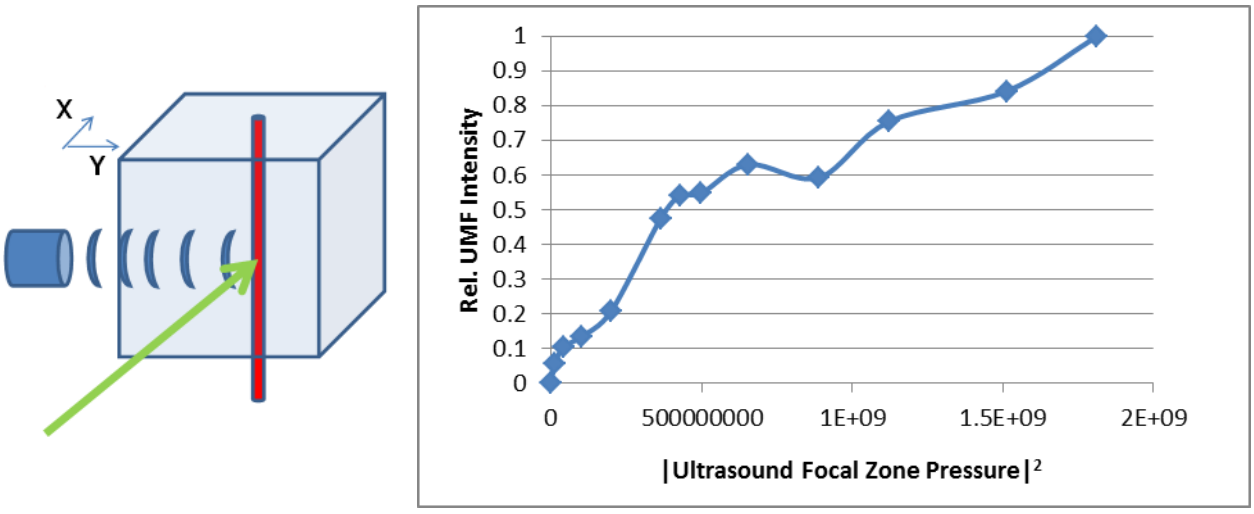


**Figure 3 - 23 (Left) Initial UMF Rhodamine B filled Silicon Tube Set-up (Right) UMF in relation to Ultrasound RF pressure.**

The data showed that the system was capable of measuring ultrasound modulated fluorescent signals. As expected, the results show that the ultrasound modulated fluorescence increased linearly ($R^2$=0.88) with the square of the ultrasound pressure.

### 3.9 Conclusions

We have developed a state-of-the-art Acousto-Optical Imaging system capable of measure both modulated and unmodulated light signals. Laser excitation can be performed with a 6W, 532 nm DPSS laser with a spot size between 1.9 and 3.22 mm. Ultrasound can be introduced into a sample with a focus spot size of 5 mm and pressure up to 62 kPa. The lock-in detection scheme can measure 6.18 pM of Rhodamine B or 98.6 pW of signal. All of these characteristics are similar to those of systems previously reported by others and initial experiments to measure Acousto-Optical interactions show that the system is capable of performing AOI experiments.

# Chapter 4

## Ultrasound modulated fluorescence is dominated by the fluorescent emission signal caused by the interaction between modulated excitation light and the fluorophore

### 4.1 Introduction

Recently, measurement of ultrasound-modulated fluorescence (AOM) has been proposed as a potential solution to the shortcomings of standard optical imaging techniques [55, 56, 58, 59]. AOM is created by focusing an ultrasonic sound beam into the ROI to modulate either the excitation [58] or emission light of the fluorophore, or possibly the fluorophore itself in terms of concentration, quantum yield, or lifetime [55, 59]. As mentioned in chapter 1, Acousto-Optical Imaging (AOI) is an emerging multi-modal imaging technique being developed to improve optical localization of fluorescent contrast in traditional fluorescence tomographic imaging. AOI uses the detection of AOM to combine the inherent spatial resolution of ultrasound imaging and the optical contrast of fluorescence imaging to enhance localization of a fluorescent region. In chapter 1, details of the interactions between ultrasound and light that allow the combination of the two to form a measurable Acousto-Optical signal were described. These interactions have been observed and are well detailed between ultrasound and coherent exciting light sources. However, until recently the Acousto-Optical interaction between ultrasound and incoherent light produced in response to excitation was believed to be too small to observe [15].

To date a few groups have reported studies of the ultrasonic modulation of incoherent fluorescent light. Kobayashi et al. were the first to experimentally observe Acousto-Optical interaction between ultrasound and incoherent light. They described successful imaging, with high resolution, of regions of fluorescent contrast using AOM in turbid media tissue phantoms and porcine tissue samples [56, 57, 95]. This chapter will detail the experimental research we have performed to repeat the Kobayashi experiments in an attempt to elucidate the mechanism

of ultrasonic modulation of incoherent light emitted from a fluorophore and to quantify the factors that affect its magnitude.

### 4.11 Kobayashi et al. Experiments

Kobayashi et al. developed a system to demonstrate the ability to ultrasonically modulate fluorescent light and image tomographically [56, 57]. The system set-up for their initial experiments can be seen in figure 4 - 1 (A). This system was modified for their second experiments to include a Ti:Sapphire laser which allowed the use of a near-infrared wavelength (NIR) to improve upon depth penetration of the excitation light. The modified system can also be seen below in figure 4 – 1 (B).

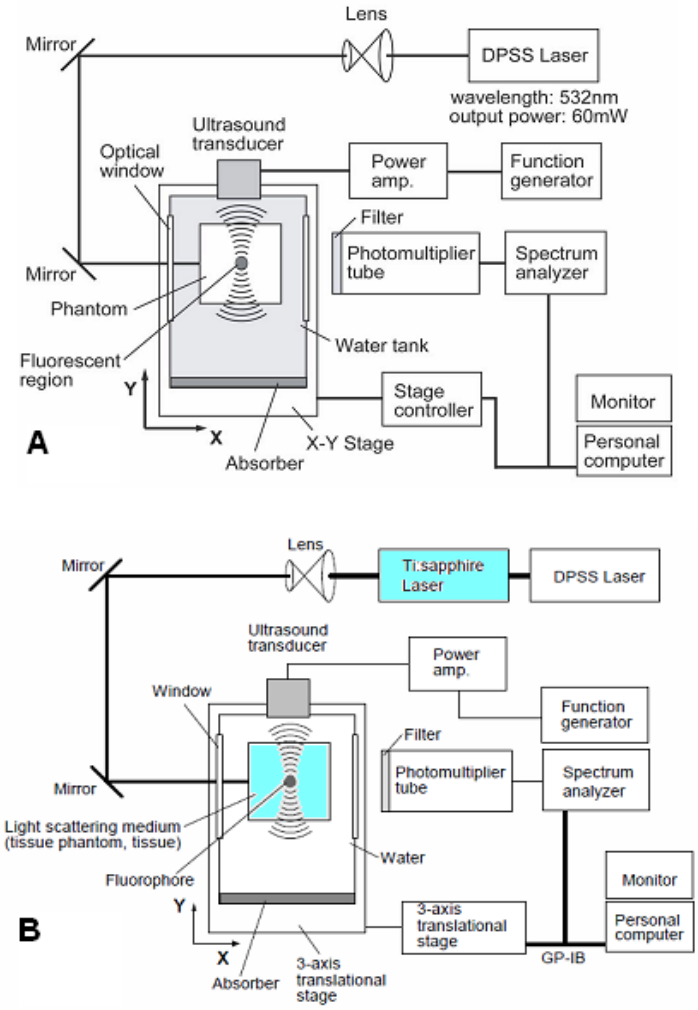


**Figure 4 - 1 (A) Schematic of Kobayashi *et al.* experimental set-up for 532 nm wavelength. (B) Schematic of the experimental set-up at 726 nm wavelength. [Adapted from Kobayashi 2006 and 2007]**

Using the system set-up in figure 4 – 1 (A), a tissue phantom was illuminated using a 532 nm diode pumped solid state (DPSS) laser at 60 mW beam intensity with a 1 mm diameter spot size. A 1 MHz focused ultrasound transducer with 38 mm focal length and 3 mm focal diameter was used to modulate light passing through the focal zone. The transducer was driven by a function generator producing a continuous sinusoidal wave which was directed into the side wall of the tissue phantom incident perpendicular to the incident laser light. The measured sound pressure in the ultrasound focal region was 41 kPa. A photomultiplier tube (PMT) of unknown manufacture and specifications was used to detect the signal which was delivered to a spectrum analyzer, and the intensities of light signals detected at the sound frequency (1MHz) were measured over a 100 Hz bandwidth. By mounting the transducer on a two-axis translational stage and placing the tissue phantom in a water tank, two-dimensional tomographic images of fluorescence intensity were obtained by translating the US beam in 500 μm steps in both the x and y directions.

An initial experiment was performed with the US beam and laser excitation light incident perpendicular and crossing in the center of the fluorescent region. The results showed that the fluorescence modulation intensity increased proportionally to the square of the increasing sound pressure giving a linear relationship between sound intensity and AOM, seen in figure 4 – 2 (A).

The next experiment involved the use of localized fluorescent region embedded in a turbid media tissue phantom. The phantom was prepared by first diluting Intralipid in 5% agar to create an isotropic light-scattering media. The gel was then poured into a mold measuring 40x40x75 $mm^3$. The final volume concentration of Intralipid was 40 ml/l Intralipid in 5% agarose gel with water-glycerin (20%) solution. A fluorescent region, consisting of fluorescent microspheres with 530 nm absorption peak and 590 nm emission wavelength, was embedded in a column of agarose gel 5 mm long and 3 mm in diameter. The phantom can be seen in figure 4 – 2 (B).

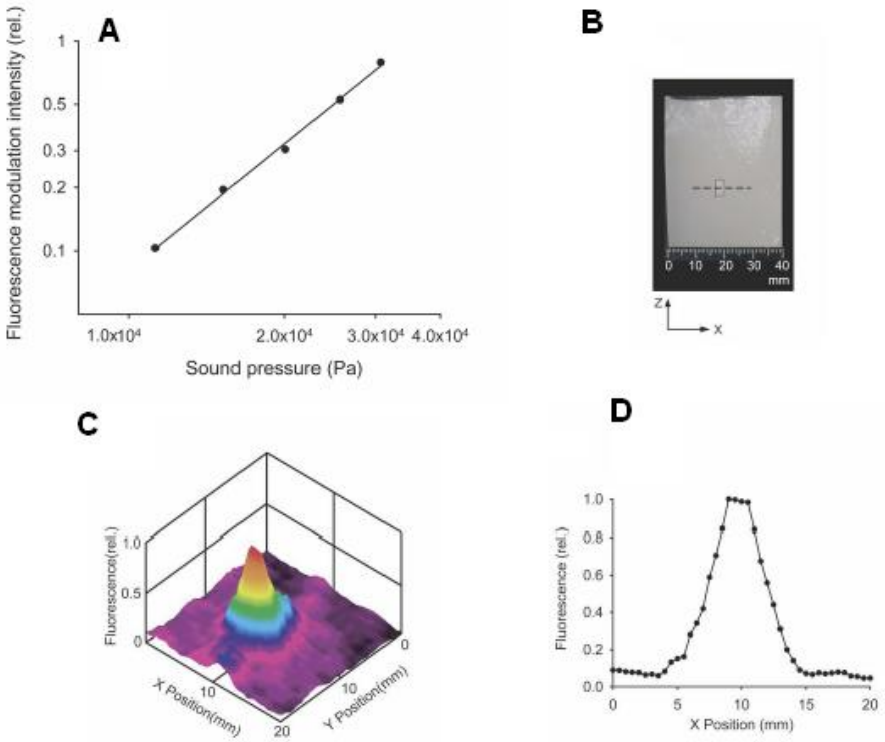


**Figure 4 - 2 Kobayashi et al. experimental results (A) Fluorescence modulation intensity as a result of increasing sound pressure. (B) Photograph of embedded fluorescent region in the tissue phantom. (C) 2-D tomographic image of modulated fluorescence intensity. (D) Fluorescent intensity along the x-axis. Modified from Kobayashi 2006.**

Next using the system in figure 4 – 1 (A), the ultrasound was scanned in two dimensions (XY plane covering 20x20mm of the phantom) over the Intralipid agar gel tissue phantom and AOM was recorded. As can be seen in figure 4 – 2 (C) and (D), they were able to localize ultrasound modulated fluorescence in two dimensions (XY plane scan of intensity measurement). A full width half max measurement on the x-axis profile of AOM determined the region to measure 3 mm coinciding with the actual 3mm size of the fluorescent region. In a repeat experiment, they again used an Intralipid tissue phantom but with two regions of fluorescent microspheres separated by a 9 mm gap along the x-axis, seen in figure 4 – 3 (c). Again the results show the ability to localize AOM to only the fluorescent regions in both one and two dimensions, seen in figure 4 – 3 (a) and (b).

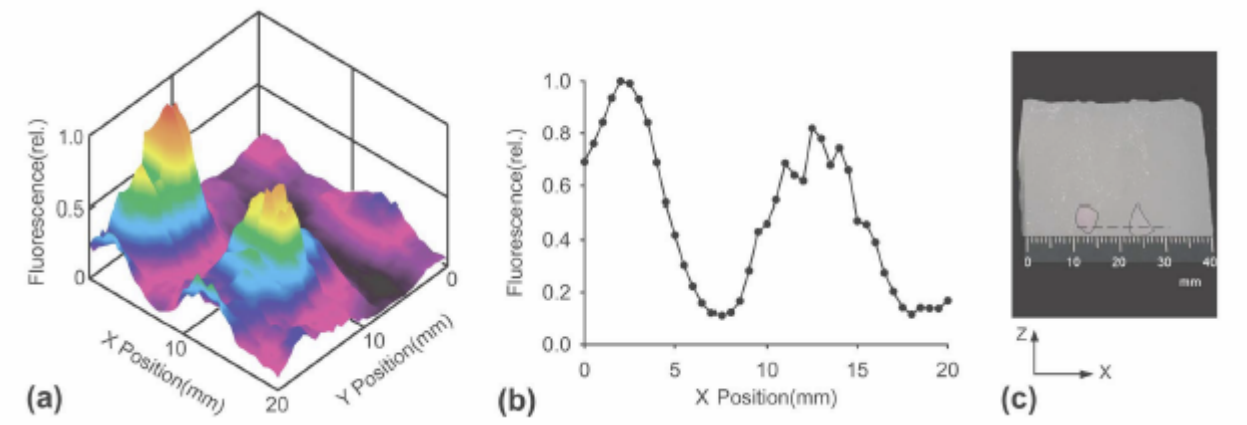


**Figure 4 - 3 Kobayashi et al experimental results for two embedded regions (a) 2-D tomographic image of modulated fluorescence intensity. (b) AOM along the x-axis. (c) Photograph of two embedded fluorescent regions in the tissue phantom. (Adapted from Kobayashi et al 2006)**

Their results demonstrated that fluorescence can be modulated and that ultrasound modulated fluorescent signal can be imaged tomographically. However their results are not interpretable unambiguously. They inferred that the modulation is induced by density variations of the media induced by the ultrasonic field. They stipulate that these density variations cause changes in the index of refraction as well as the optical scattering coefficient of the medium [56]. These explanations have previously been accepted for ultrasonic modulation of coherent light but until this point have not been shown for incoherent modulation. From the profiles reported, it appears that there was no significant modulation of the incident coherent light prior to its exciting the fluorophore. It was concluded that, with the application of near-infrared excitation light and a suitable NIR absorbing/emitting fluorophore, this technique could be applicable to measure modulated fluorescence in biological tissue.

Next, Kobayashi et al. performed a set of experiments using a pair of tissue phantoms, one Intralipid turbid gel phantom and one porcine tissue phantom, designed to test their hypothesis that fluorescence modulation could be recorded in biological tissue using NIR excitation light. A Ti:Sapphire laser was incorporated into their initial set-up allowing excitation wavelength at 726 nm as opposed to the 532 nm wavelength of the DPSS laser in the first

experiment. The apparatus can be seen in figure 4 – 1 (B). They also altered the final volume concentration of Intralipid in the tissue phantom from 40 ml/l to 80 ml/l and changed the fluorescent microspheres to 715 nm absorption peak and 755 nm emission peak (FluoroSpheres F-8799, Molecular Probes Inc.). They then performed a 2-D scan recording ultrasound modulated fluorescent intensity at each scan point similar to their previous experiment. The results can be seen in figure 4 - 4.

Similar to their first experimental results, Kobayashi et al. were again able to localize a fluorescent region in a turbid media phantom by recording ultrasound modulated fluorescent signal from the region. As can be seen in figure 4 - 4, the experimental results resolved the fluorescent region in two dimensions. Again the full width half maximum measurement they reported of the ultrasound modulated fluorescent intensity along the x-axis scan was a width of roughly 3 mm although visual inspection of the x axis intensity seems to be ~5mm. The 3 mm they measured corresponds with the actual measured diameter of the fluorescent region. They doubled the Intralipid concentration from their initial experiments, and concluded that with the increased scattering in the new phantom further experiments could be done to determine if AOM can be used to localize a fluorescent region in biological tissue.

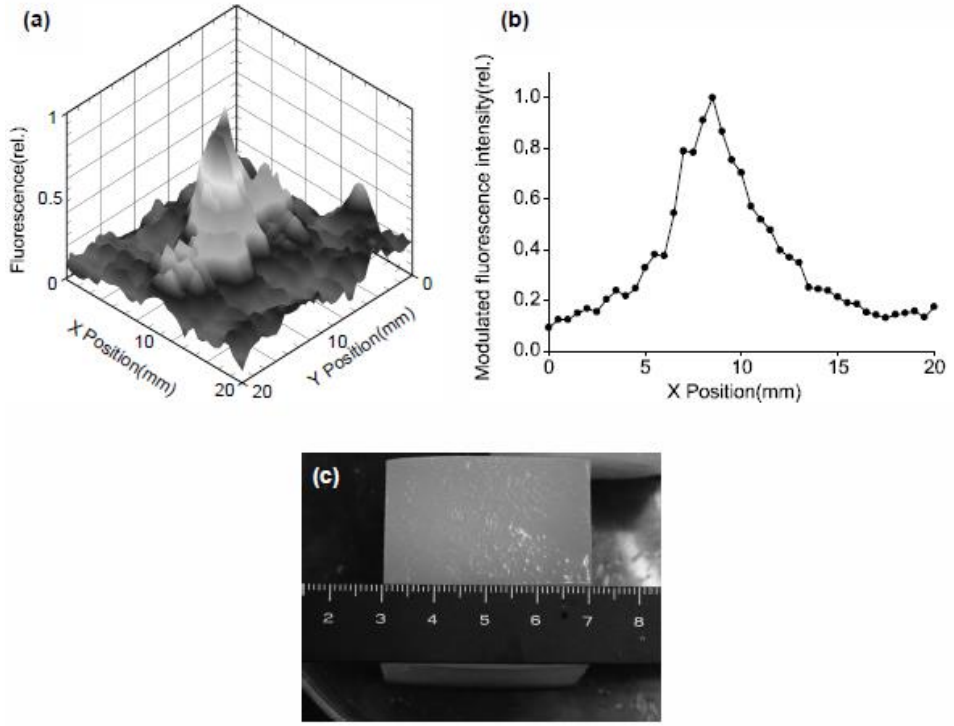


**Figure 4 - 4 Kobayashi et al. experimental results for a single embedded region (a) 2-D tomographic image of modulated fluorescence intensity. (b) AOM along the x-axis. (c) Photograph of the Intralipid tissue phantom. (Adapted from Kobayashi et al 2007)**

Next a biological tissue phantom was created by placing porcine muscle tissue obtained from a grocery market in the sample mold forming a phantom the same size and shape as the prior Intralipid gel phantoms (figure 4 – 5 (c)). A fluorescent region was embedded in the phantom as done in previous experiments. One and two dimension scans of ultrasound modulated fluorescence were performed using the apparatus of figure 4 – 1 (B). The results were similar to that in the Intralipid phantom studies. They were capable of localizing fluorescent in the center of the porcine tissue phantom in two dimensions. This can be seen in figure 4 - 5 (a) and (b). Again, full width half maximum measurement of 3mm was reported despite visual inspection of the data seeming to put this measurement closer to 5 mm. These results agreed with their previous studies and suggest that ultrasound modulated fluorescence can be used to localize regions of interest containing fluorophores of interest. Based on their results, they

demonstrated that modulated fluorescent signals could be imaged up to 30 mm in depth, which would be useful for both rats and mice. However again they failed to explain further the modulation mechanism that allows the ultrasonic interaction with only the incoherent emission light allowing them to localize the fluorescent region [57]. In theory, laser light interacting with the ultrasound focal zone before the fluorescent region will cause ultrasound modulated excitation and therefore modulated fluorescence from the fluorescent region (at the wavelength of the fluorophore and the frequency of the ultrasound). However they apparently are able to completely remove any trace of this effect to image a signal that is presumably many times smaller.

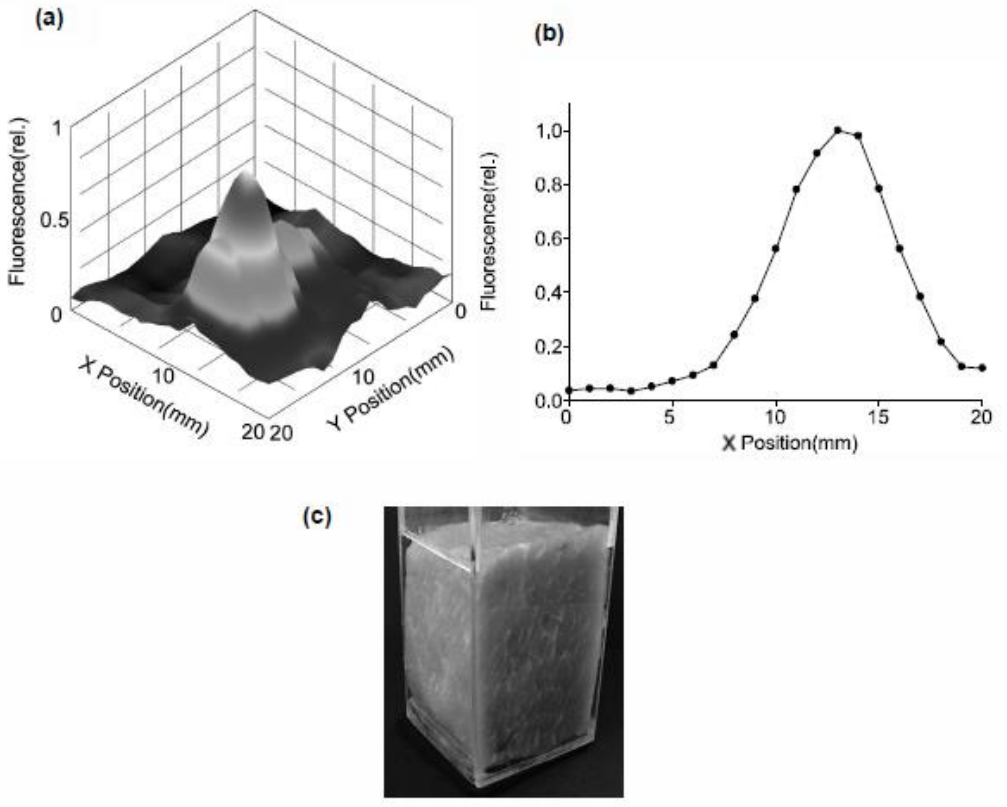


**Figure 4 - 5 Kobayashi et al. experimental results for a single region embedded in porcine tissue (a) 2-D tomographic image of modulated fluorescence intensity. (b) AOM along the x-axis. (c) Photograph of porcine tissue phantom. (Modified from Kobayashi et al 2007)**

Given the promise of these studies, we performed the following experiments to understand and build upon their results. Based on the lack of an explanation of the mechanism that drives these interactions, this work was performed to further elucidate the mechanism of modulation and assess the factors that affect the optical signals.

## 4.2 Materials and Methods

### 4.21 Acousto-Optical Imaging System

We designed, developed, and tested a state-of-the-art system capable of imaging Acousto-Optical interactions. A detailed description of the system was provided in chapter 3. The system schematic used for experiments can be seen in figure 4 - 6.

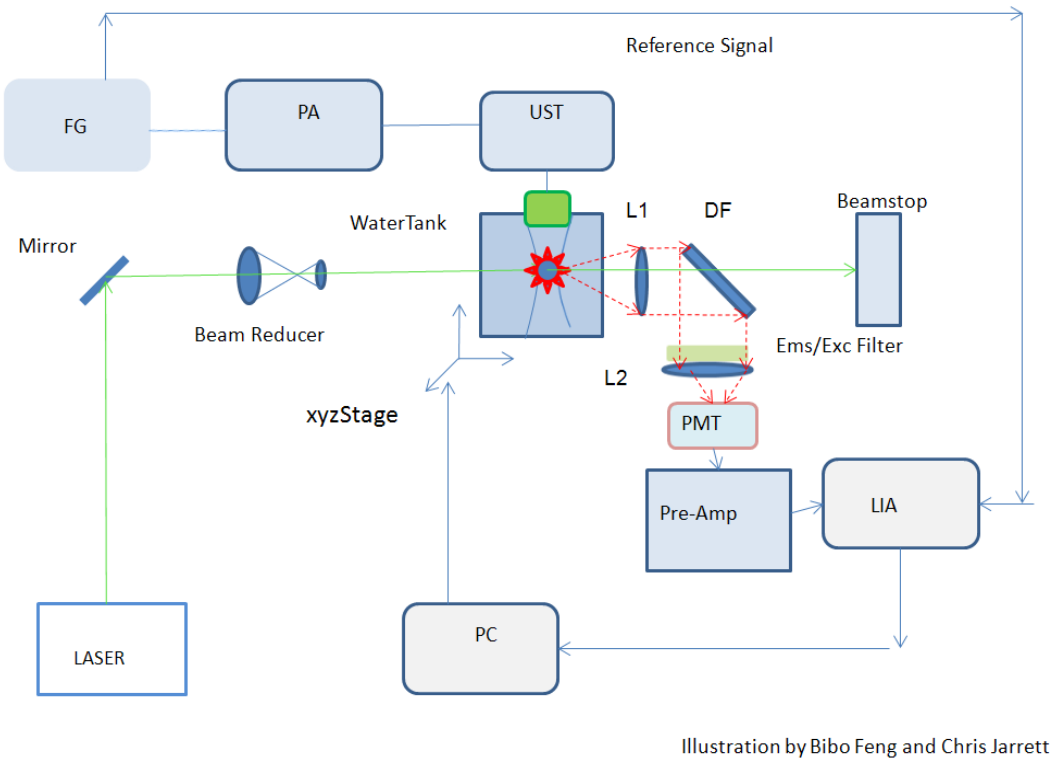


**Figure 4 - 6 Schematic of the custom designed AOI system.**

### 4.22 Development of Optical Tissue Phantoms

It was necessary to develop custom optical tissue phantoms to repeat the experiments performed by Kobayashi et al. as well as to be used for additional AO experiments. We modeled our tissue phantom after that of Frangioni et al. due to the components of these phantoms being readily modified to vary the optical properties by varying specific ingredients [96]. These phantoms closely mimic the phantoms utilized by Kobayashi et al. but NF grade gelatin was used instead of agarose gel.

The phantoms consist of a combination of deionized water, NF grade gelatin, and 10x tris-buffered saline (TBS). Tissue phantoms were developed roughly 40x20x40 mm in size. To fill a phantom mold of this size, 100 mL of phantom solution was created using 86 mL deionized water, 10 mL TBS, and 10 grams NF grade gelatin. The deionized water and TBS was mixed in a 150 mL beaker and heated on a hot plate. The temperature was monitored so that the mixture did not reach boiling. While stirring the mixture, the gelatin was added slowly to minimize clumping. Because of initial experiments showing no AOM signal reaching the PMT when embedded in an Intralipid phantom, we used optically transparent phantoms for our experiments. Thus, no additional ingredients initially were added to increase the turbidity of the phantom. After the gelatin powder was added to the heated liquid it was allowed to dissolve for five minutes. The mixture was then removed from the heat source and allowed to cool to just above room temperature. Once cooled, the mixture was poured into custom molds of the desired size, covered, and placed in a refrigerator for 8 hours. The phantom solidifies within an hour in the refrigerator but to maximize the solidity of the phantom and prolong the life span, a minimum of 24 hours refrigeration allows the phantom to last for 1 week under ideal experimental conditions. When not in use the phantom was kept in the refrigerator to prolong its life.

### 4.23 Embedding Contrast Agents in Regions of Interest

To repeat the experiments of Kobayashi et al., it was necessary to embed target regions of fluorescent agent within the phantom. It is very difficult to embed a liquid agent into a gelatin phantom both before and after it solidifies. Short of inserting rigid containers to hold the contrast agent, attempts at embedding regions of contrast before the gel solidified were unsuccessful. Thus the procedure for forming the phantoms was performed in a step wise procedure as seen in figure 4 – 7 (a). First, the gel solution was made and poured into the mold saving 30 mL of solution. A special holder was made allowing the suspension of varying sized inserts to be placed into the gel solution while the gel solidified. These inserts allowed the formation of a uniform void in the gel upon removal of the insert. Next, 1 mL of the saved gel was mixed with 0.1 mL of the fluorescent microspheres. This solution was stirred and then using a syringe was injected into the opening in the top of the void to fill region with contrast agent. The phantom was then placed in the refrigerator and allowed to cool for 5 minutes ensuring the solidification of the inserted contrast regions. Finally, the remaining 29 mL of gel solution was poured on top of the phantom and allowed to cool 8 hours with the product being a single solid gel phantom (figure 4 – 7 (b)).

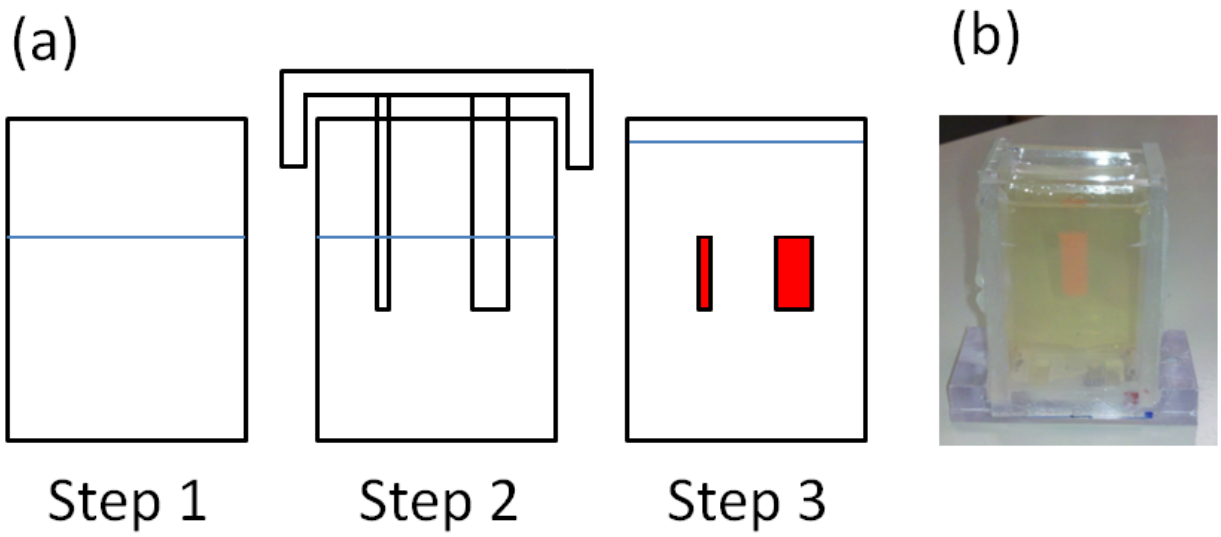


**Figure 4 - 7 (a) Stepwise procedure for embedding fluorescent regions of interest in the phantom (b) Gel phantom with fluorophore embedded**

### 4.24 Ultrasound Pressure vs. AOM signal

The first experiment to repeat the results of Kobayashi et al. was the measurement of ultrasound modulated fluorescence in relation to the ultrasound pressure in the focal zone. Laser light was directed incident to an embedded fluorescent microsphere (F-8833 540/560, Molecular Probes Inc.) region in a gelatin tissue phantom. An ultrasound transducer was introduced perpendicular to the laser excitation source such that the ultrasound focal zone coincided with the location of the fluorescent region of interest. The set-up can be seen in figure 4 - 8. Next the driving voltage (and the proportional ultrasound pressure in the focal zone) was increased in steps and ultrasound modulated fluorescence was recorded with the lock-in amplifier at each step. Based on the results obtained, the ultrasound pressure in the focal zone for all subsequent experiments was set at 43 kPa as that provided the most ultrasound modulated fluorescence signal while reducing the chance of damaging the transducer.

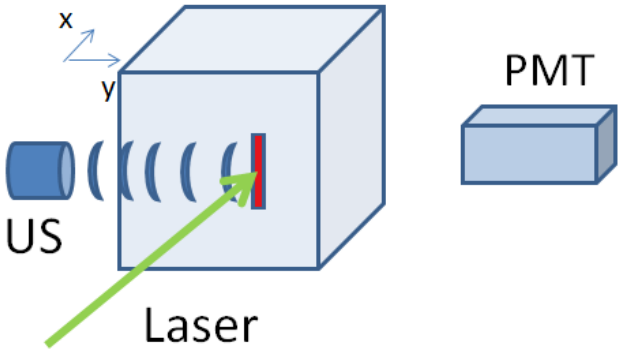


**Figure 4 - 8 Ultrasound Pressure versus Ultrasound Modulated Fluorescence Experimental Set-up.**

### 4.25 Tissue Phantom Experiments

Using the system configuration in figure 4 - 6, we next attempted to repeat the Kobayashi et al. gel phantom experiments based on the limited information given on their system specifications. An initial experiment was performed utilizing an Intralipid phantom with 40 mL/L Intralipid concentration identical to their experiment. A 2 mm region of fluorescent microspheres was embedded within the phantom and a three dimensional scan was recorded. The results were inconclusive as there was no measured AOM signal recorded within the phantom.

A subsequent experiment was performed using an identical phantom but increasing the time constant and thus the sensitivity of the detection scheme. With the 10 second time constant, the detection bandwidth was 12.5 Hz providing an equivalent noise within the detection bandwidth of 22.36 nV. With the ultrasound focused at the depth of the region of interest, AOM was recorded in a 30 mm x 20 mm scan with 0.250 mm step size.

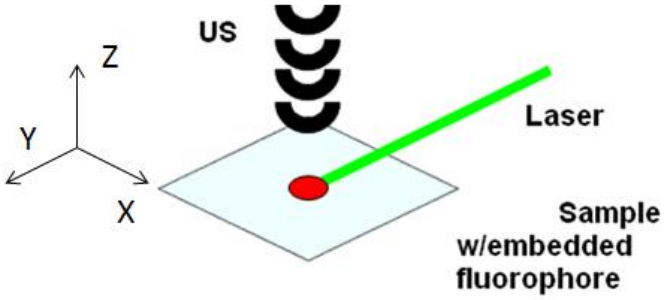


**Figure 4 - 9 Gel Phantom AOM scan experimental set-up.**

Based on the outcome of these initial scans, it was decided that optically clear phantoms (no Intralipid content) would be used in order to repeat the experiments. This allowed the interrogation of the physics involved with the mechanism of modulation while maximizing the AOM signal received at the PMT. Using an optically clear gel phantom, the ultrasound focal zone was scanned in the XY plane across the sample with the fluorophore region located in the

center of the scanned plane. The schematic for this scan can be seen in figure 4 - 9. Ultrasound modulated fluorescence was recorded over scan planes ranging from 10x10 mm to 40x40 mm during multiple scans.

### 4.26 Laser Modulation Experiments

The results of the gel phantoms experiments proved to be different from those reported by Kobayashi et al. and thus it was necessary to perform additional experiments to ensure our measured results were accurate. First it was necessary to determine if any modulated excitation light was reaching the PMT and subsequently corrupting the AOM signal. This was tested by using an optically clear phantom without a region of fluorescence. The system set-up can be seen in figure 4 - 10. AOM fluorescence was recorded in the XY plane in a 20x20 mm matrix with 0.25 mm step size. An identical scan was then performed on a sample containing a fluorescent region of interest and the results of the two scans were compared. The results from the initial fluorophore phantom experiments were then compared with the predicted excitation light through the fluorescent sample.

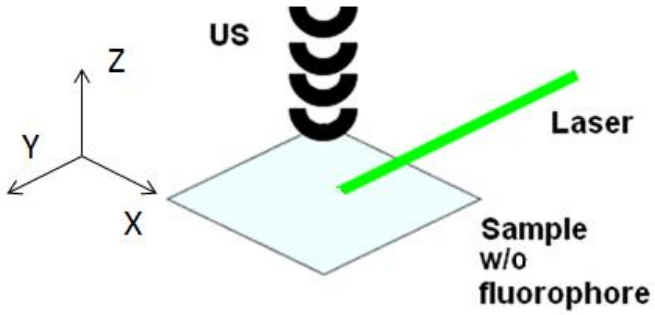


**Figure 4 - 10 Gel Phantom AOM scan of a sample without a fluorescent region of interest.**

### 4.3 Results and Discussion

#### 4.31 Ultrasound Pressure vs. AOM Signal

The first experiment performed with the designed system was the recreation of the Kobayashi experiments testing the relationship between ultrasound focal zone pressure and intensity of ultrasound modulated fluorescent signal. As can be seen in figure 4 - 11, the intensity of the relative AOM increases with ultrasound pressure squared. These results correspond to those

reported by both Kobayashi et al. and Yuan et al. [56, 61]. Of particular note, the experimental data became non-linear after the 43 kPa measurement and thus it was decided to maintain the maximum ultrasound pressure below this value to preserve the ultrasound transducer. The ultrasound focal zone pressure most often used was ~40 kPa which corresponds to a 60 $V_{p-p}$ driving voltage across the transducer. Both the 40 kPa ultrasound pressure and 60 $V_{p-p}$ driving voltage coincided with the studies reported by Kobayashi et al. and Yuan et al. [56, 57, 61] With lock-in detection, it was shown that minimum detectable fluorescent signal of our system was 6.18 nM. This translates to a fluorescence voltage output from the PMT of 384.5 pV and coupled with the responsivity value of 78 mA/W, the system detection capability is calculated as 98.6 pW. Based on these findings we continued our interrogation of the Kobayashi et al. experimental results.

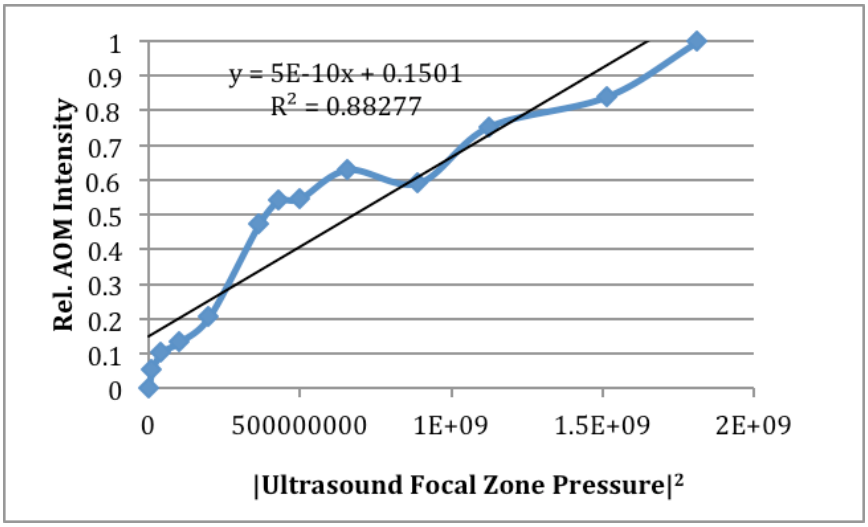


**Figure 4 - 11 AOM and the effect of increasing ultrasound focal zone pressure**

### 4.32 Tissue Phantom Experiments

Many attempts were made at repeating the experimental results of Kobayashi et al. in a turbid media tissue phantom. The results showed that AOM is created when the ultrasound focal zone was located outside of the intralipid and centered over the excitation source (lower right quadrant of the image). There is no AOM observable when the ultrasound focal zone is located within the intralipid area of the phantom. This would suggest that the AOM signal created by the

modulation of excitation is the dominant mechanism of acousto-optic interaction. The results showed that in an optical scattering tissue phantom the interpretation of the results reported by Kobayashi are unclear.

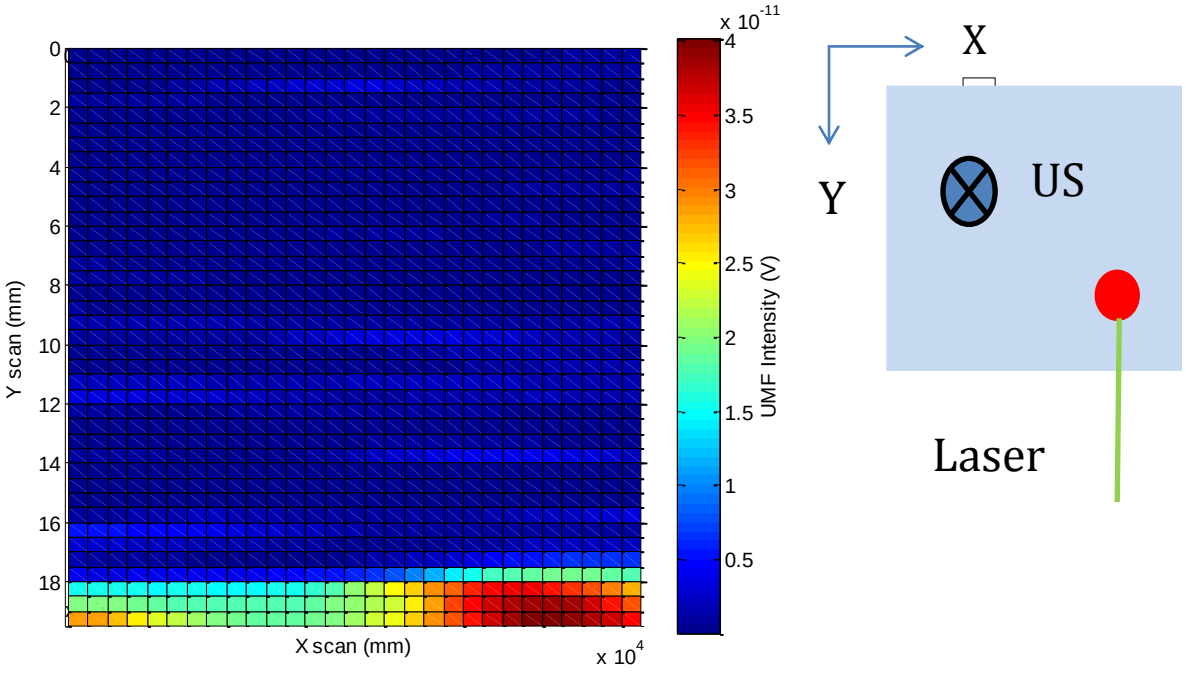


**Figure 4 - 12 (left) AOM recorded in an Intralipid Tissue Phantom (right) Experimental set-up**

Figure 4 – 12 represents an example of the experimental data we recorded using the system configuration in figure 4 - 9 to test the ability to record modulated fluorescent signal within a optically clear tissue phantom. In figure 4 – 13 (a), the arrow displays the direction of laser excitation which was centered incident to the fluorescent region of interest. The ultrasound was directed perpendicular to the laser direction (into the XY plane) and scanned in the XY plane allowing the creation of a map of measured AOM values in a 20x60 mm region. Based on the experimental results reported by Kobayashi et al., our results should be able to locate a region of fluorescent interest in the center of the scan plan as seen in figure 4 - 13 (b) [56]. However using nearly an identical experimental set-up the results were contradictory to those of Kobayashi et al.

As seen in figure 4 – 13 (a), the peak AOM signal was recorded at the ultrasound position where the most excitation light was available and not at the center of the fluorophore. These results suggest that the dominant signal is ultrasound modulated fluorescence (560 nm) generated from fluorophore interaction with ultrasound modulated excitation light. This is not to be confused with direct detection of ultrasound modulated excitation light that occurs at the wavelength of the laser source (532 nm) and is filtered out of the signal and subsequent ultrasound modulated fluorescent signal before reaching the PMT detector. Unlike the modulation of incoherent fluorescent light as reported by Kobayashi et al., ultrasound modulation of a coherent light source and the subsequent modulation of a fluorophore's output is a phenomenon that has been previously reported in great detail [15, 25, 26, 77, 87, 88, 97]. Until the Kobayashi experiments, modulation of incoherent light was considered too weak to measure experimentally and has been met with questioning by other groups [15, 58-62, 78, 85, 86]. Upon further inspection, the results we measured mimic the anticipated result of the measured AOM signal in regards to the experiments performed and these results do not coincide with those reported by Kobayashi et al.

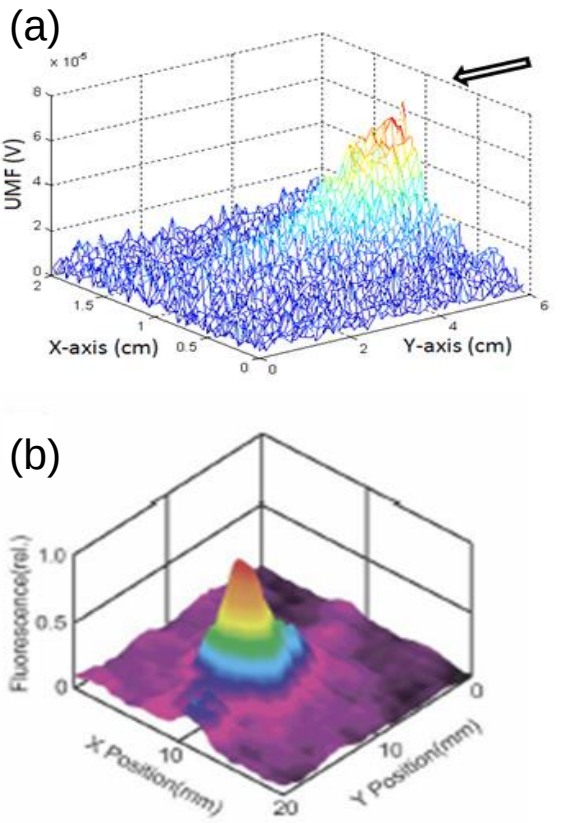


**Figure 4 - 13 Comparison of observed results with Kobayashi et al results (a) Experimental results of 2-D scan of AOM in a tissue phantom with the arrow representing the laser (b) Kobayashi et al results for a 2-D scan of AOM in a tissue phantom**

Modulated fluorescence signal reaching the detector has an optical wavelength of the fluorophore emission and varies at the sound frequency and there is no way of distinguishing separate contributions that may make up that signal. That is, modulated fluorescence created

by modulating the coherent excitation light and modulated fluorescence caused by modulating the emitted incoherent light are indistinguishable. Both signals will be modulated at the ultrasonic frequency and be received by the PMT as a light signal with the wavelength of the fluorophore emission. It is clear however from our data that the former dominates the signals we recorded.

### 4.33 Laser Modulation Experiments

The greatest contributing factor to the creation of modulated fluorescent signal is the modulation of the excitation source, and the subsequent modulation of the fluorophore excitation. Due to the relationship between excitation intensity and fluorescence emission intensity, the anticipated ultrasound modulated fluorescence should be proportional to the power of the laser excitation source at the point of the ultrasonic interaction within the sample. The laser excitation reduces in power as it is absorbed through the sample before reaching the fluorescent region of interest. This can be seen in figure 4 – 14 (a). Thus it is expected that as the ultrasound focal zone travels along the laser excitation axis (the Y axis in our experimental set-up) towards the fluorescent region of interest, the potential for modulating fluorescence decreases in proportion to the decreasing laser power. Figure 4 – 14 (b) is a Y axis profile representative of the data in figure 4 – 14 (a). It is clearly seen that the measured AOM as the ultrasound transducer travels along the y axis is indeed proportional to the expected laser power as excitation light travels through the sample. This is contradictory to the findings of Kobayashi et al. which appear to show that the only modulated signal recorded was from the modulation of the incoherent emission light from the fluorophore. Based on our findings, if the modulation of incoherent light does occur it is too weak to be distinguished under the experimental set-up that is reported by Kobayashi et al. However, their findings showing the ability to locate the fluorescent region along the X axis was confirmed by our data. However, the utility in this research is the ability to

locate fluorescence modulation at depth and thus only the Y axis modulation contributes to depth localization.

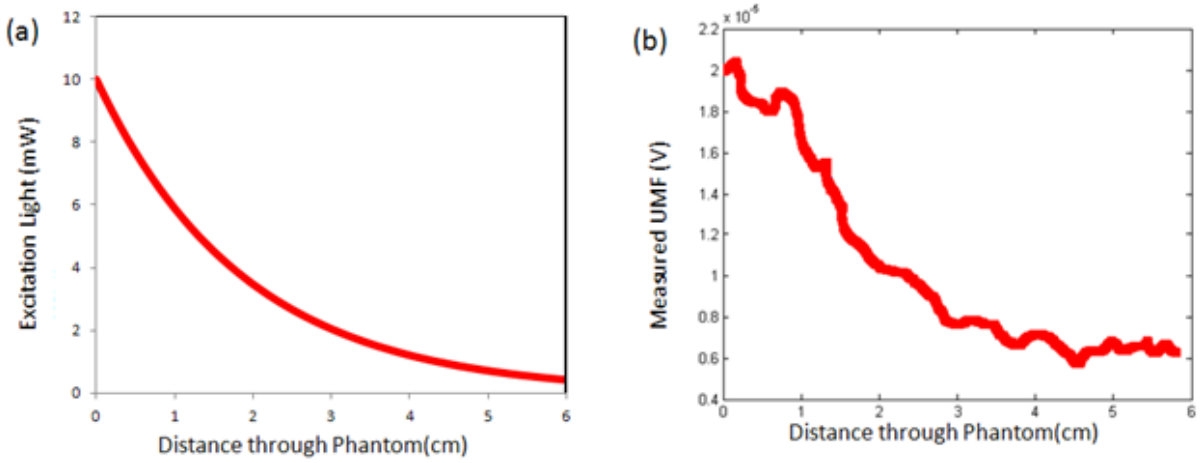


**Figure 4 - 14 (a) Predicted excitation light versus traveled distance through a phantom (b) AOM data displaying proportionality of AOM to predicted excitation light**

### 4.4 Conclusions

Kobayashi et al. reported the ability to measure ultrasound modulated fluorescence only when ultrasound interacted with the fluorescent region of interest. Not only were they able to distinguish this signal in the presence of AOM caused by modulation of the excitation source, but they were able to observe the reported signal with great modulation efficiency within a dense scattering medium without using enhanced detection techniques. Based on our results and the results reported by several other groups [58, 61, 78, 86], the modulation mechanisms contributing to the signal reported by Kobayashi et al. are unclear and the ability to record these interactions remain unrepeatable. The findings we report describe an ultrasound modulated fluorescent signal that is dominated by the modulated fluorescence caused when the ultrasound modulates the excitation light. Short of designing a more elaborate detection technique that can separate the modulated fluorescent signal into its parts, the results we report are more in line with expectations given the experimental design reported by Kobayashi et al. It is not

understood if the interaction between ultrasound and incoherent light is strong enough to be detected under the experimental set-up reported. If this interaction does indeed occur, further work needs to be performed to improve the modulation efficiency such that this weak signal can be distinguished from any modulated fluorescent signal that is created by the modulation of the excitation light source. In the next chapter, we will discuss our attempts at simplifying the incoherent light source in an attempt to elucidate the mechanism of modulation reported by Kobayashi. It was our hypothesis that by removing the excitation source and using an incoherent LED source as the ROI we should be able to detect AO modulated incoherent light.

# Chapter 5

## Detection of a Novel Mechanism of Acousto-Optic Modulation of Incoherent Light

### 5.1 Introduction

In this chapter, we report novel experimental observations of the modulation of an incoherent light beam by an ultrasonic field that are distinct from previous reported interactions of sound and light, and which demonstrate the ability to directly observe sound pressure patterns as changes in light absorption. This work was originally motivated by our interest in developing and evaluating a novel type of hybrid imaging system for molecular imaging in biological samples, and in the interpretation of previous reports of acousto-optical imaging using fluorescent light sources. Optoacoustic/Photoacoustic imaging, in which sound is produced and detected after light interacts with a target, has been successfully developed as a hybrid imaging method that combines the molecular sensitivity of optical methods with the spatial resolution and depth penetration of ultrasound, and is now in practical use in clinical and pre-clinical applications [98-100]. Acousto-optical imaging is an alternative technology to photoacoustic imaging, in which sound is used to modulate a light source, but it potentially shares some of the advantages of photoacoustic imaging, and our studies were motivated by the need to better understand the nature of acousto-optic interactions. The ability of sound to modulate light by some means is well established, and has been extensively studied both theoretically and experimentally for many years. However, previous reports of effects of sound on light have described mainly diffraction phenomena caused by phase differences of light waves induced by sound fields, such as those by Brillouin [65], Raman and Nath [101-105], Debye and Sears [106], Bragg [107], Lucas and Biquard [108], Berry [109], and Wang [73, 110]. To our knowledge, there have been no previous reports of the direct effects of sound causing changes in the absorption of ballistic photons, as reported here.

Acousto-optical imaging was first studied in the early 1990s when Marks et al. experimented with the ability to "tag" light with ultrasound [23]. Wang used a related approach to acquire images of tissues phantoms, while Leutz and Maret theoretically and experimentally analyzed the ultrasonic modulation of light [25, 87]. To date, most reports of Acousto-Optical imaging have exploited the ultrasonic modulation only of coherent light to interrogate the optical properties of a region of interest. However, in order to detect the effects of ultrasound on the emissions from fluorescent sources within an optically turbid medium, it is necessary to be able to measure ultrasonic modulation of incoherent light. To date there have been only a small number of groups that have detected and reported the ultrasonic modulation of incoherent fluorescent light [61, 78, 111-113]. Kobayashi et al. were the first to develop an acousto-optical system to demonstrate the ability to ultrasonically modulate the fluorescent light and also image the distribution of embedded fluorophores tomographically [111, 112]. The mechanism behind their reported results is not well understood and to date, no other group has been successful in repeating their experiments using similar apparatus. In our own studies using a near-identical set up, we were unable to replicate the precise effects reported by Kobayashi et al., though we did observe robust modulation of the coherent light used to produce fluorescence and the consequent modulation of the emission from the fluorophores. This phenomenon has previously been termed the ultrasound tagging of photons [25, 75, 87, 97, 114] and is exploited in the techniques of ultrasound-modulated optical tomography (USMOT) also known as acousto-optical tomography (AOT) [115]. As a follow up to those studies we aimed to test whether acoustic modulation of incoherent light was detectable using reasonable sound intensities. To remove possible confounding effects of the modulation of any coherent light sources, instead of using a laser to excite a fluorophore we substituted an incoherent LED light source. This was similar to the experimental methods of Huyhn et al. in which a chemiluminescent source replaced the laser excited fluorophore [113]. The LED was used because it was easily controlled and characterized. Using this experimental setup, we were able to demonstrate and

quantify the effects of ultrasound modulation on incoherent light, and here we report experimental evidence that the ultrasound focal zone produces a spatial variation of light absorption which, when projected, replicates the expected distribution of sound pressure and material density in the sound field. This effect differs from previous reports of diffraction phenomena caused by phase differences such as those mentioned above, and allows a much simpler approach to the observation of sound fields than those provided by previous work [116-119].

### 5.2 Materials and Methods

Figure 5 -1 shows the experimental system that was designed and built to be able to measure both optical and acousto-optical signals. A water tank was constructed with an opening for a transmitting ultrasound transducer (directed along the x-axis) and an orthogonal optical window (directed along the y-axis) centered at approximately 38.1 mm distance along the transducer (x) axis, and offset by 103 mm (along y). A waterproof LED light source (Super Bright LEDs, RL5-R8030, 630 nm) was attached to a three-dimensional translation stage and inserted into the water tank. The LED was positioned 10 mm along the y-axis from the ultrasound beam axis and directed towards the optical window. A focused circular ultrasound transducer (Olympus Panametrics V314, 1 MHz center frequency, 19.05 mm element size and 38.1 mm focal length, or a Valpey Fischer, IL0206HP, 2.25 MHz center frequency, 19.05 mm element size and 50.8 mm focal length) was placed such that the axial propagation of the ultrasonic beam (along x) was perpendicular to the principal direction (along y) of the LED light. The ultrasound focus of the 1 MHz transducer was located directly in front of the center of the optical window. A function generator (Agilent Technologies, 33500B) supplied a continuous wave, 1 MHz sinusoidal signal to an RF amplifier (Amplifier Research, 200L) to drive the ultrasound transducer at a selected voltage (0-60 volts peak to peak) to achieve a corresponding ultrasound focal zone peak negative pressure of 0-60 kPa. The voltage to

pressure conversion was calibrated and verified using a hydrophone (Onda HNC-0200). A photomultiplier tube (PMT)(Hamamatsu, H5783-20) and long, narrow sampling slit (0.75 mm width) were mounted to a translation stage at the optical window. The slit was positioned so that the light signal reaching the PMT was integrated vertically across the slit at the center of the PMT surface. The translation stages allowed the two dimensional movement of the PMT and slit to scan the pattern of LED light directed towards the PMT. The PMT signal was then passed through a trans-impedance amplifier (Hamamatsu, C6438) and amplified 20 dB and then input into a lock-in amplifier (Stanford Research Systems, SR844). The signal entering the lock-in amplifier was amplified a further 20 dB. The lock-in amplifier measured only the modulated light signal from the PMT that matches the frequency of the reference signal, which was the same as the ultrasound frequency. To record the entire incident light signal (modulated and unmodulated) reaching the PMT for a reference level, the output from the PMT could bypass the lock-in amplifier and be recorded directly on a recording oscilloscope (Hewlett Packard, 54503A). Both the lock-in amplifier and oscilloscope measured the signal amplitude (v) of the modulated input signal received from the PMT. However, we report all findings as the intensity of the modulated input signal ($v^2$) or the squared signal amplitude. A computer with LabVIEW software was used to control all stage movements and data acquisition from the lock-in amplifier and/or the oscilloscope.

When the ultrasound transducer was excited, the PMT recorded an acousto-optic signal indicating there was a direct modulation of the light reaching the PMT at the transducer frequency. We first moved the PMT and slit in the x-direction (perpendicular to the principal direction of light propagation) to locate the position of the peak acousto-optical signal in an optically clear sample (water), and this was then recorded as a function of the ultrasound transducer voltage, which produced variations in the applied ultrasound peak pressure in the focal zone. The incident unmodulated light signal produced by the LED was also measured. The modulation depth*, M,* was then calculated at each ultrasound pressure using:

$$M = \frac{\text{modulated light}}{\text{total incident light}} \tag{5-1}$$

Next, we compared the acousto-optical modulated (AOM) signal after passing through an optically clear sample (water) and also within turbid media samples (0.125, 0.1825, and 0.25 % volume, whole milk) while varying the applied ultrasound frequency (0.62, 1.0, 1.3, and 2.25 MHz) at a constant ultrasound pressure (~60 kPa). The turbid media samples were not intended to be of physiological relevance as reduced scattering coefficients of dilute whole milk samples are expected in the $mm^{-1}$ range [120, 121] while reduced scattering coefficients of biological tissues are expected in the $cm^{-1}$ range [122, 123], but they were included to help isolate the mechanism of interaction. Two separate US transducers were used to achieve the desired frequencies, one with a center frequency of 1 MHz and the second with a center frequency of 2.25 MHz. Although the first ultrasound transducer was resonant at 1MHz, the effect of the ultrasound on the LED light was measured by driving the transducer at 0.62, 1.0, and 1.3 MHz. At 0.62 and 1.3 MHz the transducer conversion efficiency was reduced by 50%, so we increased the driving voltage to compensate and verified the same peak pressure was achieved using the hydrophone. The spatial patterns of the AOM signals were measured by scanning the PMT and slit in 1 mm steps along the x-axis for each frequency at a fixed offset along y.

The overall geometry was also varied by adjusting the distance of the LED to the ultrasound focal zone between 10 and 16 mm respectively in 2mm increments, and by varying the distance from the focal zone to the scanning slit from 103 to 130 mm. At each step in x, 100 data points were recorded and averaged. The spatial variation of the LED light reaching the PMT without any ultrasonic modulation was also measured.

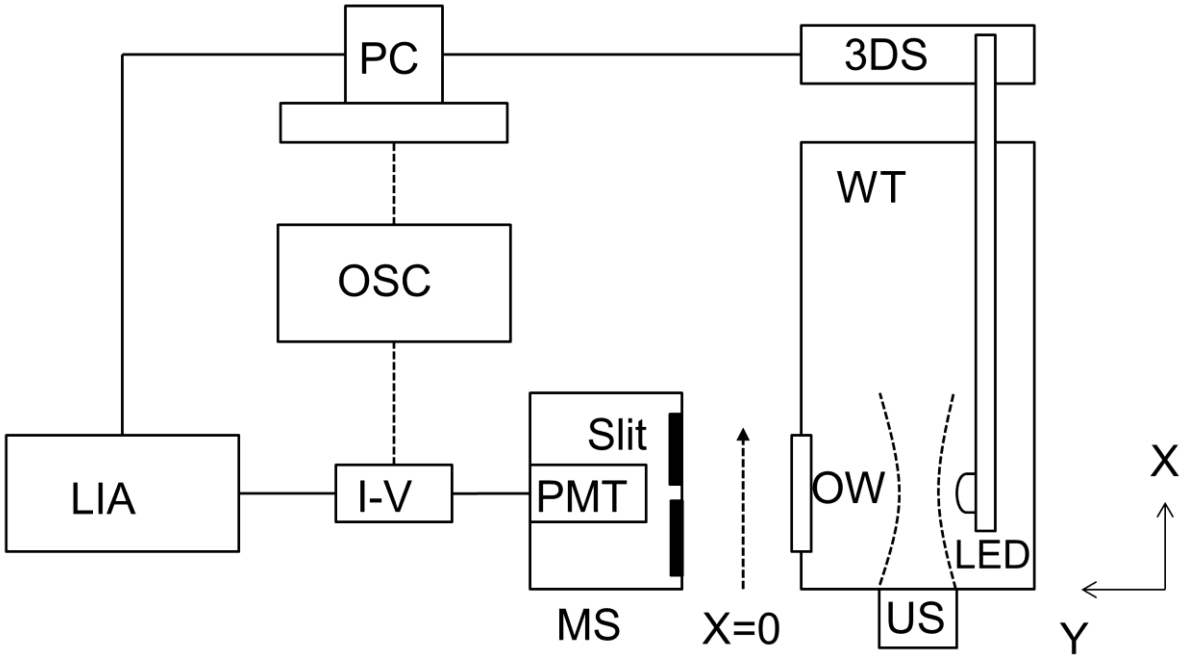


**Figure 5 - 1 Experimental Apparatus. US: ultrasound transducer; LED: light-emitting diode; OW: optical window; WT: water tank; PMT: photomultiplier tube; MS: motion stage; I-V: transimpedance amplifier; LIA: lock-in amplifier; OSC: oscilloscope; 3DS: three axis motion stage; PC: LabVIEW system control and data acquisition computer**

### 5.3 Results

Figure 5 - 2 (top) shows the effect of the ultrasound pressure on the modulated light signal in water as measured by the lock-in amplifier. The AOM signal intensity was linearly proportional to the squared ultrasound pressure ($R^2$ = 0.997). Figure 5 - 2 (bottom) shows that the modulation depth, M, was also linearly proportional to the squared ultrasound pressure ($R^2$ = 0.997) with a peak modulation depth of ~$1x10^{-8}$ at an ultrasound pressure of ~60kPa.

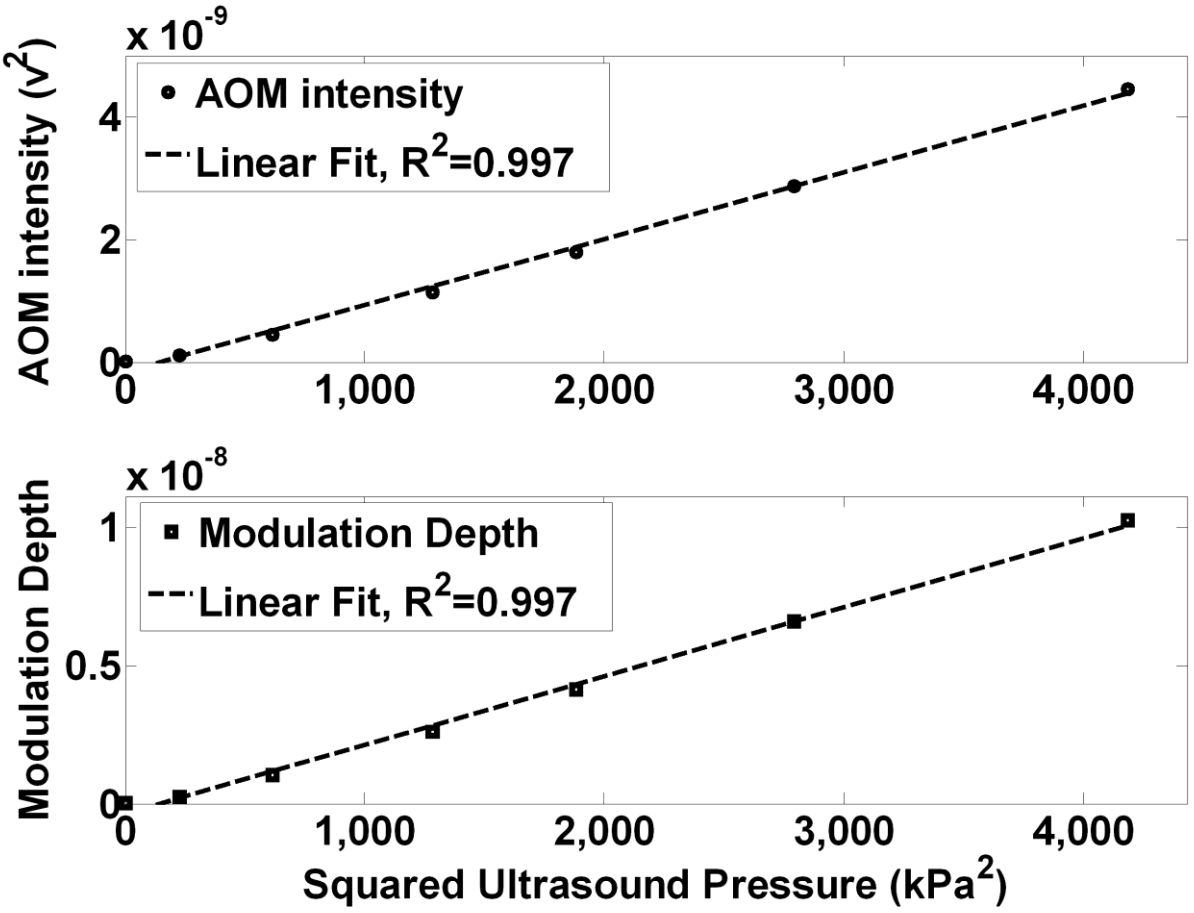


**Figure 5 - 2 Acousto-optic modulation (AOM) intensity and modulation depth increase linearly with squared ultrasound pressure. For incoherent light traveling through an ultrasound focal zone, the AOM intensity (top) and modulation depth (bottom) are linearly proportional to the squared ultrasound pressure within the focal zone.**

Figure 5 - 3 (top) shows the light distribution incident on the detector after passage through an optically clear medium (water) without ultrasound modulation, measured by scanning the PMT and slit with the LED to focal zone distance (d) = 10 mm and the LED to PMT projection distance (D) = 113 mm. The light pattern peaks about the principal axis of the LED at the center of the optical window, is reasonably uniform over approximately 30 mm of travel, but it then decreases monotonically as the slit moves further from the center of the LED and optical window. The limited size of the optical window and the geometry of the LED reduce the extent of the projection of the light at the plane of the detector. Figure 5 - 3 (bottom) shows the corresponding AOM signal pattern when the ultrasound is on. The overall pattern extends over approximately the same extent but there is a main narrow central peak with adjacent smaller maxima or side lobes on either side. The smaller maxima are located an average 8.5 mm from the main central peak. This pattern at first is suggestive of a far-field diffraction pattern, but as shown below, the pattern is in reality a simple projection of the variation of absorption of the light as it passes through the focal zone.

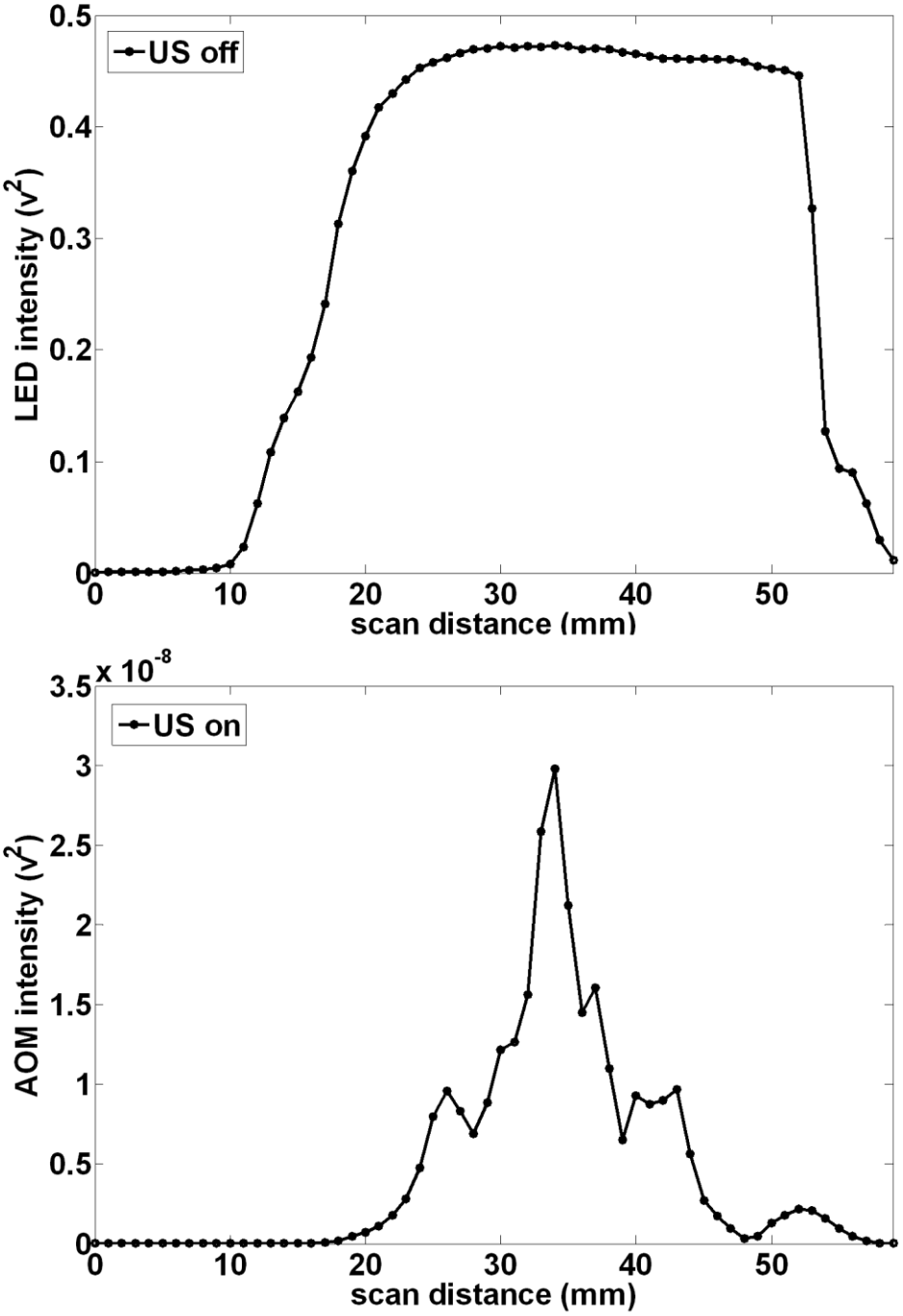


**Figure 5 - 3 Ultrasound modulation causes a spatial pattern in the projection of incoherent LED light in water. When the unmodulated LED light propagation (RF off) is sampled at a projected distance of 113 mm, the normalized incoherent light distribution is relatively smooth and uniform over the detection window. However when the light passes through an ultrasound focal zone (1 MHz, located 10 mm from the LED and 103 mm from the projection plane), the light displays a pattern having a central peak with smaller maxima or side lobes on either side with an average peak spacing of 8.5 mm.**

Figure 5 - 4 shows the corresponding projection of the 1 MHz, acousto-optically modulated light after passage through a turbid media containing varying volume percentages of whole milk. Each projection displays a similar pattern with a main central peak and adjacent smaller maxima or side lobes. Increasing milk concentration decreases the peak AOM intensity, but the peaks in milk appear more clearly resolved as the minima are deeper. The average distance between peaks was measured to be approximately the same.

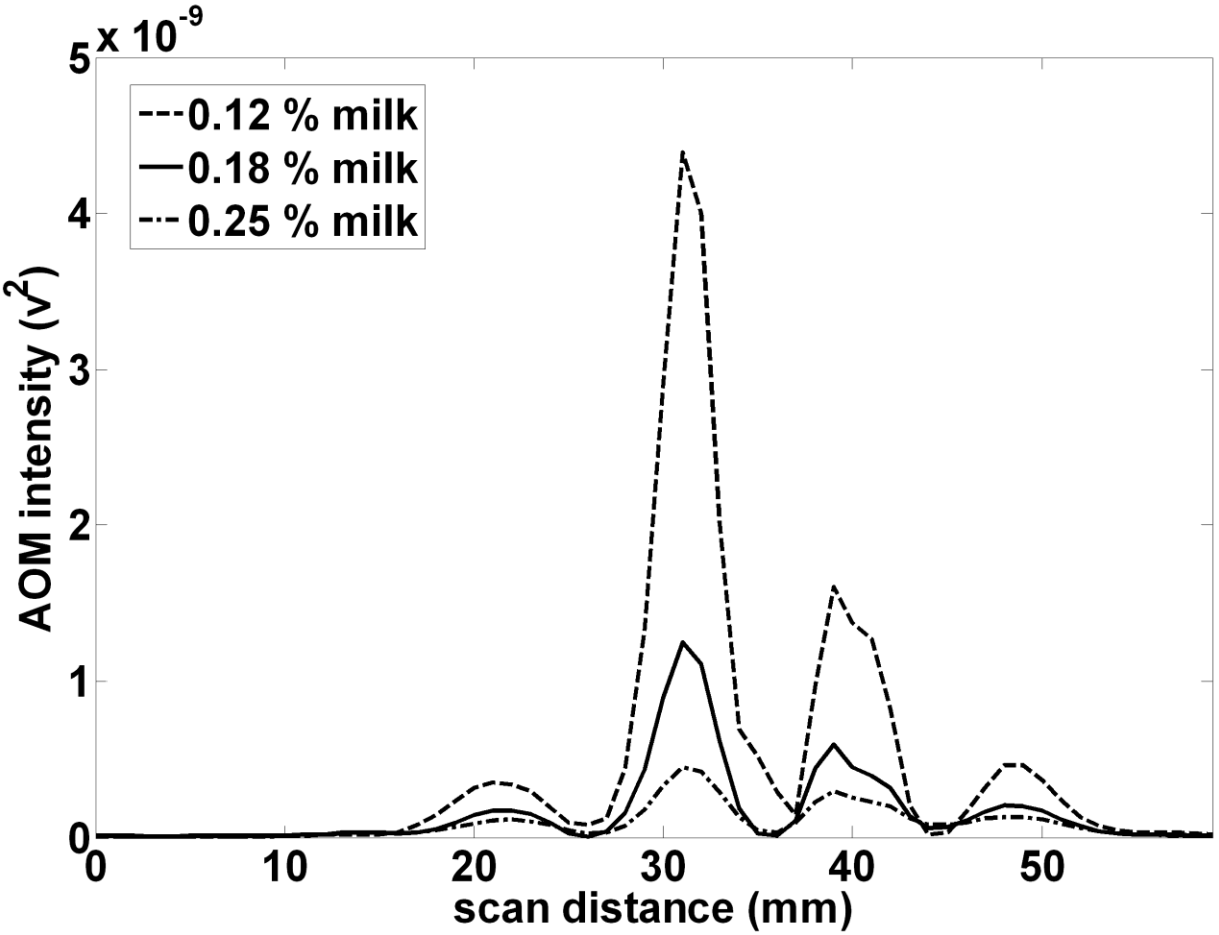


**Figure 5 - 4 Ultrasound modulation causes a spatial pattern in the projection of incoherent LED light in milk. Passing LED light through a continuous wave ultrasound focal zone (1 MHz, located 10 mm from the LED and 103 mm from the projection plane) causes acoustic modulation of the light. In a turbid medium consisting of a suspension of milk, the projection of the LED light at 113 mm consists of a peak located at the center of the optical window and adjacent smaller maxima or side lobes. With increasing milk concentration, the spatial pattern does not change but the AOM signal decreases and the lobes appear better resolved.**

Figure 5 - 5 shows the measured projections (for 1 MHz AOM light, within 0.25 % volume, whole milk) for various distances (10, 12, 14, and 16 mm) between the LED source and the ultrasound focal zone, with a fixed ultrasound focal zone to PMT distance of 103 mm. As the LED was positioned further away from the focal zone, the peaks in the distant projections undergo shifts that decrease the distance between them, and additional peaks become more clear at the edge of the window. The average distance between peaks decreased as the LED to US focal zone increased (separations of 8.67, 8, 7.5, and 7.33 mm for 10, 12, 14, and 16 mm respectively), consistent with a change in the geometrical magnification of the focal zone by the light source.

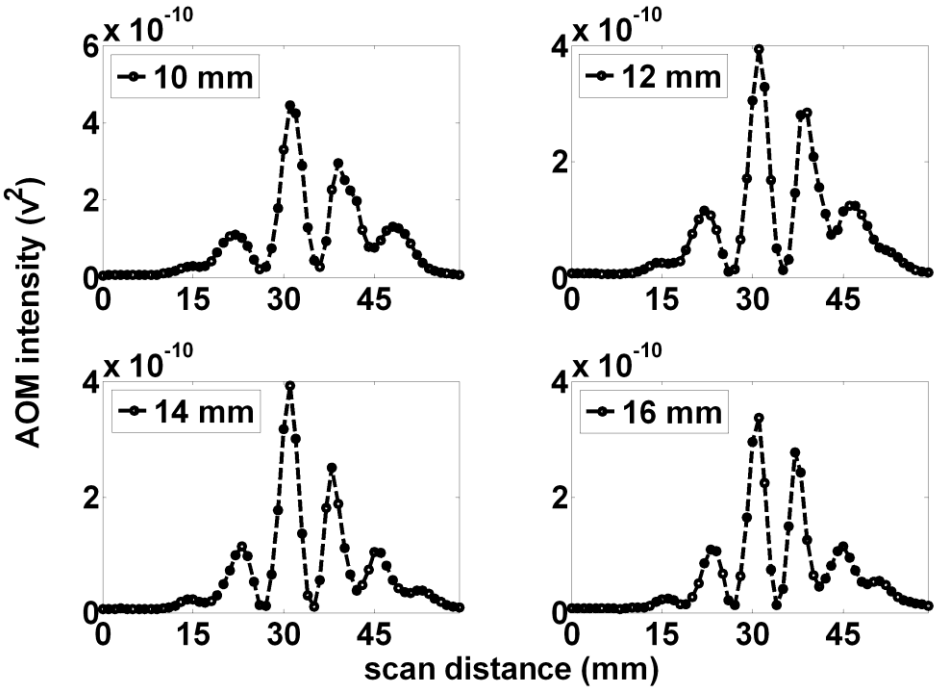


**Figure 5 - 5 The spatial pattern is suggestive of the alternating regions of optical absorption caused by ultrasound. Increasing the distance between the LED and the ultrasound focal zone causes a narrowing of the overall pattern as well as reduction of the average peak to peak distance. At a projection distance of 113 mm and LED to ultrasound focal zone distance of 10 mm (A), the distant pattern displays alternating peaks with an average peak to peak distance of 8.67 mm. This can be used to calculate an expected 0.77 mm average width of the alternating regions within the ultrasound focal zone. This is precisely the expected value of a half-wavelength of sound in water. As the LED was positioned further from the ultrasound focal zone, (B), (C), and (D), the observed pattern narrowed with additional peaks being added on the fringes of the pattern. In addition, the individual peaks narrow. The pattern is suggestive of the alternating region of optical absorption caused by the ultrasound.**

Figure 5 - 6 shows the measured projections (for 1 MHz AOM light, within 0.25 % volume, whole milk) for various distances (10, 12, 14, and 16 mm) between the LED source and the ultrasound focal zone but with an increased distance between the ultrasound focal zone and PMT of 130 mm. Similar to the above, the distant projections display small shifts decreasing the distance between the peaks, which also become narrower, with increasing LED to ultrasound focal zone distance (average distance between peaks was 10.5, 10.25, 10, and 8.75 mm for the LED to US focal zone distances of 10, 12, 14, and 16 mm respectively).

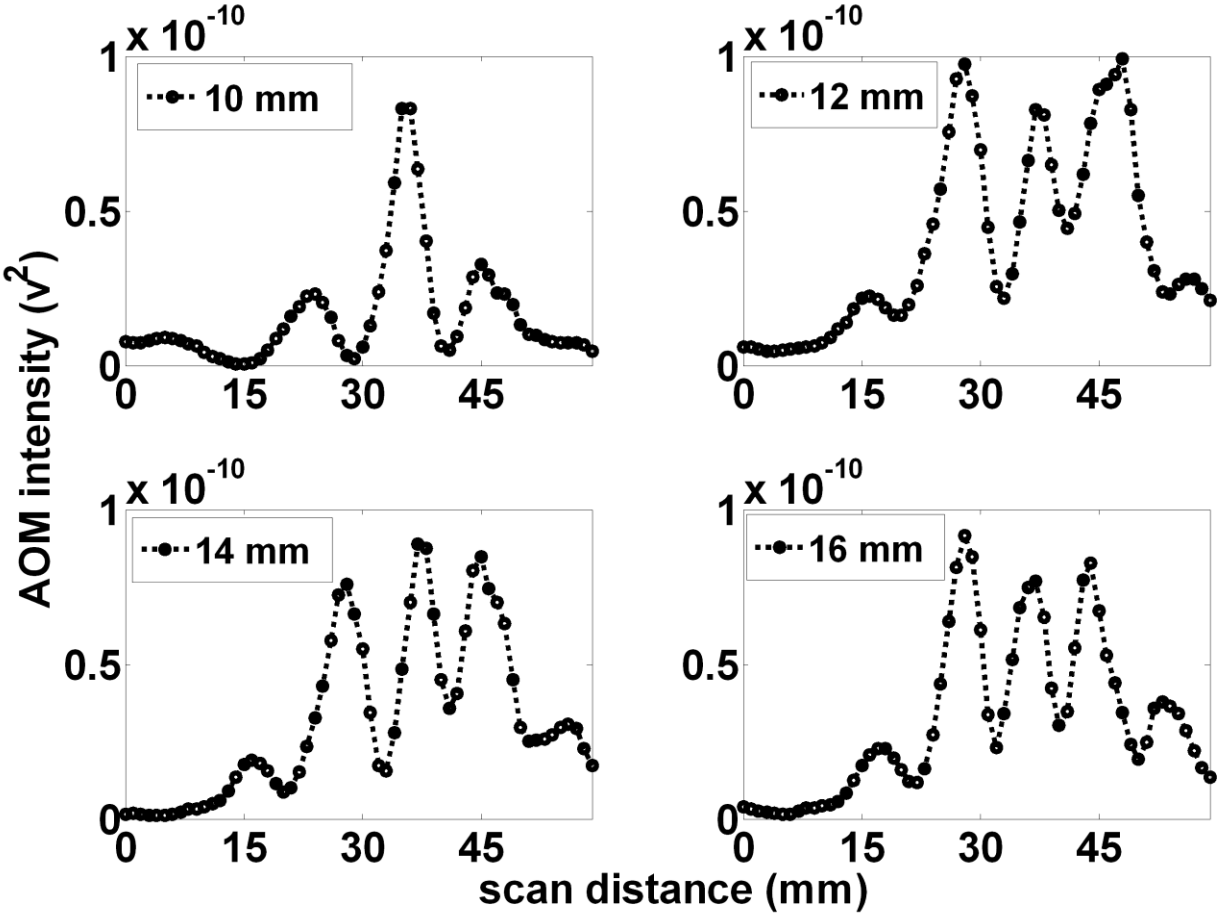


**Figure 5 - 6 The spatial pattern scales with increased projection magnification. When the projection distance = 140 mm and LED to ultrasound focal zone distance = 10 mm (A), the distant pattern displays alternating peaks with an average peak to peak distance of 10.5 mm. This can be used to calculate an expected 0.75 mm average width of the alternating regions within the ultrasound focal zone. This suggests the pattern scales with expected projection magnification. Similar to figure 5, as the LED was positioned further from the ultrasound focal zone, (B), (C), and (D), the observed pattern narrowed with additional peaks being added on the fringes of the pattern. In addition, the individual peaks narrow.**

Figure 5 - 7 shows the measured projections (for 1MHz AOM light, within 0.25 % volume, whole milk) for four different ultrasound frequencies (0.62, 1.0, 1.3, and 2.25 MHz) corresponding to wavelengths of 2.4, 1.5, 1.15 and 0.67 mm respectively. The LED to focal zone distance was set at 10 mm and the focal zone to PMT projection distance was set at 130 mm. As the frequency increased, the peaks in the light pattern become closer and more peaks appear within the window. The number of observed peaks was 2, 3, 4, and 7 for US frequencies of 0.62, 1.0, 1.3, and 2.25 MHz respectively.

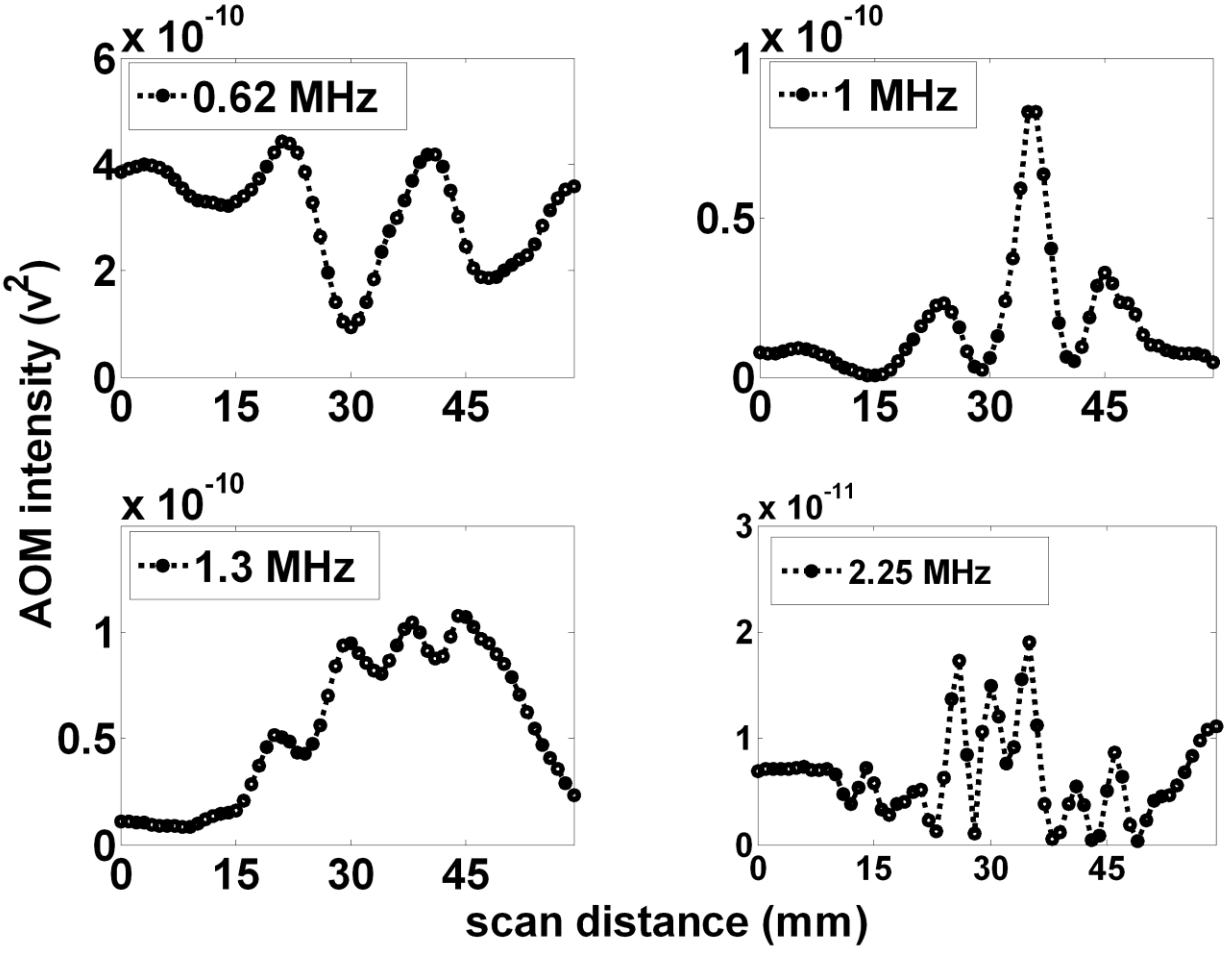


**Figure 5 - 7 . Increasing the applied ultrasound frequency increases the number of projected AOM peaks. The number of observed peaks and their separation within the observed pattern appears to scale with ultrasound frequency, (A), (B), (C), and (D), with 2, 3, 4, and 7 peaks observed for ultrasound frequencies of 0.62, 1.0, 1.3, and 2.25 MHz, respectively.**

## 5.4 Discussion

Our results demonstrate that ultrasonic modulation of incoherent light can be measured reliably, a phenomenon often suggested to be too small to observe [115]. Figure 5 - 2 shows modulation depths as large as ~$1x10^{-8}$ can be produced in pure water at readily achievable sound pressures. Furthermore, figures 5 - 3 through 5 - 7 show that incoherent light can be spatially modulated by sound to generate a pattern consisting of regular maxima and minima across the optical field of view. The pattern scales according to the wavelength and a magnification factor derived from simple geometrical considerations, but as shown below, does not conform to descriptions predicted by earlier theories that invoke wave diffraction and interference effects that are more usually associated with coherent light.

Mechanisms that may produce acoustic modulation of light have been extensively investigated before, and although there are clear explanations for some interactions with coherent light sources, the modulation of incoherent light is less well understood and more variable in practice according to several proposed theories [54, 55, 115, 124]. Resink [124] has recently reviewed the mechanisms by which photons may be “tagged” by ultrasound, and in experiments using coherent laser excitation and a fluorophore in place of the LED we have observed robust tagging of the laser light causing AO modulation at the ultrasound frequency, as predicted. However, in the current system, the light from the LED is expected to have a coherence length much less than 100 μm [125], and conventional theories of light tagging of such incoherent light do not readily translate to this situation. Moreover, the observed AOM signal pattern clearly arises from the passage of light through alternating regions of optical properties induced by the ultrasound and from our results in pure water (figure 5 - 3 bottom) does not depend on the presence of discrete scatterers or induced variations in their number density (which others have suggested may cause AOM signals) [78, 124, 126]. However as the observed pattern were more clearly resolved and quantified because of deeper minima in the turbid media milk experiments, the bulk of the data (figures 5 - 4 through 5 - 7) are reported as

the observations in a 0.25 % milk medium. It is known that the sound wave produces periodic variations in density of the medium, which also changes the refractive index of the material [23], including both the real (velocity) and imaginary (absorption) components. From simple acoustic theory, the fractional change in density is expected to be:

$$\rho_f = \frac{p_1}{\rho_0 c^2} \tag{5-2}$$

where $p_1$ is the ultrasound pressure (in Pa), $\rho_0$ is the medium density, and $c$ is the speed of sound in the medium [127]. At a pressure of 60 kPa the fractional change in the region of maximal compression is approximately 0.0027 %. The absorption coefficient of water at 630 nm is 0.319 $m^{-1}$ [128] so traversing a focal zone of dimension 3 mm would lead to variations in absorption (assuming absorption is proportional to density) producing a sinusoidal spatial modulation of the light of maximum amplitude ≈ 2.4 x $10^{-8}$ along the sound beam direction from absorption effects alone. The sound wave also likely produces changes in the light velocity, so some refraction changes may also arise that can cause phase shifts, but the relevance of these for incoherent light is not clear and given the above estimate they do not appear necessary to account for the patterns seen. This predicted spatial modulation of light amplitude is on the same order of magnitude as our observed modulation depth, seen in figure 5 - 2 as ~1x$10^{-8}$, and is easily observed with our experimental set-up. Furthermore, figure 5 - 2 shows the AOM signal and the modulation depth scale linearly with the squared ultrasound pressure, suggesting the observed affect is linearly proportional to the ultrasound intensity.

It was observed that the average distance between peaks scaled precisely with the expected geometrical magnification of a simple optical projection of the focal zone when changing the distances from the LED to the focal zone, from the focal zone to the measurement plane, and the wavelength. For simplicity, assume the LED acts as a point source of light. If the distance from the LED to the focal zone axis is d and the distance from the LED to the measurement plane is D then D/d is a geometrical magnification factor m. Distances along the

axis of the sound beam become magnified by m at the measurement distance. If the regions of alternating absorption along the axis of the focal zone of the sound beam have a width of a half wavelength $\frac{\Lambda}{2} = \frac{c}{2f}$ (where $\Lambda$ is the sound wavelength, $f$ the frequency, and $c$ the speed of sound, taken here to be ≈1500 m.sec$^{-1}$) these become $\frac{mc}{2f}$ in extent at the light detector. Note that, because we measure the temporally modulated light signal (rather than the mean ambient light level), regions of increased density along the axis show the same modulation as regions of decreased density or rarefaction, so the peaks in modulated light occur every half wavelength rather than every wavelength. As shown in figure 8, the regions of compression and rarefaction also have finite thickness $t$ in the direction of light propagation, and a sinusoidal variation along the sound field axis, so their projections are expected to have unsharp edges and may extend over a distance $\approx \frac{mc}{f}\frac{d}{2d-t}$. Thus we predict that alternating peaks of average width up to $\frac{mcl}{f(2d-t)} = \frac{cD}{f(2d-t)}$ separated by $\frac{mc}{2f}$, which may reduce the peak to trough modulation. Figure 9 shows the composite data from all the above experiments (varying $m$ and $f$), where we have plotted the measured peaks separations versus those predicted by simple theory. The measured separations of the peaks are accurately predicted, and linear regression gives the following relationship:

$$\text{measured peak spacing (mm)} = 1.03\frac{mc}{2f} + 0.6 \text{ with } R^2=0.93$$

Our data thus appear to suggest that the observed distant patterns are simple optical projections of the absorption pattern produced by the illuminated ultrasonic focal zone. These patterns scale appropriately with the ultrasound frequency and magnification factors. We thus propose that the light intensity propagating through the sound field region is modulated by the ultrasound because of variations in optical absorption alone, and that the distant light pattern

depicts the distribution of pressure within the ultrasonic focal zone. This is potentially a new way to image directly the sound fields from ultrasonic transducers.

We emphasize that our experimental findings cannot be explained by previous descriptions of acousto-optic effects. For example, Brillouin first suggested that ultrasound can modulate incident light acting as a sinusoidal grating which optically diffracts incident light into two critical angles [65]. However, Debye and Sears [106] as well as Lucas and Biquard [108] independently proved Brillouin's predictions inaccurate as they observed multiple orders of diffraction as opposed to the two critical angles Brillouin predicted. Both groups failed to adequately explain the appearance of multiple orders of diffraction but Debye and Sears did suggest that the lack of critical angles was due to the length of the ultrasound interaction with the light. They suggested that the Debye-Sears ratio given by:

$$Debye - Sears\ Ratio = \frac{\lambda L}{\Lambda^2} \tag{5-3}$$

where λ is the optical wavelength, Λ is the acoustic wavelength, and L is the interaction length; should be much larger than 1 for the appearance of the critical angles predicted by Brillouin. This ratio was later refined by Klein and Cook into the Klein-Cook parameter, Q [71], defined as:

$$Q = \frac{2\pi\lambda L}{\eta\Lambda^2} \tag{5-4}$$

where λ is the optical wavelength, L is the width of the sound beam, η is the index of refraction the medium, and Λ is the acoustic wavelength. When Q>>1, this is currently called the Bragg regime as Bragg was the first to witness this type of diffraction into critical angles using x-ray diffraction in crystals [107]. Despite unsuccessful attempts by Debye and Sears [106], Lucas and Biquard [108]. and Brillouin [129], Raman and Nath provided a series of papers [101-105] which explain the appearance of multiple orders with an exact derivation of the relationship between orders. The diffraction regime which causes multiple orders of diffraction is now known as the Raman-Nath regime.

In the Bragg regime, a diffraction pattern consisting of a zero order diffracted beam and a downshifted or upshifted first order diffracted side lobe should arise, while in the Raman-Nath regime a diffraction pattern with multiple diffraction orders projected symmetrically about the zero order is predicted [130]. We can dismiss Bragg diffraction as a possible explanation of our observed results because there are multiple peaks in the observed pattern and the experimental parameters do not meet the Klein-Cook condition [71] of Q»1. Given our set of experimental parameters (λ=630 nm, L=3 mm, Λ=1.5 mm@1 MHz), and assuming an index of refraction of water η=1.33 [131], the Klein-Cook parameter can be calculated to be $Q \approx 4 \times 10^{-9}$. Therefore Q«1 and meets the criteria for Raman-Nath diffraction. Within this regime, it is expected that the diffraction pattern will display multiple diffraction orders adjacent to the zero order at angles $\theta_m$:

$$\sin\theta_m = \frac{m\lambda}{\Lambda} \tag{5-5}$$

where m is the order of diffraction, λ is the wavelength of the light, and Λ is the wavelength of the acoustic source. Given our experimental values, the value of $\theta_1$ was calculated to be about 0.02°. Therefore under Raman-Nath theory, the diffraction pattern would generate a first order maximum located at:

$$m_1 = l \tan\theta_1 \tag{5-6}$$

where $m_1$ is the distance from the central maximum and l is the distance between the acoustic plane and the observation plane. For our experiment where l = 103 mm, this equates to an expected first order diffraction maximum located at 0.035 mm from the central peak whereas the experimentally observed first order peak location was located at an average 8.67 mm (figure 5-5, top left): when l = 130 mm the first order diffraction maximum would be expected at 0.045 mm whereas the observed maximum was located at an average 10.5 mm. These discrepancies are so large they cannot be accounted for by Raman-Nath or other diffraction theory.

## 5.5 Conclusion

We have reported the observation of acoustically modulated incoherent light within optically clear and turbid media which produces a spatial pattern that appears a simple projection of the variation of acoustic pressure within the focal zone of the sound field of an ultrasound transducer. The AOM signal and modulation depth are directly related to the sound intensity. The peaks in the projected light pattern correspond with the expected spacing of density variations and change with the geometrical magnification and wavelength of the sound field. We propose that the ultrasonic waves generate alternating regions of density that produce variations in absorption even in a clear medium such as water. Additional effects of changes in scattering number density or phase shifts and interference caused by variations in the real part of the refractive index do not appear to be necessary to explain these observations. In principle this type of coherent modulation of incoherent light could be used in novel imaging schemes, it may be relevant for the interpretation of some other studies, and may provide a novel way to image complex sound field directly.

# Chapter 6

## Direct Modulation of a Light Emitting Source

### 6.1 Introduction

The overall aim of acoustic-optical imaging is to develop a new form of hybrid imaging that combines the molecular sensitivity of optical probes with the depth penetration and spatial resolution of ultrasound but which avoids many of the issues and complexity of previous photoacoustic (PA) and acousto-optical (AO) techniques. All previous PA and AO imaging developments have relied on detecting secondary effects of optical emissions or indirect interactions, such as the sound waves generated concomitant with fluorescent light output, or the effects of sound modulating the light incident to a fluorophore, or the effects of sound modulating the refractive and scattering properties around a light emitting material. As a new approach, we investigated whether a direct, but heretofore ignored, effect of sound waves on the light output of fluorophores such as FRET pairs was detectable, postulating that ultrasound vibrations may actually modulate the light emission from an optical agent. The potential of directly affecting the light production process itself has been largely ignored, and we are unaware of any experimental studies to investigate this. We proposed to establish whether ultrasound can directly affect the light intensity and/or frequency produced by specific optical agents.

Although historically the direct effects of sound on light-emitting materials have been extensively reported, to date there have been few reported investigations of the direct modulation of the light produced by a fluorophore when subject to ultrasonic vibration. We hypothesized that ultrasound can be used to directly modify the light output of appropriate fluorophores such as FRET agents, and if so this could form the basis of a new type of hybrid molecular imaging device of the interacting fields. One previous approach to making acousto-

optical imaging of modulation of fluorescent emissions was achieved by creating contrast agents with quenchable fluorescent microbubbles [132] and ultrasound switchable fluorescent nanoparticles [133-135]. This chapter discusses our attempts at directly modulating the output of a light source via interaction with acoustic waves.

It is well known that ultrasound has both thermal and non-thermal effects on tissues [136]. It has been shown that when certain materials are illuminated with ultrasonic waves, light is emitted. This process is known as sonoluminescence and was first discovered in 1933 by Marinesco and Trillat when they noticed fogging of photographic plates in water when illuminated by ultrasound [137]. The fogging has been attributed to the emission of light from exploding bubbles of gas developed by cavitation due to the ultrasonic waves [138]. Development of these bubbles and further emission of light is outside the scope of this paper but readers are referred to Putterman and Weninger's review [139]. Furthermore it has been shown that ultrasound is capable of altering phosphorescence. In 1951, Lucien Petermann discovered that when a phosphorescent vinyl plastic was insonated with ultrasound, a radiation effect was present. Petermann along with Oncley showed that ultrasound can be detected due to excitation of phosphorescence using a CaS – SrS phosphorescent plate [140].

It is also known that ultrasound has both mechanical and thermal effects on media and thus it is possible that ultrasound could have an effect on the output of a fluorophore that is mechanically or temperature dependent. Green fluorescent protein (GFP) for example has been shown to undergo a quenching mechanism when the structure is compressed or stretched using atomic force microscopy [141, 142]. Based on prior studies, GFP is pressure insensitive up to 14kbar and thus compression of GFP is not likely to occur as a result of ultrasonic waves due to peak pressure of 60kPa at 1 MHz ultrasound frequency [143]. Yet another example of a contrast agent with an output that depends on their size is quantum dots. If the size of a quantum dot can be altered, the emission wavelength changes [144]. However like GFP, quantum dots are highly pressure insensitive and thus ultrasound pressures in the kPa range would be ineffective

at compressing the size of a quantum dot [145, 146]. Although GFP and quantum dots are not suitable for ultrasonic modulation, there is a wide range of contrast agents with the potential to be influenced by ultrasound. We tested a range of contrast agents to determine if fluorescent output can be modulated. Along with the conventional fluorescent dyes we tested at the beginning of this research in chapters 3 and 4, such as Rhodamine and Alexa dyes, we tested a variety of potential contrasts agents including ZnS, ZnCdS, a freely diffusing FRET pair based contrast agent, and FRET labeled nanosponges. Although this is not a complete list of contrast agents with the potential to be modulated by ultrasound, this chapter will describe our selection of these contrast agents as well as our results in attempting the direct modulation of their outputs.

## 6.2 Methods

### 6.21 FRET Modulation

In FRET (Förster Resonance Energy Transfer), energy is transferred from an excited donor to an acceptor molecule by intermolecular long range dipole-dipole interactions. This transfer can occur over distances of 10Å to 100Å. This allows FRET to be essentially a “spectroscopic ruler” as the distance it occurs over is very small [147]. In order to occur, the fluorescence spectrum of the donor and the absorbance spectrum of the acceptor must overlap. Thus a donor-acceptor pair must be chosen that meets not only the experimental constraints but also the constraints set forth by the physics of the FRET interaction.

At moderate powers ultrasound causes cyclic displacements of the medium of several nanometers and the positions of molecules by up to 50 Å. This could allow the switching on or off of FRET donor-acceptor pairs by increasing or decreasing the distance between the donor acceptor pairs. Nielsen et al. proposed a similar idea in which ultrasound is used to create a change in donor-acceptor distance of a FRET pair thus directly changing the FRET signal [148].

This theory hinges on the fact that FRET efficiency is directly proportional to the inverse sixth-distance between the donor and acceptor [149] as shown in:

$$E = \frac{1}{1+\left(\frac{R}{R_0}\right)^6} \tag{6-1}$$

where $E$ is the FRET efficiency, $R_0$ is the Förster radius, and $R$ is the donor-acceptor distance. Thus if the distance between the donor-acceptor pair can be modulated, the FRET signal will be altered.

In an initial experiment, we aimed to evaluate the ability to modulate a freely diffusing FRET pair using ultrasound. For these experiments, we chose a FRET pair consisting of Rhodamine B dye as the FRET pair donor and 4-Sulfonir as the FRET pair acceptor. 4-Sulfonir is a novel dye created at Vanderbilt by Dr. Wellington Pham [150]. This dye was chosen for its ideal characteristics which allow this research to probe the principles of modulation of FRET emissions both ex-vivo and in-vivo. It has a characteristic large Stokes shift of almost 150 nm with an excitation maximum at 600nm and an emission maximum at 750nm. The emission maximum being near-IR allows maximal depth penetration in tissue suitable for future studies involving *in-vivo* small animal imaging. In addition to the near-IR capabilities of this dye, it has been shown to be water soluble [150]. The developed dye has a monofunctional group suitable for activation as a succinimide ester. Besides this amine-reactive ester, Pham has successfully developed a versatile amino-epoxide linker and attached it to the 4-Sulfonir dye via the amine end of the linker. The epoxide-derivatized dye can be used to label a variety of bioactive materials including peptides, proteins, nanoparticles, and more, via not only amino groups, but also hydroxyls or thiol-containing bioactive materials [151]. Furthermore, the selected FRET donor dye was Rhodamine B. This dye was chosen because it is readily available and the 575 nm emission peak overlaps with the 600 nm excitation peak of the chosen 4-Sulfonir acceptor. This dye will allow the labeling of protein/antibodies. Rhodamine B is also water soluble and is

available with an NHS ester group which allows primary and secondary amino group labeling. The combination of the properties of the Rhodamine B donor and the 4-Sulfonir acceptor has the potential to allow us to maximize our abilities to modulate FRET emissions in both *ex-vivo* and *in-vivo* applications.

Using the experimental setup in figure 6 – 1, we attempted to observe modulation of product from the freely diffusing Rhodamine B and 4 – Sulfonir FRET pair. A 532 nm laser excitation source was incident on the sample vial containing the FRET pair. A pencil type ultrasound transducer (US) was immersed in the sample and cycled on and off. The modulated donor fluorescence was observed via the photomultiplier tube (PMT) by filtering out the laser excitation source and the acceptor emissions. The output signal from the PMT was directed to a lock-in amplifier (Stanford Research Systems, SR844) and the modulated donor fluorescent emission was recorded via a customized LabVIEW program described in the Appendix. An initial experiment alternated ultrasound on and off (1000 data points per block) and FRET donor emissions were observed.

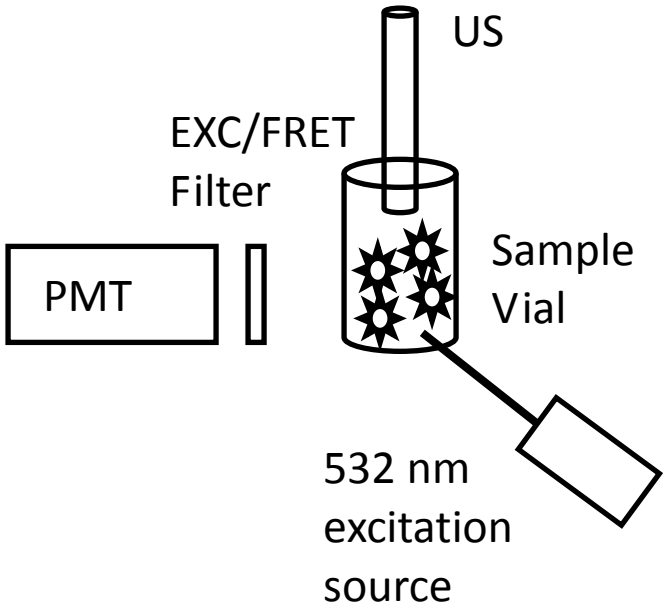


**Figure 6 - 1 Experimental setup for direct ultrasound modulation of contrast agents. PMT is the photomultiplier tube; EXC/FRET Filter is the chosen filter set to filter the excitation source and chosen FRET emission light; and US is the ultrasound transducer.**

### 6.22 FRET Labeled Nanosponges

In addition to the chosen freely diffusing FRET pair of Rhodamine B and 4-Sulfonir, we evaluated if the emissions of a FRET pair labeled nanosponge were capable of being modulated by ultrasound. This was done with the nanosponge concentration in a freely diffusing medium of dichloromethane (DCM). Nanosponges were chosen as an interesting potential contrast agent because of their potential and untested ability to be mechanically altered with ultrasound interaction. This was anticipated to be similar to the known interaction between ultrasound and microbubbles where ultrasound can create oscillations in the microbubble diameter [152]. It was our hypothesis that a nanosponge would allow a greater ultrasound influence on the FRET pair than expected in a freely diffusing solution of FRET pair as studied in the work described FRET modulation section above. The FRET labeled nanosponges were provided by Dr. Eva Harth at Vanderbilt University.

Harth et al. created a functionalized polyester nanoparticle (nanosponge) which allows the attachment of targeting agents and contrast agents for drug delivery and potentially for targeted contrast agent delivery for imaging [153]. Using these nanosponges, Harth was able to provide us with a FRET labeled nanosponge. The chosen FRET pair was Alexa Fluor 555 (donor) and 647 (acceptor) dyes. These dyes were chosen as succinimidyl esters (NHS esters) of Alexa Fluor dyes that are readily available. This allows the Alexa Fluor dyes to be conjugated to the primary amine ($R\text{-}NH_2$) groups available on the surface of the nanosponge. This is represented in figure 6 – 2. This attachment can be done using a statistical attachment of the Alexa Fluor dye FRET pair. This allows the ability to select the proportion of the two dyes on the surface of the nanosponge. This arrangement is represented in figure 6 – 2. This is important as we are attempting to vary the FRET efficiency via ultrasound modulation of the nanosponge diameter. Although the dyes will be randomly distributed on the surface of the nanosponge, the statistical attachment allows the possibility of FRET interactions. Using the experimental setup in figure 6 – 1, the FRET labeled nanosponges suspended in dichloromethane (DCM) were

modulated in an identical fashion as the freely diffusing FRET pair described previously. Blocks of signal with ultrasound on and off were observed and compared for FRET donor emissions and the chosen DCM control sample.

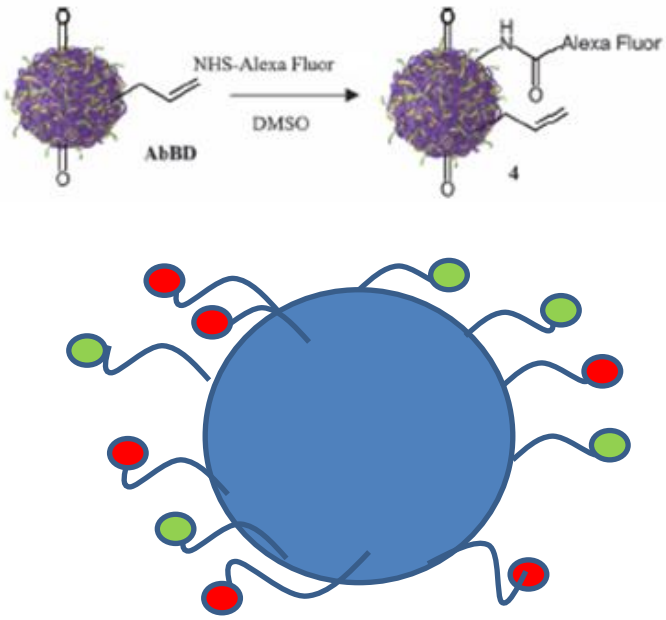


**Figure 6 - 2 (top) Labeling of polyester nanosponge with NHS-Alexa Fluor Dye. (bottom) Representation of the statistical attachment of Alexa Fluor dye FRET pair. Alternating colors represent the different Alexa dyes.**

### 6.23 ZnS and ZnCdS

Lastly, we attempted to modulate separate suspensions of ZnS and ZnCdS. These were chosen as they have been shown to interact with ultrasound [154, 155]. ZnS and granular mixtures of ZnS have been shown to sonoluminesce with ultrasound interaction [154, 155]. Addtionally, ZnCdS phosphorescent emissions have been shown to be varied with ultrasound interaction [156, 157]. This phenomenon was used in early ultrasound imaging techniques via the use of ZnCdS phosphorescent films [158]. Upon exposure to ultrasound, the phosphorescence of ZnCdS phosphor film varies and can be observed visually or through photographic detection. At the beginning of this work, neither ZnS nor ZnCdS had been studied as potential contrast

agents for acousto-optical imaging techniques and thus we aimed to study the ability to directly modulate the emissions of these substances.

Using the experimental setup in figure 6 – 1 (without the excitation source), we observed the interaction between ultrasound and ZnS or ZnCdS suspensions. As both compounds are insoluble, it was necessary to suspend each compound separately within a dimethyl sulfoxide (DMSO) solvent and the suspension was continually stirred by inserting a magnetic stir bar and placing the sample vial on a stirring plate. In an initial experiment, light emissions from each suspension, as well as a control sample of DMSO, were observed while alternating the ultrasound on and off for blocks of 1000 data points. Next, this was repeated in four alternating blocks of ultrasound on and off while collecting 5000 data points per block.

### 6.3 Results and Discussion

In this section will describe our experimental observations for our attempts at the direct modulation of freely diffusing FRET, FRET labeled nanosponges, and suspensions of ZnS and ZnCdS.

#### 6.31 FRET Modulation

Initial experiments showed that direct modulation of freely diffusing FRET pairs was not observed with the chosen experimental methods. Figure 6 – 3 shows the raw data observed of Acousto-Optical Modulated freely diffusing FRET pairs (Rhodamine B and 4-Sulfonir). The series in blue represents the AOM observed for the freely diffusing FRET sample when the ultrasound transducer was off and the red series is the observed FRET AOM signal when the ultrasound transducer was on. From this comparison there appears no significant observable difference between the two.

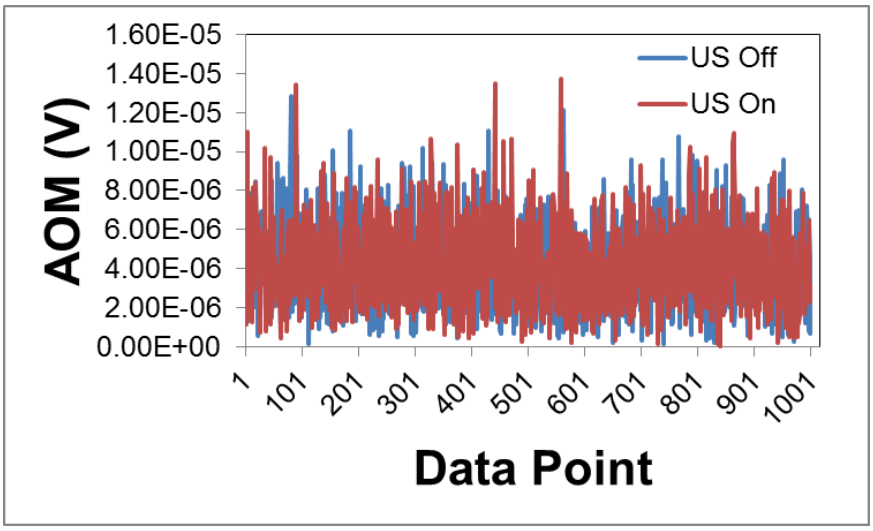


**Figure 6 - 3 Observed Acousto-Optical Modulation (AOM) of freely diffusing FRET pairs with ultrasound off and on.**

A statistical comparison was made between the two data sets. First, the mean and standard deviation for each set were calculated and can be seen in figure 6 – 4. The mean FRET AOM signals when the ultrasound was off and on were $4.15x10^{-6}V$ and $4.16x10^{-6}V$ respectively. The standard deviations were $\pm 2.17x10^{-6}V$ and $\pm 2.13x10^{-6}V$ respectively. The visual difference between the AOM signal with ultrasound off and on are negligible. A statistical t-test between the two data sets provide a p value of 0.27 and thus the means of the two samples are not statistically significantly different.

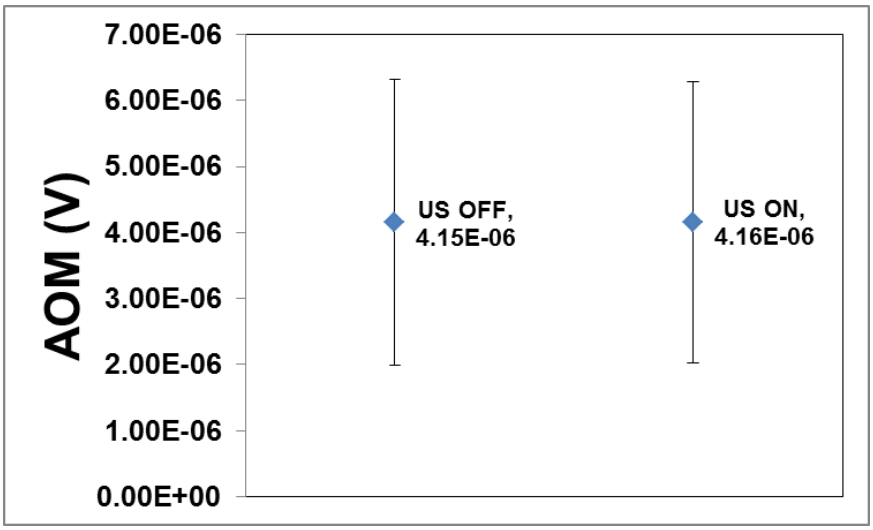


**Figure 6 - 4 Mean value of observed AOM of freely diffusing FRET pairs with ultrasound off and on. Blue diamond represents the mean of the data.**

It was expected that we would be able to observe variations in the FRET signal that correspond to the frequency of the ultrasound modulation (1 MHz). From our observations we were unable to detect any modulated signal. There are numerous explanations for the lack of observation but a likely explanation is the lack of influence the ultrasound has on the cumulative FRET signal within a freely diffusing medium. Within a freely diffusing FRET sample, the FRET pairs are likely moving with the overall bulk motion of the medium caused by the compression and rarefaction of the ultrasound within the medium. If there are any modulations of FRET pair distances, they likely coincide with modulations of FRET pair distance that cancel out in the averaging of the signal when measured. That is some FRET pairs might become closer together increasing FRET signal while other FRET pairs become further apart decreasing FRET signal. This could be improved by labeling ultrasound sensitive materials with the FRET pair at known distances. This is currently being done by groups to create ultrasound switachable fluorophores which are quenched via ultrasonic interaction [133-135]. Another possible explanation for the inability to measure modulated FRET signal is the limited sensitivity of the detection scheme

## 6.32 FRET Labeled Nanosponge Results and Discussion

Initial experiments showed that direct modulation of freely diffusing FRET labeled nanosponges was not observed with the chosen experimental methods. Figure 6 – 5 shows (top) the comparison between the observed AOM signal for the control DCM samples when ultrasound is off and on; (middle) the comparison between the observed AOM signal for the FRET labeled nanosponge sample when ultrasound is off and on; and (bottom) the comparison between observed AOM signal between the control DCM sample and the FRET labeled nanosponge sample when the ultrasound was on. Note: Median value is the middle red line in each box and the standard deviations are the whiskers. The top and bottom of each box represent the 75% and 25% percentiles of the data sample. The additional red crosses outside the whiskers represent outliers. Similar to the freely diffusing FRET sample results shown in figure 6 – 4, the results for the FRET labeled nanosponges are not visually conclusive. The measured AOM signal increased when ultrasound was on versus off for both the control CDM and the nanosponge samples but the AOM signal was slightly smaller in the comparions of the nanosponge sample with the control. The mean values were 72.8, 93.2, 77.6, 91.5 nV for the samples DCM US off, DCM US on, Nanosponges US off, and Nanosponges US on, respectively. The difference in the means were not statistically significant. It is assumed that the experimental methods used for the nanosponge sample contributed to similar inabilities to observe modulated signal as were seen in the freely diffusing FRET samples. Thus the freely diffusing nature of the nanosponges contribute an inability to observe modulated FRET signals as the compressions and rarefactions of the medium contribute alternating changes in the FRET signal which cancel out when measuring the averaged signal. Furthermore, the detection scheme to measure the FRET donor emission changes was not sensitive enough to observe anticipated changes. The introduction of a nanosponge created with an ultrasound sensitive polymer could possibly influence the ability to modulate the FRET signal observed.

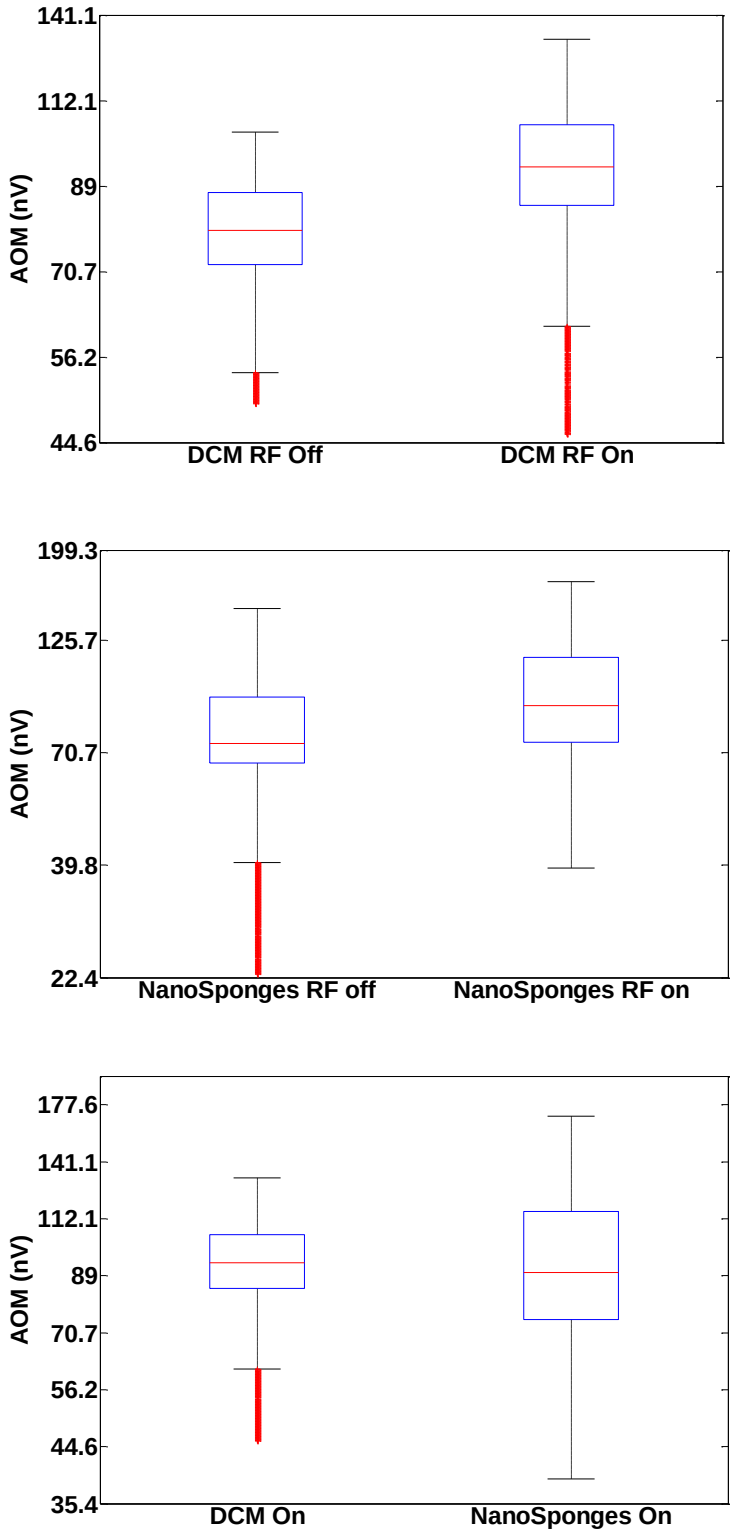


**Figure 6 - 5 Observations on the Direct modulation of nanosponges. (top) observed AOM signal for control sample DCM with ultrasound off and on. (middle) Observed AOM for FRET labeled nanosponges with ultrasound off and on. (bottom) Comparison between observed AOM for the control DCM and Nanosponge with ultrasound on.**

### 6.33 ZnS and ZnCdS Modulation Results and Discussion

Initial experiments showed that direct modulation of ZnCdS and ZnS was not observed to be statistically significant with the chosen experimental methods but was trending on significance. Figure 6 – 6 shows the initial experimental data comparing observed AOM amplitude for DMSO (control), ZnCdS, and ZnS when ultrasound was on. The mean values were $2.29x10^{-7}$, $2.32x10^{-7}$, and $2.19x10^{-7}$ V for DMSO, ZnCdS, and ZnS, respectively. A stastical ANOVA test was performed and provided a p value of 0.0519. Although not statistically significant, this p value was trending on signficance and it was determined to repeat the experiment adding additional blocks of data for each sample. These data are seen in figure 6 – 7.

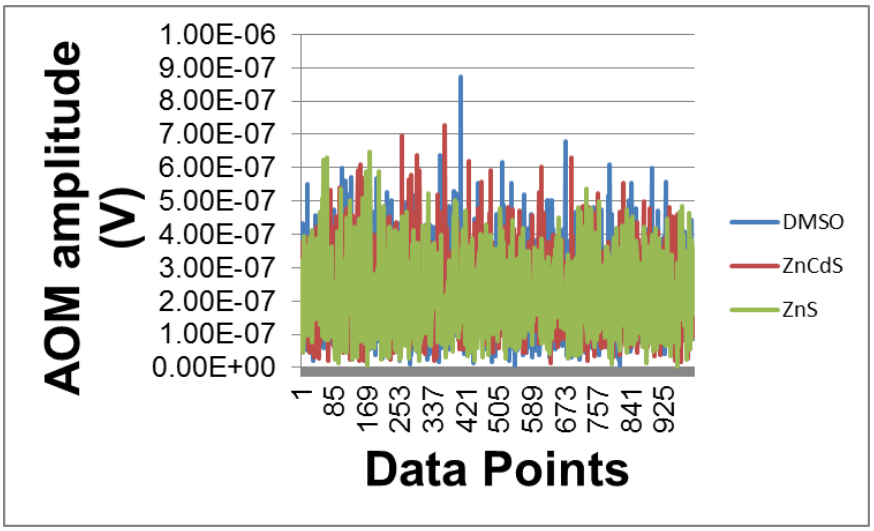


**Figure 6 - 6 Initial experimental data showing overlapping DMSO (control), ZnCdS, and ZnS AOM amplitude when ultrasound was on**

Figure 6 -7 shows the (top) AOM amplitude comparison between the control DMSO with ultrasound off vs on; (middle) AOM amplitude comparison between the ZnCdS with ultrasound off vs on and the comparison between ZnS with ultrasound off vs. on; (bottom) Normalized AOM amplitude comparison of DMSO vs ZnCdS and DMSO vs ZnS with ultrasound on. There is a

visual difference between all comparisons. $2.9x10^{-8}$, $1.38x10^{-7}$, $3.4x10^{-8}$ , $1.62x10^{-7}$, $3.0x10^{8}$ , and $1.43x10^{-7}$ V for DMSO US off, DMSO US on, ZnCdS US off, ZnCdS US on, ZnS US off, and ZnS US on, respectively. The bottom figure shows the AOM amplitudes of ZnCdS and ZnS with ultrasound on normalized to the mean DMSO US on signal. These values were $2.4x10^{-8}$ and $0.5x10^{-8}$ V for ZnCds and ZnS respectively. Both values proved to be stastically significant different from the DMSO mean with p values less than 0.001. This was anticipated as both ZnCdS and ZnS have been reported to have interactions with ultrasound in the past . We did not however anticipate the increase in signal seen in the DMSO sample when ultrasound was applied. Two possible explanations include (1) the introduction of additional cross talk between the ultrasound transmitter and the receiver within the detection system due to the applied ultraound signal; or (2) the introduction of sonoluminescense created by cavitation and emission of light within the DMSO sample. Neither of these explanations were able to be confirmed and thus the reasoning behind this increase in signal is unexplained currently.

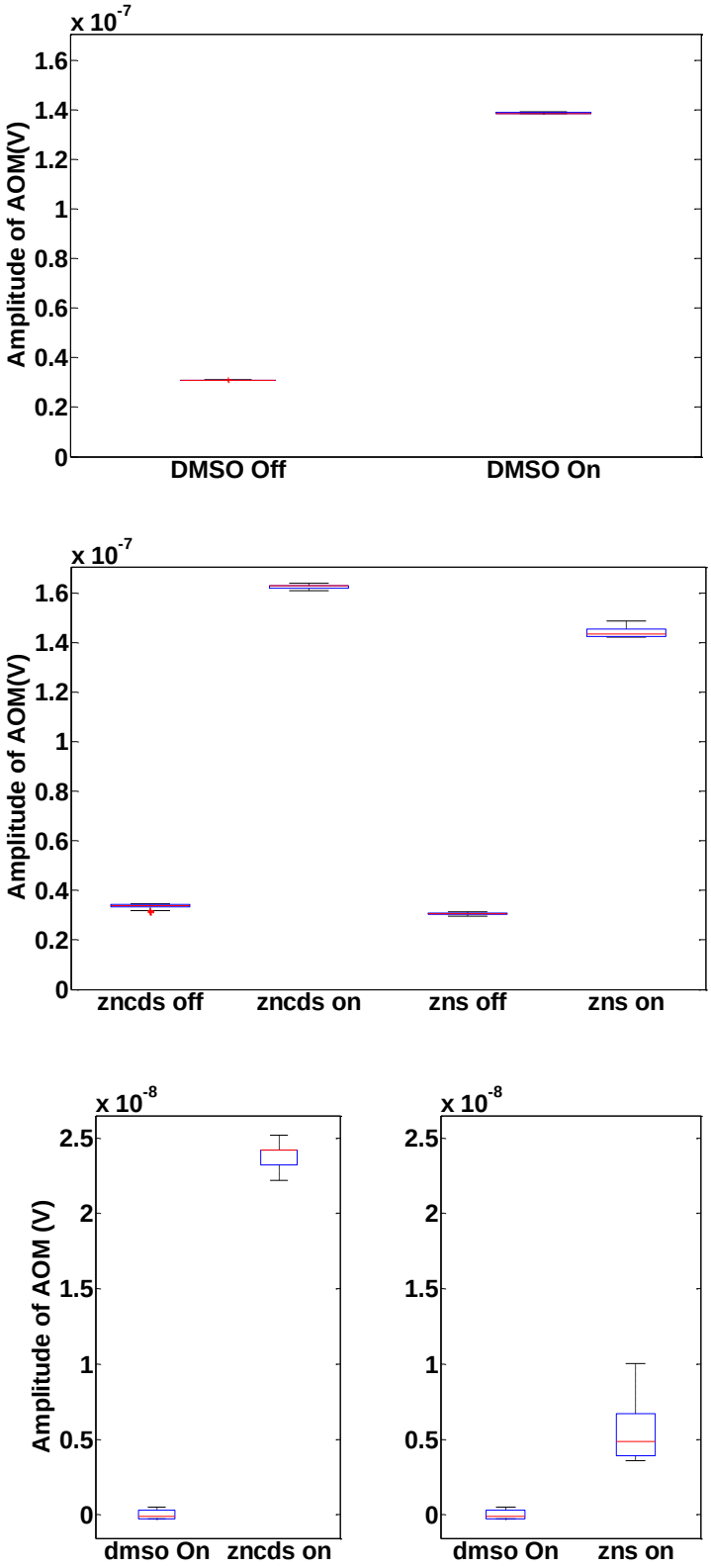


**Figure 6 - 7 Observations on the direct modulation of ZnCdS and ZnS (top) comparison of AOM amplitude for ultrasound off vs. on for control DMSO sample; (middle) comparison of AOM amplitude for ultrasound off vs. on for ZnCdS and ZnS; (bottom) comparison of Normalized AOM amplitude for DMSO vs. ZnCdS and DMSO vs. ZnS with ultrasound applied.**

## 6.4 Conclusion

In this chapter, we showed our results on the direct modulation of four chosen potential acousto-optic contrast agents, including freely diffusing FRET pairs, FRET labeled nanosponges, ZnCdS, and ZnS. Although both FRET based contrast agents showed no observed AOM in validation experiments, both ZnCdS and ZnS showed promise with observations of AOM with applied ultrasound. It is likely that the emissions of the FRET contrast agents could be modulated and observed with changes to the experimental methods including (1) changing the detection scheme to a more sensitive detection of the fluorescent lifetime; and (2) changing the medium the FRET agents are embedded in or attached to an ultrasound sensitive medium to enhance the effects of the ultrasound on the FRET pair distances. This is currently being done by Yuan et al. via thermosensitive polymers and is quite an advancement on the contrast agents we described. The observation of AOM within the ZnCdS and ZnS suspensions was anticipated but the ability to harness this property is not known. As mentioned previously, ZnCdS phosphorescent films were used for ultrasound detection in the past but the current state of acousto-optic imaging requires injectable or targeted contrast agents capable of improving modulation depth. Currently there is no known research that includes enhancing acousto-optical contrast agents with ZnCdS or ZnS but these could be an alternative to the current FRET based agents.

# Chapter 7

## Conclusions on the Physical Basis of Acousto-Optical Imaging

In this dissertation, it was aimed to demonstrate the modulation of incoherent light by ultrasound and investigate what factors affect the magnitude of such effects. In this chapter, the conclusions of this research will be discussed based on the reported findings. First, the conclusions of each specific aim will be summarized and discussed briefly. Next, the limitations of this research and its conclusions will be discussed. Finally, the future direction and suggestions for research within AOM of incoherent light will be discussed.

### 7.1 Specific aims

With the overall goal of this research being the demonstration and investigation of the ultrasonic modulation of incoherent light, three specific aims were set at the beginning. These aims were:

**Aim 1:** To design and develop instrumentation to detect and quantify Acousto-Optical interactions.

**Aim 2:** To evaluate the contributions of different mechanisms of ultrasonic modulation of fluorescence and the factors that influence these effects in turbid media like tissues

**Aim 3:** To test a variety of contrast agents to determine if their light output may be directly affected by ultrasonic modulation, which would suggest a novel approach to AOI

### 7.2 System Design and Development (Aim 1)

We were successful in aim 1 which was to design and develop instrumentation capable of detecting and quantifying Fluorescence and Acousto-Optical interactions. The design of this system was fully described in chapter 3, and was closely modelled after the experimental set-up reported by Kobayashi et al. [111]. The designed system is easily modified for varying

experimental methods. It is capable of a range of measurements including the ability to vary excitation sources as well as ultrasound sources. The system geometry can be varied readily, though the water tank is limited in size and input diameters for ultrasound transducers and optical windows. However, as the detection scheme is independent of the water tank, the experimental apparatus can be easily modified for future use. It is automated for three-dimensional stage movement and data collection.

The designed system was characterized in chapter 3 and shown capable of detecting fluorescence, having a minimum detectable concentration of 6.18 nM Rhodamine B (time constant = 10 s). Furthermore, the system was shown capable of detecting and quantifying Acousto-Optical signals in numerous experiments throughout this work, including the experimental findings reported in chapters 3, 4, 5, and 6. The initial experimental observation of Acousto-Optical signal showed ultrasound modulated fluorescence (UMF) intensity that scaled linearly with the squared ultrasound pressure. This was confirmed again in chapter 5, figure 5 – 2, where modulated incoherent LED light intensity was observed with modulation depth on the order of $10^{-8}$ which scaled linearly with squared ultrasound pressure.

### 7.3 Ultrasonic Modulation of Fluorescence (Aim 2)

We were successful in aim 2 which was to evaluate the contributions of different mechanisms of ultrasonic modulation of fluorescence and the factors that influence these effects in turbid media like tissues. The motivation for this work was provided by the experimental results reported by Kobayashi et al. [111, 112]. However, the results reported by Kobayashi were not repeated in our results despite our experimental apparatus being modeled after their reported system. Their results reported the ability to detect ultrasound modulated fluorescence only when ultrasound interacted with the fluorescent region of interest. They were able to distinguish this signal in the presence of AOM caused by modulation of the excitation source as well as observe the signal with great modulation efficiency within a dense scattering

medium without enhanced detection techniques. Our results in chapter 4 describe the detection of AOM signal which is dominated by modulated fluorescence caused by the ultrasound modulation of the excitation source. These results were not described by those of Kobayashi and thus the modulation mechanisms of the signals reported by Kobayashi remain unclear. Despite being unable to repeat the results by Kobayashi, we were capable of detecting modulated incoherent light without the presence of an excitation source in chapter 5. Our results in chapter 5, show that it is possible to modulate emitted incoherent light and detect this effect. However the ability to modulate the emitted incoherent light from a fluorophore remains unclear. Based on our results in chapter 5, modulating a fluorescent light source should be possible although the ability to distinguish this modulated fluorescence from the modulated fluorescence caused by modulated excitation is not predicted. To date, the results reported by Kobayashi et al. have yet to be repeated by any other of a number of groups. We did however show that modulated incoherent light could be generated and detected with an intensity and modulation depth that scale linearly with the squared ultrasound pressure (chapter 5, figure 2). Furthermore, our results in chapter 5 appear to show that ultrasound can impart a pattern in the projection of incoherent light that can be visualized by scanning the projection with a PMT and Slit combination and plotting the projection AOM intensity. As shown in chapter 5, this pattern appears to be a simple projection of the varying density caused by the ultrasound interaction within the LED illuminated ultrasound focal zone, without the need to invoke phase effects or variations in the real part of the wave velocity. The pattern appears to scale with system geometry as well as ultrasound frequency. In principle this type of coherent modulation of incoherent light could be used in novel imaging schemes, it may be relevant for the interpretation of some other studies, and may provide a novel way to image complex sound fields directly.

### 7.4 Direct Modulation of a Fluorophore (Aim 3)

Our study of the direct modulation of contrast agents was only partly successful in that we were able to observe modulation of both ZnCdS and ZnS. Although our observations on the direct modulation of freely diffusing FRET pairs and FRET labelled nanosponges did not prove the ability to modulate these samples, there are additional future experiments that could be performed to further interrogate such contrast agents. A few examples of future experiments include (1) labelling an ultrasound absorbing material with a FRET pair and observing FRET signal changes due to ultrasound; (2) embedding FRET labelled nanosponges in a thin film material to enhance the ultrasound effects on the nanosponge structure; and (3) creation of ultrasound sensitive fluorescent labelled nanosponges capable of quenching under ultrasonic pressures. The direct modulation of contrast agents may be the future of Acousto-Optical Imaging techniques as the modulation depth of AOI needs to be greatly increased to improve signal detection.

### 7.5 Limitations

As mentioned previously, this work was modelled after the initial findings of Kobayashi et al. The beginning of this work started in 2009 and the field has taken great steps since the inception of this work. The experimental apparatus designed is limited and could be upgraded in several ways to improve its abilities to interrogate acousto-optic interactions, although at significant cost. An enhancement to the system would be a new detection scheme with increased sensitivity. It would be beneficial to include a PMT detector or similar capable of photon counting and/or fluorescent lifetime measurements. This would allow further advances in the ability to explain the effects reported by Kobayashi. Furthermore, at the inception of this work, there had been no groups that had attempted to directly modulate the output of a contrast agent. This is no longer the case as Yuan et al. have made tremendous strides in the development of ultrasound sensitive polymers. Our work was limited not only by the detection

scheme but also by the contrast agents chosen. With the addition of ultrasound sensitive polymers, it is possible to further interrogate the interactions described by Kobayashi. Lastly, the designed system although flexible could be more fully automated and scaled to provide the future researcher with a benchtop Acousto-Optic Imaging system. In the current iteration, our system is only semi-automated and could be further refined.

### 7.5 Future Directions and Recommendations

With the results reported by Kobayashi being unrepeated to date, the future of this field relies on the ability to efficiently modulate a fluorescent signal in the presence of an excitation source. The question remains how the modulated fluorescence signal created by the modulated excitation source can be separated from the modulated fluorescent signal created by the ultrasound modulation of the fluorophore emissions. How Kobayashi was capable of this remains unclear. As the modulation depth of the modulated fluorescence created by the modulated excitation source is much larger than that of modulated fluorescence created by the ultrasound modulation of the fluorophore emissions, current research is focusing on increasing modulation depth. This is being done through the development of specialized imaging probes [95] as well as contrast agents designed to enhance the effect of ultrasound modulation.

A promising approach in the design of specialized contrast agents uses fluorescent microbubbles [132]. This work was the first demonstration of an ultrasound quenchable fluorescent microbubble. The ultrasound modulates the diameter of the microbubble, allowing the separation between surface fluorophores to be varied, effectively modulating the quenching efficiency. Another example of current research in ultrasound modulated fluorophores includes Yuan's work in ultrasound switchable NIR fluorophores [133-135]. These ultrasound switchable fluorophores were developed by encapsulating an environment sensitive indocyanine green (ICG) dye within thermosensitive nanoparticles. Without ultrasound, the nanoparticles are hydrophilic and fill with water which causes the ICG dye to not fluoresce. When ultrasound is

incident on the nanoparticles, the nanoparticles rapidly switch to hydrophobic, expelling the interior water and allowing the fluorescence intensity of the ICG dye to increase [134]. There are many promising opportunities and directions within Acousto-Optical Imaging techniques and this work should contribute to assisting in the decisions on future directions of AO research.

# Appendix

# Acousto-Optical Imaging System Operations Manual

## A1.0 Introduction

What follows is a detailed operating manual for the VUIIS Acousto-Optical Imaging System. This document will only cover the operation of the system. A detailed characterization of the system's hardware, specifications, and limitations can be found in Chapter 3. This system is the product of 5 years of design and development and thus all software that runs the system cannot be discussed in detail. We will discuss the main LabVIEW programs that are required to operate the system but the underlying programs that run within these main programs are left for the end user to interpret.

## A2.0 Quick Start Guide

This quick start guide serves as a step-by-step guide to starting the system and running a first experiment.

### A2.1 Step-by-Step Start-up Process

*ATTENTION! First time users should consult the detailed "System Start-Up and Operation" instructions in section 4.0 to ensure the system is not damaged as well as to avoid bodily injury caused by accidental exposure to RF injuries.*

1. **Power on the system**.
2. **Ensure RF power is set to an acceptable level.**
3. **Connect all desired connections to the oscilloscope**.
4. **Set desired waveform output on the function generator.**
5. **Set PMT control voltage on power supply module.**

6. **Start-up experimental control software.**

7. **Turn on RF power at the amplifier and with "BL2600_VI_01.vi"**.

8. **Utilize the "ImagingScan_2.3.vi" virtual instrument to control experiments.**

9. **Set Scan Settings in "ImagingScan_2.3.vi"**.

10. **Run Scan.**

11. **Save and Visualize data.**

**A3.0 Designed Acousto-Optical Imaging System**

A schematic of the designed system can be seen in figure A-1 below. Similar to previous systems, a laser excitation source (Sprout-G 6W, Lighthouse photonics) is focused via a 10x Galilean beam expander (BE10M, Thorlabs) to a 1.9 mm spot size. The laser light enters a custom built water bath. An ultrasound transducer (V314-SU-F, Panametrics/Olympus-NDT) is positioned perpendicular to the laser beam and is driven by a continuous sinusoidal wave generated by a function generator (Model 166, Wavetek), FG. A reference signal is also sent to a lock-in amplifier (SR844, Stanford Research Systems). An RF amplifier (Model 200L, Amplifier Research) is used to power the UST. The flexibility of our system allows the movement of the stages (XY Stages, TSB60-I, Zaber Technologies, Z Stage, Microkinetics) in three dimensions. We can move either the ultrasound transducer or the sample using custom designed holders. Signal is focused, filtered, and collected after the custom built water tank. A lens focuses the signal on a dichroic mirror, DF, (Di01-T488/532/594/638, Semrock) which transmits 95% of the excitation light (532 nm) and reflects light at the wavelength of the fluorophore (550-575 nm). Further emission/excitation filtering is performed to exclude any additional excitation light from the signal reaching the PMT. The Ems/Exc filter includes a 550 nm long-pass filter (NT47-617, Edmund Optics) and a band-pass filter (FF01-572/28, Semrock) which has a 572 nm center frequency with a 28 nm bandwidth. The PMT (H5783-20, Hamamatsu) collects the signal which is amplified by the accompanying pre-amplifier. Then the amplified signal is delivered to the

lock-in amplifier (LIA). The signal is then displayed on an oscilloscope (54503A, Hewlett Packard) and recorded by a custom LabView program on a dedicated custom computer server (Windows 7, Intel Core 2 Duo, 3.0 GHz, 3 GB RAM). A detailed list of system components can be found in table A - 1.

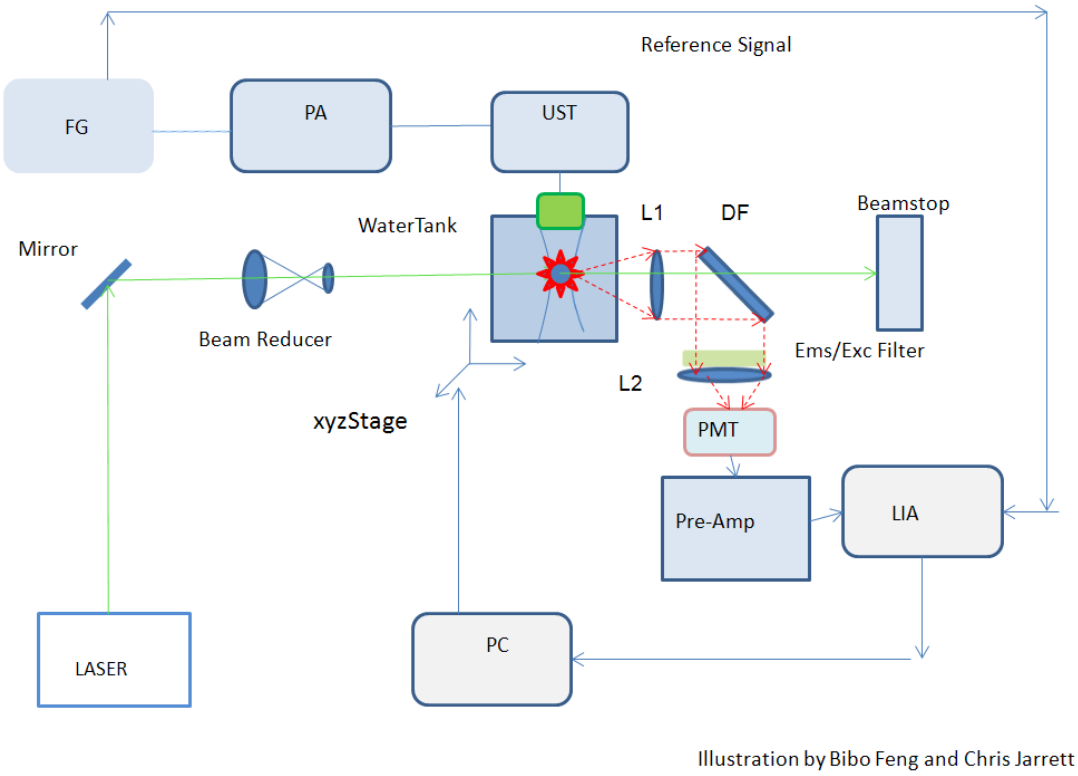


**Figure A - 1 Schematic of the custom designed AOI system**

**Table A-1: List of System Components**

| Abbreviation | Component | Model | Information |
|---|---|---|---|
| Laser | Light Source | LightHouse Photonics, Sprout-G 6W | DPSS 532nm laser, 6 W maximum power |
| FG | Function Generator | Wavetek, Model 166 | 0-50 MHz freq. range, 15 V p-p @50 Ω |
| PA | RF Power Amp. | Amplifier Research, Model 200L | Used at 0-8 W, capable of 200 W |
| UST | Ultrasound Transducer | Olympus-NDT, V314-SU-F | 1.5” Spherical Focus |
| Beam Reducer | Laser Beam Reducer | Thorlabs, BE10M | 10x Galilean Beam Reducer |
| XY Stage | XY Motion Control | Zaber Technologies, TSB60-I stage, T-LA60A-KT01 Actuator | 60 mm travel, 0.01 µm resolution |
| Z Stage | Z Motion | Microkinetics | 100 mm travel, 100 µm res. |
| Water Tank | Sample Tank | VUIIS, Ken Wilkens Custom | 130x180x100 mm, 5 windows for various 0.75” – 2” inserts |
| L1 | Focus Lens | Thorlabs, | 200 mm focal length |
| DF | Filter | Semrock, Di01-T488/532/594/638 | Transmits exc. light @532 nm reflects signal to the PMT |
| Ems/Exc Filter | Filter | Semrock, FF01-572/28 band pass filter | Transmits 558-586 nm signal |
| | | Edmund Optics, 550 nm Long pass Filter OD>2.0 | Transmits >550 nm signal |
| L2 | Focus Lens | Thorlabs, | 20 mm focal length |
| PMT | Light Detector | Hamamatsu, H5783-20 | Sens. 72 mA/W @532 nm |
| Pre-Amp | Signal Amplification | Hamamatsu, C6438 Amp, C7169 Power Supply | 20 dB gain, 0-1.2 V control |
| LIA | Lock-In Amplifier | Stanford Research Systems, SR844 | 25kHz – 200 MHz freq. range, 80 dB Dynamic range |
| Oscilloscope | Signal View | Hewlett-Packard, 54503A | dc-500 MHz, 1 mV/division |
| PC | Computer | Custom Server | Win. 7, 3.0 GHz |

### A3.1 Server

The AOI system consists of many interworking signal generation and signal collection devices. These devices all have to work in unison to allow the operation of this system in an efficient, accurate, precise, and repeatable manner. In order to operate this complex system of devices, a server was designed with accompanying software. This server allows the operation of each device in unison, the set-up of experimental procedures, and the storing and manipulation of data.

The server is a Dell Optiplex 760 PC labeled “Bounder.” It has an Intel Core2Duo CPU E8600 @ 3.33 GHz. There is 4.00 GB of Ram and the system is running Windows 7 ultimate service pack 1, 64-Bit Operating system. There is an 80 GB hard disk drive. All files for the AOI system are located on the Local Disk (C:) drive. The server’s IP address is: 192.168.0.100.

### A3.11 Windows XP Virtual Machine and VNC Viewer

When designing the system, it was necessary to operate a Windows XP virtual machine on the server as Windows 7 was a new operating system and a majority of the software needed to run the AOI system was not yet compatible with Windows 7. The Windows XP virtual machine can be accessed via the server’s desktop shortcut “Windows XP_Optics Lab.vmcx-Shortcut” or on the local disk, C:\Users\OptLab\Virtual Machines. The shortcut icon can be seen in figure A-2. All software needed to run the AOI system is located within LabVIEW on the Windows XP Virtual Machine on the server. The login for the XP virtual machine is User “OptLab” and password “laser”.


**Figure A - 2 Windows XP Virtual PC Icon**

In addition to the server, the system (and server) can be remotely accessed by utilizing VNC viewer. While connected to the Vanderbilt network, the VNC viewer software requires the following settings to operate the system remotely. When the VNC software application is

opened, the display will appear as Figure A-3 (left). The VNC server is optlab.dhcp.mc.vanderbilt.edu and the encryption is selected by VNC server. To connect to this server, the user selects “Connect” and the prompt shown in figure A-3 (right) is displayed. The username is left blank and the password to the system is “laser”. Upon logging in via VNC viewer, the user has complete access to the AOI system and can control experimental set-up and data storage.

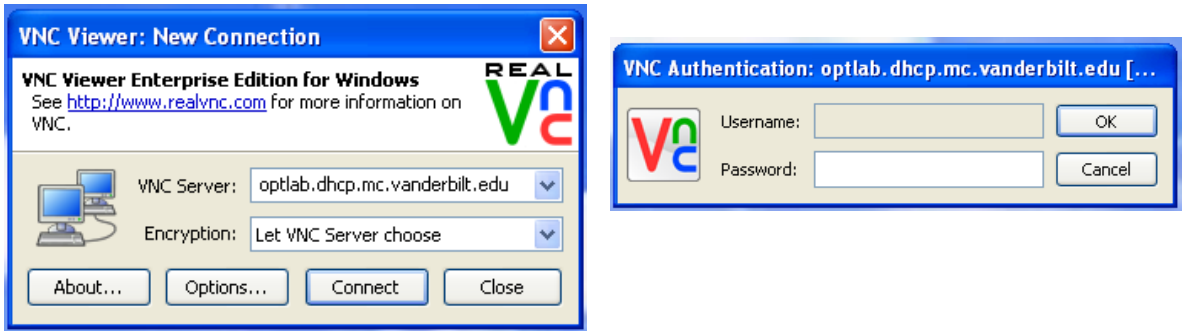


**Figure A - 3 (Left) VNC Viewer: New Connection (Right) Username and Password entry**

### A3.12 Additional Computers (PC named Charger, Laptop)

Since the system can be operated remotely, there are two additional computers in the lab that were set-up for remote access of the server. The first computer is a Dell Optiplex 755 labeled “charger”. Charger has an Intel Core 2 Quad Q9550 processor clocked @2.83 GHz with 3.25 GB of RAM. Windows XP Professional service pack 3 is the operating system. It has a 160GB hard disk drive. The second computer is a Dell latitude E5500 laptop. This laptop has an Intel Core 2 Duo R8700 processor clocked @2.53 GHz with 4.0 GB RAM. The system runs a 64-Bit Windows 7 Ultimate operating system. Upon startup, the user will see the OptLab icon which allows access to the laptop. The laptop password is “laser”. As this laptop was used initially to run the experiment, it will have a bit of the LabVIEW system software and some initial experimental data on the hard disk. However, the laptop is not a suitable replacement for the

server discussed previously. The laptop is too slow to run the AOI system in an efficient manner. The maximum experiment times were reduced from up to 10 hours with the laptop to 4 hours with the server, although typical scans are currently 45 minutes to 2 hours.

### A3.13 GPIB Control

The server connects with the data collection devices via GPIB control. A Rabbit RCM 3200 microcontroller allows remote control of data collection devices via GPIB. Using the LabVIEW Measurement & Automation Explorer, the devices connect to the server at the Agilent E5810A LAN/GPIB Gateway IP address 192.168.0.100 and the Rabbit microcontroller at 192.168.0.102. The assigned GPIB addresses are seen in the table below.

| Device | Model | Channel |
|---|---|---|
| Oscilloscope | HP54503A | 8 |
| Lock-In Amp | SR844 | 6 |
| Optional Spectrum Analyzer | Agilent N9010A | 18 |
| Optional Voltage Meter | Agilent 34401A | 10 |

Additional devices can be controlled via the GPIB control set-up using the LabVIEW Measurement & Automation Explorer.

### A3.14 System Software Components

The AOI system utilizes National Instruments LabVIEW software system to automate experiments as well as observing and recording experimental data. Using the Measurement & Automation Explorer coupled with the GPIB interface, LabVIEW controls not only the experimental set-up but also the recording of data from the oscilloscope, lock-in amplifier, RF

amplifier microcontroller (Rabbit102), and any additional devices connected to the system. In addition, the UBox USB Device Server software allows the connection and recording of data from the Thorlabs PM100D optical power meter used to monitor excitation power.

### A3.15 Essential LabVIEW Software

Within the Windows XP virtual machine set-up, numerous LabVIEW virtual instruments can be found that operate the various components of the AOI system. The directory of which is "\\tsclient\C\VUIIS\OptLab\LabVIEW". The majority of these virtual instruments have been combined into the "ImagingScan2.3.vi" virtual instrument. In addition to the "ImagingScan2.3.vi" virtual instrument, the "BL2600_VI_01.vi" virtual instrument is necessary in the operation of the system. The "BL2600_VI_01.vi" VI utilizes the Rabbit102 microcontroller to control the delivery of amplified RF power to the attached ultrasound transducer. The use of these programs to run the system will now be discussed in detail.

## A4.0 System Start-up and Operation

1. **Power on the system**. This includes powering on the PM100D optical power meter, Oscilloscope, Function Generator, Lock-In Amplifier, RF Amplifier, PMT Voltage Control, and PMT +5/-5 V power supply (located beneath the optics table and labeled).

   *Note: RF Amplifier does not power on just by pushing the "power" button. When pressed, the power light will come on and when the system is ready to be operated the "standby" light will light up. Here the "operate" button can be pressed to begin transmitting RF. It is suggested that the "operate" button is not pressed until the desired ultrasound transducer is connected and the RF power is set to an acceptable level to avoid damaging the transducer.*

2. **Ensure RF power is set to an acceptable level** to avoid an initial spike and damage to the ultrasound transducer. This can be done by setting the function generator's "Vernier Output Attenuation (dB)" knob to 60 dB on the outer knob and all the way to the left on the inner knob.

*Note: With both inner and outer knobs turned to the left, this is the smallest level of RF power being sent to the transducer when the RF amplifier is switched on.*

3. **Connect all desired connections to the oscilloscope**. The oscilloscope has 4 inputs that can be visualized. The most often used connections are that for the TTL out signal from the function generator and the coupled output of the RF amplifier.

*Note: Input channel 1 has been damaged in the past. It is not reliable for making system measurements as it does not behave as a 50 Ω load. It is however acceptable to visualize signals or for input of a trigger signal. Additionally, the input cable from the RF coupler is a signal that is -10 dB of the actual signal being supplied to the ultrasound transducer. This can be used to visualize and ensure that the RF power does not exceed the threshold value supplied to the US transducer. It is recommended that the $V_{p\text{-}p}$ of the coupled output from the RF amplifier not exceed 6-7 V. This equates to roughly 60-70 $V_{p\text{-}p}$ and is reaching the limit of the transducers at CW. The visualized waveform will begin to be non-sinusoidal when the limit is being approached indicating potential damage to the transducer if continued at this level.*

4. **Set desired waveform output on the function generator.** The function generator can control the frequency, wave shape, and power of the desired signal sent to the US transducer. The most common signal was a 1.041 MHz, sinusoidal signal with a 60 $V_{p\text{-}p}$

output at the transducer (6 $V_{p-p}$ read at the coupled RF output read on the oscilloscope after step 7). The RF amplifier output to the transducer is controlled by the function generator input to the amplifier. Using the “Vernier Output Attenuation (dB)” knob, the power should be gradually increasing the level of the innermost knob while in the 60 dB setting. If the 60 dB setting does not reach the desired output, the inner most knob can be turned all the way left to its minimum level and then the outer knob can be switched to 40 dB and so forth. Any setting over 40 dB on the outer knob risks damage to the transducer.

5. **Set PMT control voltage on power supply module.** The PMT module has a dedicated power supply that allows the control voltage to be manually set. The module allows for a 0-1.2 V control voltage. Manufacturer recommendations are to set the control voltage at 0.8 V to prolong the life of the detector. For the purposes of our experiments, the control voltages was often set between 0.5 V to 0.8 V.

6. **Start-up experimental control software.** Connect to the optics lab server via a VNC viewer connection using the password “laser”. Then start the “Windows XP_Optics Lab” Virtual PC. From the virtual PC there are three set-up steps to complete in order to perform most experiments. First, clicking the “UBox USB Device Server” icon, a GUI will appear showing the PM100D power module device. The “Action” box must be selected and the “status” will change to “connected”. Next, start-up “LabVIEW” and start the “BL2600_VI_01.vi” virtual instrument and the “ImagingScan.2.3.vi” virtual instrument.

7. **Turn on RF power at the amplifier and with “BL2600_VI_01.vi”**. Once the “operate” button is selected on the RF amplifier, the RF power can be turned on or off remotely using the “BL2600_VI_01.vi” virtual instrument. The front panel of the VI is shown below. To turn RF power supplied to the US transducer on or off, open the VI, click run, and then click start. A

string of numbers will appear in the “Received data:” box when the system is operating properly. The RF pulse should be set to “off”. To turn RF off or on select the box located next to the “Send Cmd” radio button that defaults to the string “Turn ON RF Gate Signal”. To turn on the signal, select “Send Cmd”. To turn off the signal, select “Turn OFF RF Gate Signal” and then select “Send Cmd”. When the RF is off, the “RF gate” button will light up green. To stop the VI, turn off the RF using described method and the “stop” button on the VI should be selected.

*Note: The “RF Pulse Width ms” and “RF Pulse Off Time ms” is preselected to 20 ms and 980 ms respectively. This ensures the duty cycle of the Transducer does not exceed that recommended by the manufacturer. Essentially, a continuous wave (CW) signal is cycled 20 ms on and 980 ms off for every second.*

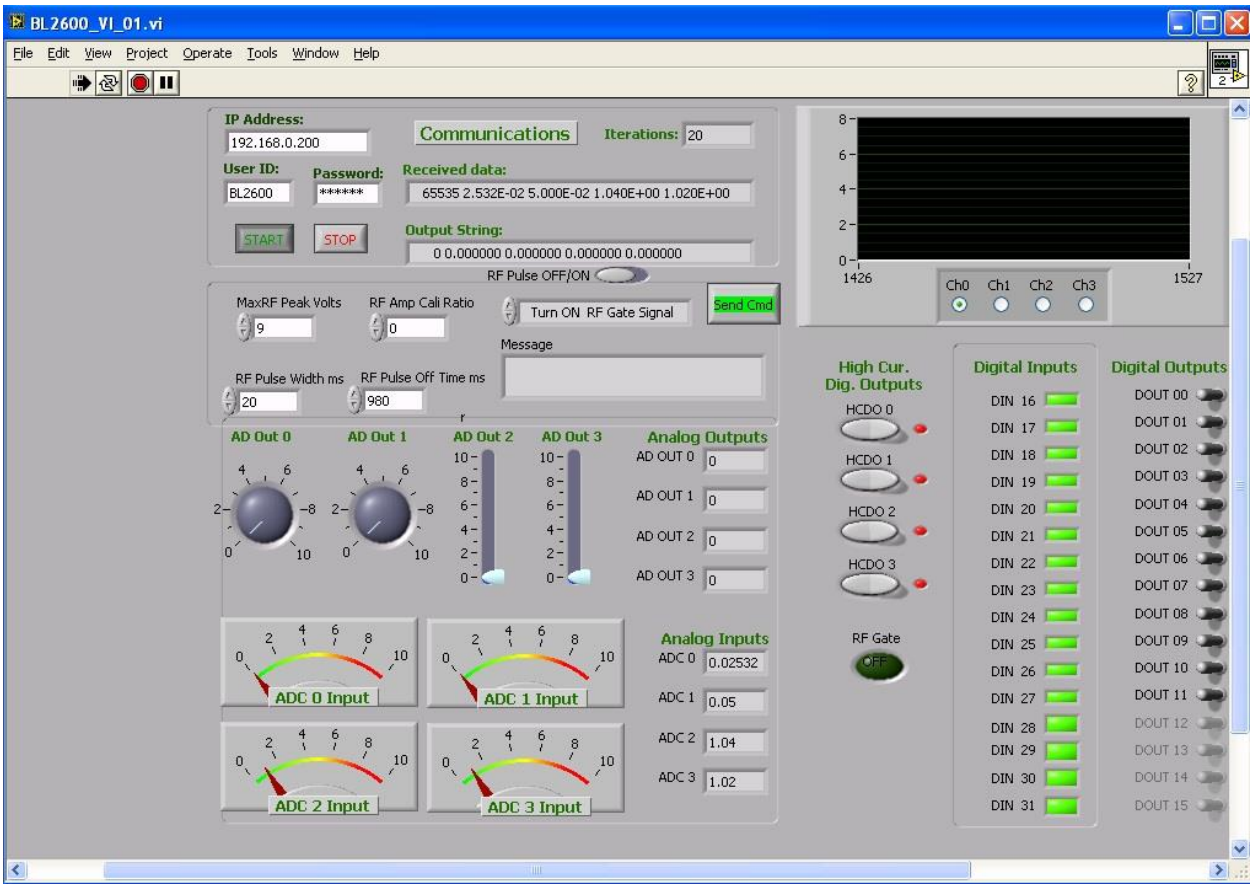


8. **Utilize the "ImagingScan_2.3.vi" virtual instrument to control experiments.** Turn on signal collection for each device used in the experiment by clicking the red button on the respective signal box within the Data Acq tab (See Below). The red light will turn green when signal acquisition is activated. The most common used devices are the HP5403a oscilloscope, the SR844 Lock-In Amplifier, and the PM100D optical power meter.

*Note: If excitation power measurements are desired, the user must align the optical power meter head in the desired measurement location and turn on signal collection with the UBox USB Device Server software.*

Signal acquisition can be verified by clicking “Grab Signal”, “SR844 Read”, or the green icon in the PM100D box. Also the number of data points collected per step is set here. Example if 200 is entered in the “Data per Step” box, there will be 200 data points recorded in the data file before the program steps the stages to the next step.

*Note: An error will occur if a system component is switched to record within the Data Acquisition when the system component is not itself powered on.*

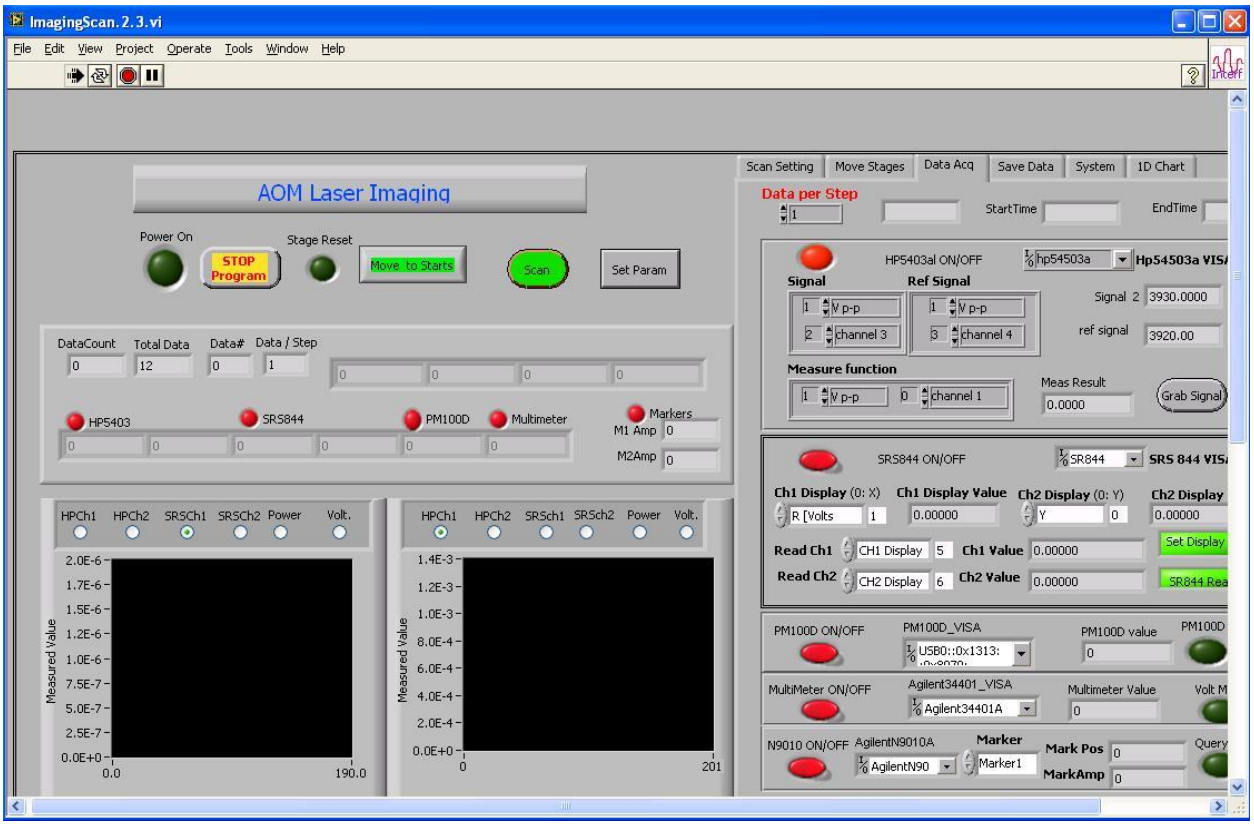


9. **Set Scan Settings in “ImagingScan_2.3.vi”**. To run a scan, the step size and number of steps within each axis should be set within the “Scan Setting” tab. The X and Y axis stages require a step size of 10000 to travel 1 mm and the  Z axis stage requires a step size of 1000 to travel 1 mm. For example, a 2500 step size on the X and Y stages would be a 0.25

mm step size but on the Z stage it would be 2.5 mm. Once the step size and no. of steps is input, the “Move Distance” will be automatically calculated.

*Note: The user must be aware of selected scan distances and the limitations of the stages and any physical barriers. The X and Y stages can be moved 60 mm each and the Z stage can be moved 100 mm but due to the varying experimental set-up conditions, it is recommend that the user moves stages manually to the desired start and finish positions to ensure the stages do not make impact and cause damage to the system.*

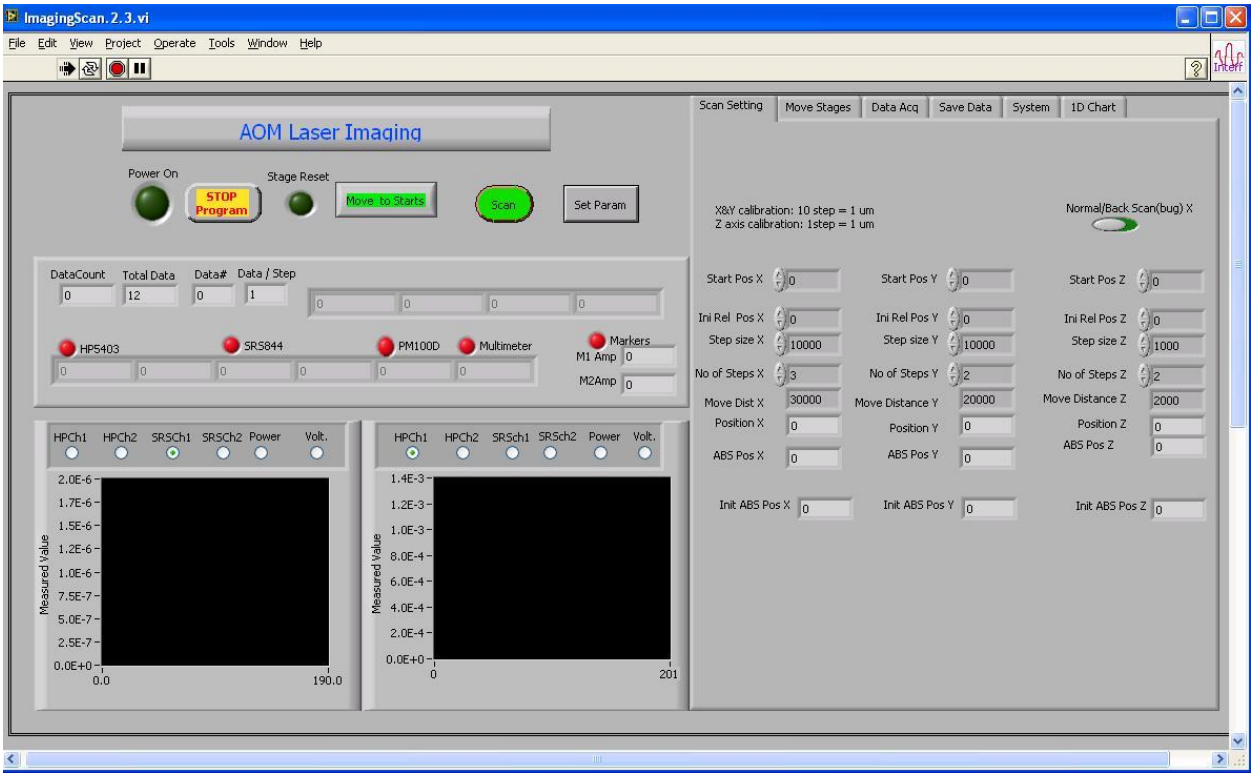


10. **Run Scan.** With the LabVIEW “ImagingScan2.3.vi” virtual instrument running, the experiment can be performed as set-up in the previous steps by clicking the green “Scan” button.

*Note: The "STOP Program" button only stops the program once the entire experimental procedure has been completed. To stop the program in an emergency, LabVIEW must be closed. This will leave the stages at the last data point prior to the closure and the stages must be reset to the starting position. "Move to Starts" will only move the stages to the starts of the last run program and the default is to home position for all of the stages.*

11. **Save and Visualize data.** Data can be saved in the "Save Data" tab and can be visualized in the "1D Chart" tab. Further visualization can be performed by importing the data into a program such as Matlab.

    Data is saved in a ".txt" file with the following format.

#File Directory and Attached Name ..\..\EXPDATA\,znsRFon2

# add comments to file

#Data per Step, 2E+4

#Exp_Date_StartTime_EndTime_FileNumber, 130326,205642,211338,1E+1

#axis, init RelativePos, Step, Num of steps, Abs Pos

#X-Axis, 0.000000E+0,1.000000E+0,1,582966

#Y-Axis, 0.000000E+0,1.000000E+0,1,200000

#Z-Axis, 0.000000E+0,1.000000E+0,1,0

#data number,X pos,Y pos, Z pos, Sig (v),Ref(v),SRS Ch1,Ch2, Laser PW, multimeter V, Marker1 Freq, Marker1 Amp, Marker2 Freq, Marker2 Amp

Where the most commonly used data are StartTime, EndTime, X pos, Y pos, Z pos, Sig(v), and

SRS Ch1. Of these StartTime and EndTime are given in military time of hhmmss and can be used to calculate the length of the scan. X pos, Y pos, Z pos, are used to give the 3 dimensional locations of the current data point. Sig(v) gives the -10 dB coupled RF power at the Oscilloscope and can be used to calculate the actual RF power reaching the ultrasound transducer. Of note, the Sig(v) should be closely monitored to ensure damage does not occur to the US transducers. A common maximum value for Sig(v) would be ~6 volts and values over 7 volts are increasing the risk of US transducer and/or RF coupler damage. Finally, the SRS Ch1 gives the channel 1 signal reaching the lock-in amplifier with the frequency of the supplied reference signal. This signal is an amplitude, and must be squared to provide the signal intensity.

**A5.0 Data Processing**

It is often common for the user to analyze and visualize the experimental data with a third party data analysis software (e.g. Matlab) as the 1D Chart is limited. Due to an infinite number of varying experimental parameters it is left to the user to understand which data columns must be visualized and how to do so. Often the data must be pre-processed to allow the user to analyze the data efficiently. Removing the column headers and formatting the ".txt" file to a ".dat" file is the most often pre-processing technique and can done either automatically through a user defined Matlab code or by manually stripping the data of this information with a text editing software such as Microsoft Excel. Another pre-processing technique often performed is the averaging of data. Within the LabVIEW "ImagingScan2.3.vi" virtual instrument, the user can specify the number of data to be recorded at each data point. This will cause the text file to list all data at each point in succession before moving the stages and recording the next data point within a scan. Again, the user is responsible for the automation or manual averaging of this data to ensure accurate visualization of data.

### A5.1 Matlab processing and code

An automated Matlab M file (ProcessDataFile.m) has been written that will provide a visualization of data. The links to these files can be found on the desktop of the server as well as the Windows XP virtual machine. In order for this program to be used, the ProcessDataFile.m and the ProcessDataFile.fig files must be located within the current directory being used in Matlab. The code can be found at the end of this appendix.

Often the automated ProcessDataFile.m program is not capable of performing the user desired analysis of the data and thus a manual entry and visualization of the data can be performed using the Matlab code below.

```
clear all
close all

% Load data file
% File has been pre-processed such that x data is column 1, y data is
% column 2, and SRS ch1 data is inserted for the z data in column 3. This
% allows a 3D (x,y,intensity) visualization of the data.

load filename.dat

% assign x and y coordinates and make a meshgrid
x=filename(:,1);
y=filename(:,2);
[X Y]=meshgrid(x,y);

% assign z coordinates
z=filename(:,3);

% create a
xu=unique(x);
yu=unique(y);

% create an array of zeros to be filled later with dimensions xu,yu
zm=zeros(length(yu),length(xu));

% Insert data into the zm array in the proper location
for m=1:length(xu)
for n=1:length(yu)
zm(n,m)=z(find(x==xu(m)&y==yu(n)));
end
end

% visualize data using mesh, surf, plot, etc
```

```
mesh(xu,yu,zm)

% label the axis
xlabel('x scan')
ylabel('y scan')
zlabel('z values')
```

**ProcessDataFile.m and ProcessDataFile.fig**

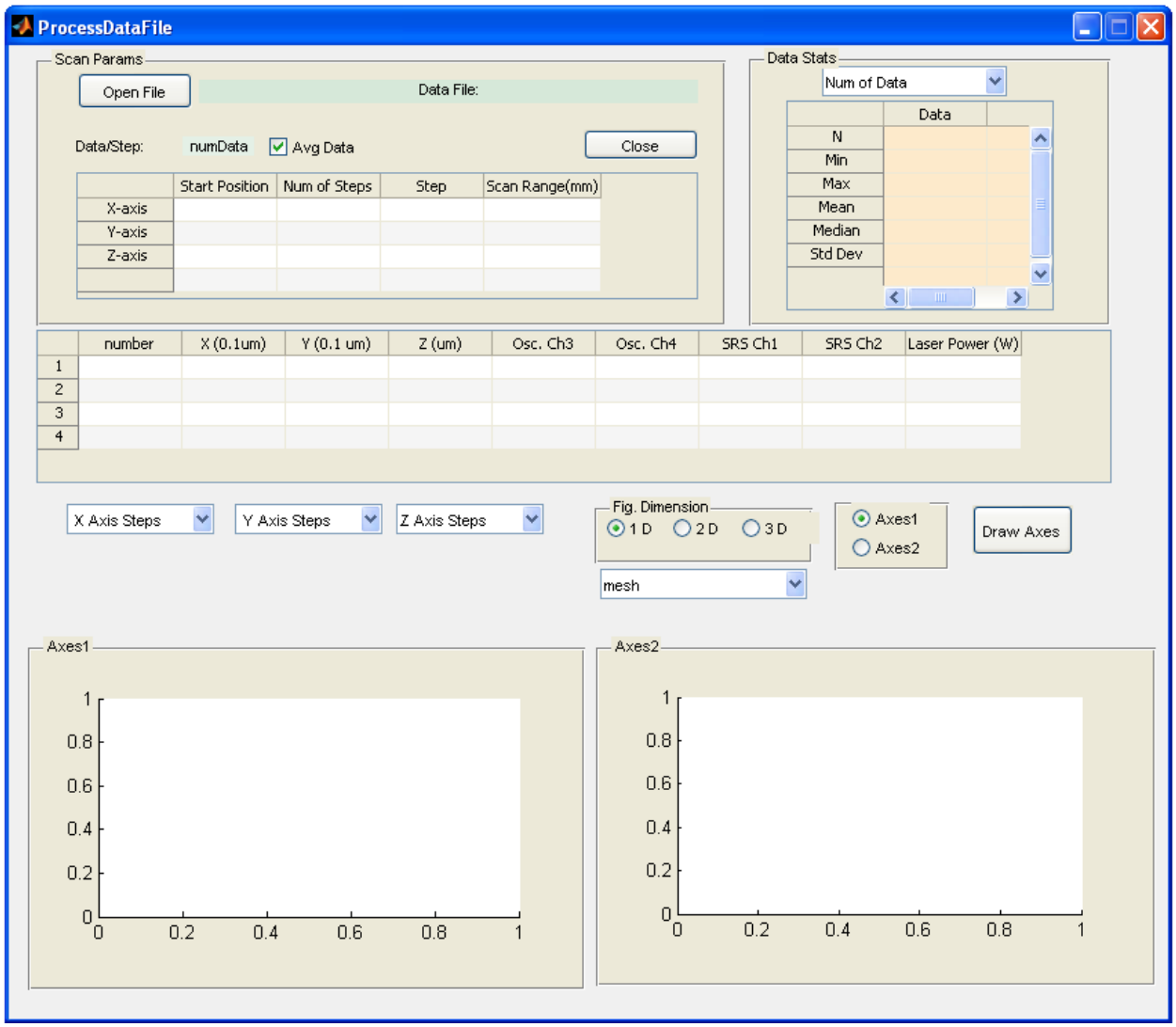


```
%%
%%
% This program reads the experimental scanning data and plots its
% 1d,2d and 3d figures.
```

```
%
% Version: 0.1
% Date: March 26, 2012
% Bibo Feng
%
%
function varargout = ProcessDataFile(varargin)
% PROCESSDATAFILE MATLAB code for ProcessDataFile.fig
%      PROCESSDATAFILE, by itself, creates a new PROCESSDATAFILE or raises the existing
%      singleton*.
%
%      H = PROCESSDATAFILE returns the handle to a new PROCESSDATAFILE or the
handle to
%      the existing singleton*.
%
%      PROCESSDATAFILE('CALLBACK',hObject,eventData,handles,...) calls the local
%      function named CALLBACK in PROCESSDATAFILE.M with the given input arguments.
%
%      PROCESSDATAFILE('Property','Value',...) creates a new PROCESSDATAFILE or raises
the
%      existing singleton*. Starting from the left, property value pairs are
%      applied to the GUI before ProcessDataFile_OpeningFcn gets called. An
%      unrecognized property name or invalid value makes property application
%      stop. All inputs are passed to ProcessDataFile_OpeningFcn via varargin.
%
%      *See GUI Options on GUIDE's Tools menu. Choose "GUI allows only one
%      instance to run (singleton)".
%
% See also: GUIDE, GUIDATA, GUIHANDLES

% Edit the above text to modify the response to help ProcessDataFile

% Last Modified by GUIDE v2.5 03-Apr-2012 10:30:56

% Begin initialization code - DO NOT EDIT
gui_Singleton = 1;
gui_State = struct('gui_Name',       mfilename, ...
                   'gui_Singleton',  gui_Singleton, ...
                   'gui_OpeningFcn', @ProcessDataFile_OpeningFcn, ...
                   'gui_OutputFcn',  @ProcessDataFile_OutputFcn, ...
                   'gui_LayoutFcn',  [] , ...
                   'gui_Callback',   []);
if nargin && ischar(varargin{1})
    gui_State.gui_Callback = str2func(varargin{1});
end

if nargout
    [varargout{1:nargout}] = gui_mainfcn(gui_State, varargin{:});
else
    gui_mainfcn(gui_State, varargin{:});
end
```

```
% End initialization code - DO NOT EDIT


% --- Executes just before ProcessDataFile is made visible.
function ProcessDataFile_OpeningFcn(hObject, eventdata, handles, varargin)
% This function has no output args, see OutputFcn.
% hObject    handle to figure
% eventdata  reserved - to be defined in a future version of MATLAB
% handles    structure with handles and user data (see GUIDATA)
% varargin   command line arguments to ProcessDataFile (see VARARGIN)

% Choose default command line output for ProcessDataFile
handles.output = hObject;

% Update handles structure
guidata(hObject, handles);

initParame(hObject, handles);

% UIWAIT makes ProcessDataFile wait for user response (see UIRESUME)
% uiwait(handles.figure1);

function initParame(hObject, handles)
%set(handles.figDim,  'Data',1);  %set init params
%set(handles.figAxes, 'Data',1);
 handles.figDim = 1;  %set init params
 handles.figAxes= 1;

       set(handles.ppmXAxis,'Enable','on');
       set(handles.ppmYAxis,'Enable','off');
       set(handles.ppmZAxis,'Enable','off');
       set(handles.ppmSelectDraw,'Visible','off');

% Update handles structure
guidata(hObject, handles);


% --- Outputs from this function are returned to the command line.
function varargout = ProcessDataFile_OutputFcn(hObject, eventdata, handles)
% varargout  cell array for returning output args (see VARARGOUT);
% hObject    handle to figure
% eventdata  reserved - to be defined in a future version of MATLAB
% handles    structure with handles and user data (see GUIDATA)

% Get default command line output from handles structure
varargout{1} = handles.output;


% --- Executes on button press in openFile.
function openFile_Callback(hObject, eventdata, handles)
% hObject    handle to openFile (see GCBO)
```

```
% eventdata  reserved - to be defined in a future version of MATLAB
% handles    structure with handles and user data (see GUIDATA)
%readDataFile;

[fname,pname] = uigetfile('*.*','Enter data file');

%fid = fopen('data.txt');
%fname = 'data.txt';
%fname = '2dScanData.txt';
%pname='';

 if (fname ~= 0)
  filename = sprintf('%s%s',pname,fname);
  handles.filename = filename;
  %readExpDataFile(filename);

    %fid = fopen('data.txt');
    fid = fopen(filename);

    %Read  lines from file, removing newline characters
    tline = fgetl(fid);
    while ischar(tline)
      if strncmpi(tline,'#Data per Step',14)
          dataPerStep = textscan(tline,'%s %d',2,'delimiter',',');
          handles.dataPerStep = dataPerStep;
      end
      %read x, y, z axis parameters
      if strncmpi(tline,'#X-Axis',7)
          x_axis = textscan(tline,'%s %d %d %d %d',5,'delimiter',',');
      end
      if strncmpi(tline,'#Y-Axis',7)
          y_axis = textscan(tline,'%s %d %d %d %d',5,'delimiter',',');
      end
      if strncmpi(tline,'#Z-Axis',7)
          z_axis = textscan(tline,'%s %d %d %d %d',5,'delimiter',',');
      end

      % read column headers
      if strncmpi('#data number',tline,12)
          colTitles = textscan(tline,'%s %s %s %s %s %s %s %s %s %s ',8,'delimiter',',');
          handles.expDataTitle = colTitles;
          break;
      end

       tline = fgetl(fid);
    end

    % read numeric data
    ColData = textscan(fid, '%d %d %d %d %f %f %f %f %f');
    %C_data0 = textscan(fid, '%d %d %d %d %f %f %f %f %f', 'CollectOutput',1)
```

```
    fclose(fid);

    %set parameters
      set(handles.txtFileName, 'String', fname);
      set(handles.txtNumData, 'String', dataPerStep[113]);
      tblScan{1,1} = x_axis{5};
      tblScan{1,2} = x_axis[113];
      tblScan{1,3} = x_axis{3};
      tblScan{1,4} =  x_axis{3}*x_axis[113]/10;

      tblScan{2,1} = y_axis{5};
      tblScan{2,2} = y_axis[113];
      tblScan{2,3} = y_axis{3};
      tblScan{2,4} =  y_axis{3}*y_axis[113]/10;

      tblScan{3,1} = z_axis{5};
      tblScan{3,2} = z_axis[113];
      tblScan{3,3} = z_axis{3};
      tblScan{3,4} =  z_axis{3}*z_axis[113]/10;



 end
 %update tblScan in gui
 set(handles.tblScan,'Data',tblScan);

% expData = ColData;
avg = get(handles.ckbAvgData,'Value');
avgData = avgAcqData(ColData,dataPerStep[113],avg); %num number of data acq per step

set(handles.tblExpData, 'Data',avgData);
 guidata(hObject,handles);


function avgData = avgAcqData(ColData,num,avg) %num number of data acq per step
%num: number data per steps
%avg 1:need average data in num data per step
avgData=[];
tmpData = [];
k = size(ColData,2);

    for j=1:k
        tmpData(:,j)=ColData{1,j};
    end
steps= size(tmpData,1);
sum=0.0;idx =0;
dnum=double(num); %convert int to double data
if num == 1  %only 1 data per step
   avgData = tmpData;
else if avg == 0
        avgData = tmpData;
```

```
    else %average the data on each scan step
      for j=1:k
          index =1;
          for i = 1:steps
              sum = sum + tmpData(i,j);
              idx = idx + 1;
              if idx == num
               avgData(index,j)= sum/dnum;
               sum = 0;
               idx = 0;
               index = index +1;
              end
              %avgData(i,j)=mean(tmpData(i:num,j);
          end
       end
    end
end



% --- Executes on button press in Close.
function Close_Callback(hObject, eventdata, handles)
% hObject    handle to Close (see GCBO)
% eventdata  reserved - to be defined in a future version of MATLAB
% handles    structure with handles and user data (see GUIDATA)

user_response = modaldlg('Title','Confirm Close');
%user_response = 'yes';
switch lower(user_response)
case 'no'
    % take no action
case 'yes'
    % Prepare to close GUI application window
    delete(handles.figure1)
end



% --- Executes on button press in btnTest.
function btnTest_Callback(hObject, eventdata, handles)
% hObject    handle to btnTest (see GCBO)
% eventdata  reserved - to be defined in a future version of MATLAB
% handles    structure with handles and user data (see GUIDATA)
  set(handles.txtFileName, 'String', 'file - name');


% --- Executes on selection change in ppmXAxis.
function ppmXAxis_Callback(hObject, eventdata, handles)
% hObject    handle to ppmXAxis (see GCBO)
% eventdata  reserved - to be defined in a future version of MATLAB
% handles    structure with handles and user data (see GUIDATA)
```

```
% Hints: contents = cellstr(get(hObject,'String')) returns ppmXAxis contents as cell array
%        contents{get(hObject,'Value')} returns selected item from ppmXAxis


% --- Executes during object creation, after setting all properties.
function ppmXAxis_CreateFcn(hObject, eventdata, handles)
% hObject    handle to ppmXAxis (see GCBO)
% eventdata  reserved - to be defined in a future version of MATLAB
% handles    empty - handles not created until after all CreateFcns called

% Hint: popupmenu controls usually have a white background on Windows.
%       See ISPC and COMPUTER.
if ispc && isequal(get(hObject,'BackgroundColor'), get(0,'defaultUicontrolBackgroundColor'))
    set(hObject,'BackgroundColor','white');
end


% --- Executes on selection change in ppmYAxis.
function ppmYAxis_Callback(hObject, eventdata, handles)
% hObject    handle to ppmYAxis (see GCBO)
% eventdata  reserved - to be defined in a future version of MATLAB
% handles    structure with handles and user data (see GUIDATA)

% Hints: contents = cellstr(get(hObject,'String')) returns ppmYAxis contents as cell array
%        contents{get(hObject,'Value')} returns selected item from ppmYAxis


% --- Executes during object creation, after setting all properties.
function ppmYAxis_CreateFcn(hObject, eventdata, handles)
% hObject    handle to ppmYAxis (see GCBO)
% eventdata  reserved - to be defined in a future version of MATLAB
% handles    empty - handles not created until after all CreateFcns called

% Hint: popupmenu controls usually have a white background on Windows.
%       See ISPC and COMPUTER.
if ispc && isequal(get(hObject,'BackgroundColor'), get(0,'defaultUicontrolBackgroundColor'))
    set(hObject,'BackgroundColor','white');
end


% --- Executes on selection change in ppmZAxis.
function ppmZAxis_Callback(hObject, eventdata, handles)
% hObject    handle to ppmZAxis (see GCBO)
% eventdata  reserved - to be defined in a future version of MATLAB
% handles    structure with handles and user data (see GUIDATA)

% Hints: contents = cellstr(get(hObject,'String')) returns ppmZAxis contents as cell array
%        contents{get(hObject,'Value')} returns selected item from ppmZAxis
```

```
% --- Executes during object creation, after setting all properties.
function ppmZAxis_CreateFcn(hObject, eventdata, handles)
% hObject    handle to ppmZAxis (see GCBO)
% eventdata  reserved - to be defined in a future version of MATLAB
% handles    empty - handles not created until after all CreateFcns called

% Hint: popupmenu controls usually have a white background on Windows.
%       See ISPC and COMPUTER.
if ispc && isequal(get(hObject,'BackgroundColor'), get(0,'defaultUicontrolBackgroundColor'))
    set(hObject,'BackgroundColor','white');
end


% --- Executes on button press in btnDrawAxes.
function btnDrawAxes_Callback(hObject, eventdata, handles)
% hObject    handle to btnDrawAxes (see GCBO)
% eventdata  reserved - to be defined in a future version of MATLAB
% handles    structure with handles and user data (see GUIDATA)


% Plot one axes at a time, changing data; first the population
dataTable = get(handles.tblExpData,'Data'); % Obtain the data table
% Choose appropriate axes
if isequal(handles.figAxes,1)
    axes = handles.axes1;
elseif isequal(handles.figAxes,2)
    axes = handles.axes2;
end

switch handles.figDim % Get Tag of selected object.
    case 1
        % Code for when radiobutton1 is selected.
         drawOneDimFigure(dataTable,handles,axes);
    case 2
        % Code for when radiobutton2 is selected.

        drawTwoDimFigure(dataTable,handles,axes);

    case 3
        % Code for when radiobutton2 is selected.

        drawThreeDimFigure(dataTable,handles,axes);
end


%%Draw one dimension figure
function drawOneDimFigure(dataTable,handles,axes)
xDimIdx = get(handles.ppmXAxis,'Value');
xStrlist = get(handles.ppmXAxis,'String');
if handles.figAxes ==1
    hAxes = handles.panAxes1;
```

```
    sAxes = 'Axes1';
else
    hAxes = handles.panAxes2;
    sAxes = 'Axes2';
end


%set(handles.panAxes1, 'Title', strcat('Axes',int2str(handles.figAxes),': Data number  vs.
',xStrlist(xDimIdx)));
 set(hAxes, 'Title', strcat(sAxes , ': Data number  vs. ',xStrlist(xDimIdx)));

 n =  size(dataTable,1);
plot(axes,1:n,dataTable(:,xDimIdx),'LineWidth',2);

xlabel(axes, 'Data number');
ylabel(axes, xStrlist(xDimIdx));

%% Draw Two dimension (2d plot)
function drawTwoDimFigure(dataTable,handles,axes)
xDimIdx = get(handles.ppmXAxis,'Value');
yDimIdx = get(handles.ppmYAxis,'Value');
xStrlist = get(handles.ppmXAxis,'String');
yStrlist = get(handles.ppmYAxis,'String');

if handles.figAxes ==1
    hAxes = handles.panAxes1;
    sAxes = 'Axes1';
else
    hAxes = handles.panAxes2;
    sAxes = 'Axes2';
end

%set(handles.panAxes1, 'Title', strcat('Axes',int2str(handles.figAxes),': Data number  vs.
',xStrlist(xDimIdx)));
 set(hAxes, 'Title', strcat(sAxes ,': ', xStrlist(xDimIdx), ' vs. ',yStrlist(yDimIdx)));

plot(axes,dataTable(:,xDimIdx),dataTable(:,yDimIdx),'LineWidth',2);

xlabel(axes, xStrlist(xDimIdx));
ylabel(axes, yStrlist(yDimIdx));


%% Draw Three dimension (3d plot)
function drawThreeDimFigure(dataTable,handles,axes)
xDimIdx = get(handles.ppmXAxis,'Value');
yDimIdx = get(handles.ppmYAxis,'Value');
zDimIdx = get(handles.ppmZAxis,'Value');

%yDimIdx = get(handles.ppmYAxis,'Value');
xStrlist = get(handles.ppmXAxis,'String');
yStrlist = get(handles.ppmYAxis,'String');
```

```
zStrlist = get(handles.ppmZAxis,'String');

if handles.figAxes ==1
    hAxes = handles.panAxes1;
    sAxes = 'Axes1';
else
    hAxes = handles.panAxes2;
    sAxes = 'Axes2';
end
set(hAxes, 'Title', strcat(sAxes ,':  ', xStrlist(xDimIdx), ' , ',yStrlist(yDimIdx), ' vs.
',zStrlist(zDimIdx)));


F = TriScatteredInterp(dataTable(:,xDimIdx),dataTable(:,yDimIdx),dataTable(:,zDimIdx));
[qx,qy] = meshgrid(dataTable(:,xDimIdx),dataTable(:,yDimIdx));
qz = F(qx,qy);

vDraw = get(handles.ppmSelectDraw,'Value');
sDraw = get(handles.ppmSelectDraw,'String');

%select type of 3d drawings
switch  char(sDraw(vDraw))
    case 'mesh'
        mesh(axes,qx,qy,qz);
    case 'contour'
        contour(axes,qx,qy,qz);
    otherwise
            mesh(axes,qx,qy,qz);
end

 xlabel(axes, xStrlist(xDimIdx));
 ylabel(axes, yStrlist(yDimIdx));
 zlabel(axes, zStrlist(zDimIdx));




% --- Executes on button press in btnDataStats.
function btnDataStats_Callback(hObject, eventdata, handles)
% hObject    handle to btnDataStats (see GCBO)
% eventdata  reserved - to be defined in a future version of MATLAB
% handles    structure with handles and user data (see GUIDATA)
% Get the stats table from the gui



% --- Executes on selection change in ppmStatsData.
function ppmStatsData_Callback(hObject, eventdata, handles)
% hObject    handle to ppmStatsData (see GCBO)
% eventdata  reserved - to be defined in a future version of MATLAB
% handles    structure with handles and user data (see GUIDATA)
```

```
% Hints: contents = cellstr(get(hObject,'String')) returns ppmStatsData contents as cell array
%        contents{get(hObject,'Value')} returns selected item from ppmStatsData
dataColindex = get(hObject,'Value');    % What plot type is requested?
                                % add 3 to match the  col of expData table
strlist = get(hObject,'String');        % Get the choice's name

% Plot one axes at a time, changing data; first the population
dataTable = get(handles.tblExpData,'Data'); % Obtain the data table

% Get the stats table from the gui
stats = get(handles.tblStats, 'Data');
% Generate the stats for the selection
stats = setStats(dataTable, stats, dataColindex);
% Replace the stats in the gui with the updated ones
set(handles.tblStats, 'Data', stats);

function stats = setStats(table, stats, col)
% Computes basic statistics for data table.
%   table  The data to summarize (a population or selection)
%   stats  Array of statistics to update
%   col    Which column of the array to update
%   peak   Value for the peak period, computed externally

stats{1,1} =   size(table,1);      % Number of rows
stats{2,1} =    min(table(:,col));
stats{3,1} =    max(table(:,col));
stats{4,1} =   mean(table(:,col));
stats{5,1} = median(table(:,col));
stats{6,1} =    std(table(:,col));


% --- Executes during object creation, after setting all properties.
function ppmStatsData_CreateFcn(hObject, eventdata, handles)
% hObject    handle to ppmStatsData (see GCBO)
% eventdata  reserved - to be defined in a future version of MATLAB
% handles    empty - handles not created until after all CreateFcns called

% Hint: popupmenu controls usually have a white background on Windows.
%       See ISPC and COMPUTER.
if ispc && isequal(get(hObject,'BackgroundColor'), get(0,'defaultUicontrolBackgroundColor'))
   set(hObject,'BackgroundColor','white');
end


% --- Executes when selected object is changed in panFigDim.
function panFigDim_SelectionChangeFcn(hObject, eventdata, handles)
% hObject    handle to the selected object in panFigDim
% eventdata  structure with the following fields (see UIBUTTONGROUP)
%   EventName: string 'SelectionChanged' (read only)
%   OldValue: handle of the previously selected object or empty if none was selected
```

```
%   NewValue: handle of the currently selected object
% handles    structure with handles and user data (see GUIDATA)

switch get(eventdata.NewValue,'Tag') % Get Tag of selected object.
    case 'rdbOneDim'
        % Code for when radiobutton1 is selected.
        figDim=1;
        set(handles.ppmXAxis,'Enable','on');
        set(handles.ppmYAxis,'Enable','off');
        set(handles.ppmZAxis,'Enable','off');

        set(handles.ppmSelectDraw,'Visible','off');
    case 'rdbTwoDim'
        % Code for when radiobutton2 is selected.
        figDim=2;
        set(handles.ppmXAxis,'Enable','on');
        set(handles.ppmYAxis,'Enable','on');
        set(handles.ppmZAxis,'Enable','off');
        set(handles.ppmSelectDraw,'Visible','off');
    case 'rdbThreeDim'
        % Code for when togglebutton1 is selected.
        set(handles.ppmXAxis,'Enable','on');
        set(handles.ppmYAxis,'Enable','on');
        set(handles.ppmZAxis,'Enable','on');

        set(handles.ppmSelectDraw,'Visible','on');
        figDim=3;
    otherwise
        figDim=1;
        set(handles.ppmXAxis,'Enable','on');
        set(handles.ppmYAxis,'Enable','off');
        set(handles.ppmZAxis,'Enable','off');
        % Code for when there is no match.
end
handles.figDim = figDim;

% Update handles structure
guidata(hObject, handles);


% --- Executes when selected object is changed in panAxes.
function panAxes_SelectionChangeFcn(hObject, eventdata, handles)
% hObject    handle to the selected object in panAxes
% eventdata  structure with the following fields (see UIBUTTONGROUP)
%   EventName: string 'SelectionChanged' (read only)
%   OldValue: handle of the previously selected object or empty if none was selected
%   NewValue: handle of the currently selected object
% handles    structure with handles and user data (see GUIDATA)

switch get(eventdata.NewValue,'Tag') % Get Tag of selected object.
    case 'rdbAxes1'
```

```
        % Code for when radiobutton1 is selected.
        figAxes=1;
    case 'rdbAxes2'
        % Code for when radiobutton2 is selected.
        figAxes=2;
    otherwise
        figAxes=1;
        % Code for when there is no match.
end
 handles.figAxes = figAxes;

% Update handles structure
guidata(hObject, handles);


% --- Executes on button press in ckbAvgData.
function ckbAvgData_Callback(hObject, eventdata, handles)
% hObject    handle to ckbAvgData (see GCBO)
% eventdata  reserved - to be defined in a future version of MATLAB
% handles    structure with handles and user data (see GUIDATA)

% Hint: get(hObject,'Value') returns toggle state of ckbAvgData


% --- Executes during object creation, after setting all properties.
function axes1_CreateFcn(hObject, eventdata, handles)
% hObject    handle to axes1 (see GCBO)
% eventdata  reserved - to be defined in a future version of MATLAB
% handles    empty - handles not created until after all CreateFcns called

% Hint: place code in OpeningFcn to populate axes1


% ------------------------------------------------------------------
function plot_ax2_Callback(hObject, eventdata, handles)
% hObject    handle to plot_ax2 (see GCBO)
% eventdata  reserved - to be defined in a future version of MATLAB
% handles    structure with handles and user data (see GUIDATA)

% Create a figure to receive this axes' data
axes2fig = figure;
% Copy the axes and size it to the figure
axes2copy = copyobj(handles.axes2,axes2fig);
set(axes2copy,'Units','Normalized',...
            'Position',[0.12,.20,.80,.65])
% Assemble a title for this new figure
%str = [get(handles.panAxes1,'Title') ' for ' ...
%       get(handles.sellabel,'String')];

str = [ get(handles.txtFileName,'String')];
```

```
title(str,'Fontweight','bold')
% Save handles to new fig and axes in case
%  we want to do anything else to them
handles.axes1fig = axes2fig;
handles.axes1copy = axes2copy;
guidata(hObject,handles);


% --------------------------------------------------------------------
function plot_ax1_Callback(hObject, eventdata, handles)
% hObject    handle to plot_ax1 (see GCBO)
% eventdata  reserved - to be defined in a future version of MATLAB
% handles    structure with handles and user data (see GUIDATA)
% Create a figure to receive this axes' data
axes1fig = figure;
% Copy the axes and size it to the figure
axes1copy = copyobj(handles.axes1,axes1fig);
set(axes1copy,'Units','Normalized',...
            'Position',[0.12,0.2,.80,.65])
% Assemble a title for this new figure
%str = [get(handles.panAxes1,'Title') ' for ' ...
 str = [ get(handles.txtFileName,'String') ];

title(str,'Fontweight','bold')

% Save handles to new fig and axes in case
% we want to do anything else to them
handles.axes1fig = axes1fig;
handles.axes1copy = axes1copy;
guidata(hObject,handles);

% --------------------------------------------------------------------
function plot_axes1_Callback(hObject, eventdata, handles)
% hObject    handle to plot_axes1 (see GCBO)
% eventdata  reserved - to be defined in a future version of MATLAB
% handles    structure with handles and user data (see GUIDATA)


% --------------------------------------------------------------------
function Plot_axes2_Callback(hObject, eventdata, handles)
% hObject    handle to Plot_axes2 (see GCBO)
% eventdata  reserved - to be defined in a future version of MATLAB
% handles    structure with handles and user data (see GUIDATA)


% --- Executes on selection change in ppmSelectDraw.
function ppmSelectDraw_Callback(hObject, eventdata, handles)
% hObject    handle to ppmSelectDraw (see GCBO)
% eventdata  reserved - to be defined in a future version of MATLAB
% handles    structure with handles and user data (see GUIDATA)
```

```
% Hints: contents = cellstr(get(hObject,'String')) returns ppmSelectDraw contents as cell array
%        contents{get(hObject,'Value')} returns selected item from ppmSelectDraw


% --- Executes during object creation, after setting all properties.
function ppmSelectDraw_CreateFcn(hObject, eventdata, handles)
% hObject    handle to ppmSelectDraw (see GCBO)
% eventdata  reserved - to be defined in a future version of MATLAB
% handles    empty - handles not created until after all CreateFcns called

% Hint: popupmenu controls usually have a white background on Windows.
%       See ISPC and COMPUTER.
if ispc && isequal(get(hObject,'BackgroundColor'), get(0,'defaultUicontrolBackgroundColor'))
    set(hObject,'BackgroundColor','white');
end
```

# REFERENCES


1. Service, R.F., *New probes open windows on gene expression, and more.* Science, 1998. **280**(15 May): p. 1010-1011.
2. Service, R.F., *Scanners get a fix on lab animals.* Science, 1999. **286**(17 December): p. 2261-2263.
3. Massoud, T.F., and Gambhir, S.S.,, *Molecular Imaging in living subjects: seeing fundamental biological processes in a new lightq.* Genes and Development, 2003. **17**: p. 545-580.
4. Weissleder R., a.M., U.,, *Molecular Imaging.* Radiology, 2001. **219**(2): p. 316-333.
5. Balaban, R.S.a.H., V.A.,, *Challenges in Small Animal Noninvasive Imaging.* ILAR Journal, 2001. **42**(3): p. 248-263.
6. Weissleder, R., *Molecular Imaging: Exploring the Next Frontier.* Radiology, 1999. **212**: p. 609-614.
7. Ntziachristos, V., Ripoll, J., Wang, L.V., and Weissleder, R.,, *Looking and listening to light: the evolution of whole-body photonic imaging.* Nature Biotechnology, 2005. **23**(3): p. 313-320.
8. Weissleder R., a.N., V.,, *Shedding ligh onto live molecular targets.* Nature Medicine, 2003. **9**(1): p. 123-128.
9. Contag, C.H., and Bachman, M.H., , *Advances in In Vivo Bioluminescence Imaging of Gene Expression.* Annu. Rev. Biomed. Eng., 2002. **4**: p. 235-260.
10. Weissleder, R., *A clearer vision for in vivo imaging.* Nat. Biotechnol., 2001. **19**: p. 316-317.
11. Weissleder, R., *Scaling down imaging: molecular mapping of cancer in mice.* Nature Reviews, 2002. **2**(January).
12. Herranz, M. and A. Ruibal, *Optical Imaging in Breast Cancer Diagnosis: The Next Evolution.* Journal of Oncology, 2012. **2012**: p. 10.
13. Wessels, J.T.e.a., *In Vivo imaging in experimental preclinical tumor research - a review.* Cytometry Part A, 2007. **71A**: p. 542-549.
14. Cheong, W.F., S.A. Prahl, and A.J. Welch, *A review of the optical properties of biological tissues.* IEEE J Quantum Elect, 1990. **26**: p. 2166-2185.
15. Wang, L.V., *Ultrasound-mediated biophotonic imaging: A review of acousto-optical tomography and photo-acoustic tomography.* Disease Markers, 2003,2004. **19**: p. 123-138.
16. Ku, G., et al., *Thermoacoustic and photoacoustic tomography of thick biological tissues toward breast imaging.* Technol Cancer Res Treat, 2005. **4**(5): p. 559-66.
17. Ku, G. and L.V. Wang, *Deeply penetrating photoacoustic tomography in biological tissues enhanced with an optical contrast agent.* Opt Lett, 2005. **30**(5): p. 507-9.
18. Ku, G., et al., *Multiple-bandwidth photoacoustic tomography.* Phys Med Biol, 2004. **49**(7): p. 1329-38.
19. Ku, G., et al., *Imaging of tumor angiogenesis in rat brains in vivo by photoacoustic tomography.* Appl Opt, 2005. **44**(5): p. 770-5.
20. Leutz, W., and G. Maret, *Ultrasonic Modulation of Multiply Scatterd light,.* Physica B, 1995. **204**: p. 14-19.
21. Li, P.C., et al., *Photoacoustic imaging of multiple targets using gold nanorods.* IEEE Trans Ultrason Ferroelectr Freq Control, 2007. **54**(8): p. 1642-7.
22. Mahan, G.D., W.E. Engler, J.J. Tiemann, and E. Uzgiris, *Ultrasonic Tagging of Light: Theory.* Proc Natl Acad Sci U S A, 1998. **95**: p. 14015-14019.

23. Marks, F.A., Tomlinson, H.W., and Brooksby, G.W. *A comprehensive approach to breast cancer detection using light: photon localization by ultrasound modulation and tissue characterization by spectral discrimination.* in *Proceedings of SPIE Photon Migration and Imaging in Random Media and Tissues, B.* 1993.
24. Rosencwaig, A., *Photoacoustics and Photoacoustic Spectroscopy*. 1980: J. Wiley & sons.
25. Wang, L., Jacques, S.L., and Zhao, X.M., *Continuous-wave ultrasonic modulation of scattered laser light to image objects in turbid media.* Optics Letters, 1995. **20**: p. 629-631.
26. Wang, L., et al., *Combined photoacoustic and molecular fluorescence imaging in vivo.* Conf Proc IEEE Eng Med Biol Soc, 2005. **1**: p. 190-2.
27. Wang, L.V., and Hsin-i Wu, *Biomedical Optics: Principles and Imaging*. 2007, Hoboken: John Wiley & Sons.
28. Wang, X., et al., *Noninvasive photoacoustic angiography of animal brains in vivo with near-infrared light and an optical contrast agent.* Opt Lett, 2004. **29**(7): p. 730-2.
29. Wang, X., et al., *Noninvasive laser-induced photoacoustic tomography for structural and functional in vivo imaging of the brain.* Nat Biotechnol, 2003. **21**(7): p. 803-6.
30. Wang, X., et al., *Photoacoustic tomography of biological tissues with high cross-section resolution: reconstruction and experiment.* Med Phys, 2002. **29**(12): p. 2799-805.
31. Xu, M.a.W., L., *Photoacoustic Imaging in Biomedicine.* Review of Scientific Instruments, 2006. **77**: p. 22.
32. Bell, A., *Production of Sound by Radiant Energy.* Manufacturer and Builder, 1881. **13**(3): p. 2.
33. Patel, C.K.N.a.T., A.C., *Pulsed optoacoustic spectroscopy of condensed matter.* Review of Modern Physics, 1981. **53**(3): p. 517-550.
34. West, G.A., *Photoacoustic Spectroscopy.* Review of Scientific Instruments, 1983. **54**(7): p. 21.
35. Hutchins, D.A.a.T., A.C., *Pulsed photoacoustic materials characterization.* IEEE Trans Ultrason Ferroelectr Freq Control, 1986. **33**(5): p. 21.
36. Tam, A.C., *Applications of Photoacoustic sensing techniques.* Review of Modern Physics, 1986. **58**(2): p. 50.
37. Sigcrist, M.W., Journal of Applied Physics, 1986. **60**(7): p. R83-R122.
38. Zharov, V.P.a.V.S.L., *Laser Optoacoustic Spectroscopy*. Springer Series in Optical Science. Vol. 37. 1986, New York: Springer-Verlag.
39. Mandelis, A., ed. *Principles and Perspectives of Photothermal and Photoacoustic Phenomena*. 1992, Elsevier Science: New York.
40. Michaelian, K.H., *Photoacoustic Infrared Spectroscopy*. 2003, Hoboken, NJ: Wiley-Interscience.
41. Mclelland, J.F., Jones, R.W., and Bajic, S.J. , *Photoacoustic Spectroscopy*, in *Handbook of Vibrational Spectroscopy*, J.M.a.G. Chalmers, P.R., Editor. 2002, Wiley: New York.
42. Gusev, V.E.a.K., A.A., *Laser Optoacoustics*. 1993, New York: AIP.
43. *Biomedical Optoacoustics*. in *Proceedings of SPIE*. 2000.
44. *Biomedical Optoacoustics II*. in *Proceedings of SPIE*. 2001. San Jose, CA, USA.
45. *Biomedical Optoacoustics III*. in *Proceedings of SPIE*. 2002. San Jose, CA.
46. *Biomedical Optoacoustics IV*. in *Proceedings of SPIE*. 2003. San Jose, CA.
47. *Photons Plus Ultrasound: Imaging and Sensing*. in *Proceedings of SPIE*. 2004. San Jose, Ca.
48. *Photons Plus Ultrasound: Imaging and Sensing 2005: The Sixth Conference on Biomedical Thermoacoustics, Optoacoustics, and Acousto-optics*. in *Proceedings of SPIE*. 2005. San Jose, CA.

49. Wang, L. and S. Hu, *Photoacoustic Tomography: In vivo imaging from organelles to organs.* Science, 2012. **335**: p. 1458-1462.
50. Li, C. and L.V. Wang, *Photoacoustic tomography and sensing in biomedicine.* Phys Med Biol, 2009. **54**(19): p. R59-97.
51. Wang, Y. and L.V. Wang, *Forster resonance energy transfer photoacoustic microscopy.* J Biomed Opt, 2012. **17**(8): p. 086007.
52. Ermilov, S.A., et al. *Real-Time optoacoustic imaging of breast cancer using an interleaved two laser imaging system coregistered with ultrasound*. in *Photons Plus Ultrasound: Imaging and Sensing 2010*. 2010. San Francisco, CA.
53. Xia, W., et al., *Design and evaluation of a laboratory prototype system for 3D photoacoustic full breast tomography.* Biomedical Optics Express, 2013. **4**(11): p. 2555-2569.
54. Krishnan, K., *A theory for the ultrasonic modulation of incoherent light in turbid medium*, in *Proceedings of SPIE*. 2005.
55. Yuan, B., Gamelin, J., and Zhu, Q.,, *Mechanisms of the ultrasonic modulation of fluorescence in turbid media.* Journal of Applied Physics, 2008. **104**(10).
56. Kobayashi, M., *Fluorescence tomography in turbid media based on acousto-optic modulation imaging.* Applied Physics Letters, 2006. **89**.
57. Kobayashi, M. *Fluorescence Tomography of Biological Tissue Based on Ultrasound Tagging Technique*. in *Proceedings of SPIE- OSA Biomedical Optics*. 2007.
58. Hall, D., *Quadrature Detection of Ultrasound-Modulated Photons in a Gain-Modulated, Image-Intensified, CCD Camera.* The Open Optics Journal, 2008. **2**: p. 75-78.
59. Yuan, B., *Ultrasound-modulated fluorescence based on a fluorophore-quencher-labeled microbubble system.* Journal of Biomedical Optics, 2009. **14**(2): p. 024043.
60. Yuan, B., *Sensitivity of fluorophore-quencher labeled microbubbles to externally applied static pressure.* Medical Physics, 2009. **36**(8): p. 3455-3469.
61. Yuan, B.H., et al., *Microbubble-enhanced ultrasound-modulated fluorescence in a turbid medium.* Applied Physics Letters, 2009. **95**(18): p. 3.
62. Yuan, Y.L.a.B. *Do large fluroescent particles enhance the modulation efficiency of ultrasound-modulated fluorescence?* in *Proc. of SPIE*. 2011.
63. Hergert, W., and T. Wriedt, ed. *The Mie Theory: Basics and Applications*. 2012, Springer.
64. Laugier, P., and G. Haïat, ed. *Bone Quantitative Ultrasound*. Vol. XII. 2011. 468.
65. Brillouin, L., *Diffusion de la lumière et des rayonnes X par un corps transparent homogène: influence de l'agitation thermique.* Ann. Phys, 1922. **17**: p. 88-122.
66. Korpel, A., *Acousto-Optics: A Review of Fundamentals.* Proc. IEEE, 1981. **69**(1): p. 48-53.
67. Raman, C.V., and N.S. Nath, *The diffraction of light by high frequency sound waves.* Proc Ind. Acad. Sci., 1935. **2**: p. 406-420.
68. Raman, C.V., and N.S. Nath, *The diffraction of light by high frequency sound waves.* Proc Ind. Acad. Sci., 1936. **3**: p. 75-84.
69. Raman, C.V., and N.S. Nath, *The diffraction of light by high frequency sound waves.* Proc Ind. Acad. Sci., 1936. **3**: p. 119-125.
70. Raman, C.V., and N.S. Nath, *The diffraction of light by high frequency sound waves.* Proc Ind. Acad. Sci., 1936. **3**: p. 459-465.
71. Klein, W.R., and B.D. Cook, *Unified approach to ultrasonic light diffraction.* IEEE Trans. Sonics Ultrason., 1967. **SU-14**: p. 723-733.
72. Moharam, M.G., and L. Young, *Criterion for Bragg and Raman-Nath Diffraction Regimes.* Appl Opt, 1978. **17**(11): p. 1757-1759.
73. Wang, L.V., *Mechanisms of Ultrasonic Modulation of Multiply Scattered Coherent Light: An Analytical Model.* Phys Rev Letters, 2001. **87**(4).

74. Kempe, M., *Acousto-Optic tomography with multiply scattered light.* J. Opt. Soc. Am. A, 1997. **14**(5): p. 1151-1158.
75. Wang, L.V., and X. Zhao, *Ultrasound-modulated optical tomography of absorbing objects buried in dense tissue-simulating turbid media.* Appl Opt, 1997. **36**(26): p. 7277-7282.
76. Bal, G., and J.C. Schotland, *Inverse Scattering and Acousto-Optic Imaging.* Phys Rev Letters, 2010. **104**.
77. Liu, Q., Norton, S., and Vo-Dinh, T., , *Modeling of nonphase mechanisms in ultrasonic modulation of light propagation.* Applied Optics, 2008. **47**(20): p. 3619-3630.
78. Yuan, B. and Y. Liu, *Ultrasound-modulated fluorescence from rhodamine B aqueous solution.* Journal of Biomedical Optics, 2010. **15**(2): p. 021321-6.
79. Mei, R., *Velocity fidelity of flow tracer particles.* Experiments in Fluids, 1996. **22**(1).
80. Guz, A.N., and A.P. Zhuk, *Motion of solid particles in a liquid under the action of an acoustic field: the mechanism of radiation pressure.* Int. Appl. Mech., 2004. **40**: p. 246-265.
81. Aboobaker, N., D. Blackmore, and J. Meegoda, *Mathematical modeling of the movement of suspended particles subjected to acoustic and flow fields.* Applied Mathematical Modeling, 2005. **29**(6): p. 515-532.
82. Wiklund, M., J. Toivonen, M. Tirri, P. Hanninen, and H.M. Hertz, *Ultrasonic enrichment of microspheres for ultrasensitive biomedical analysis in confocal laser-scanning fluorescence detection.* J. Appl. Phys., 2004. **96**(2).
83. Yasuda, K., and T. Kamakura, *Acoustic radiation force on micrometer-size particles.* Appl Phys Ltrs, 1997. **71**(13).
84. Matsukawa, M., T. Akimoto, S. Ueba, and T. Otani, *Ultrasonic wave properties in the particle compounded agarose gels.* Ultrasonics, 2002. **40**(1-8): p. 323-327.
85. Hall, D., *Feasibility of Dual Optics/Ultrasound Imaging and Contrast Media for the detection and characterization of Prostate Cancer*. 2008, U.S. Army Medical Research and Material Command: University of California.
86. Hall, D.J., et al. *Detection of ultrasound-modulated photons and enhancement with ultrasound microbubbles*. 2009. SPIE.
87. Leutz, W.a.M., G., *Ultrasonic Modulation of Multiply Scatterd light,.* Physica B, 1995. **204**: p. 14-19.
88. Dolfi, D., Micheron, F., *Imaging Process and System for Transillumination with Photon Frequency Marking*, USPTO, Editor. 1989: United States.
89. Olympus-NDT *Ultrasonic Transducers Technical Notes*. 2006.
90. Garetz, J.M.K.a.B.A., *Measurement of a Gaussian laser beam diameter through the direct inversion of knife-edge data.* Appl Opt, 1983. **22**(21): p. 3406-3410.
91. Latham, P., Morita, Y., Massa, N., and Jeong, T. *Photodetector Characteristics*. 1999.
92. Ready, J., *Optical Detectors and Human Vision*, in *Fundamentals of Photonics*.
93. Division, N.C.S.T.a.S., *Telecommunications Glossary of Telecommunication Terms*, in *Federal Standard 1037C- Noise Equivalent Power*. 1996.
94. Saleh, B.E., and Teich, M., , *Fundamentals of Photonics*. 1991, New York: John Wiley & Sons, Inc. .
95. T. Q. Duc, S.K., and M. Kobayashi.,, *Development of Ultrasonic Modulation Probe for Fluorescence Tomography Based on Acousto-Optic Effect.* International Journal of Optics, 2011. **2011**.
96. Frangioni, J.V.e.a., *Tissue-like phantoms for near-infrared fluorescence imaging system assessment and the training of surgeons.* Journal of Biomedical Optics, 2006. **11**(1).
97. Mahan, G.D., Engler, W.E., Tiemann, J.J., and Uzgiris, E.,, *Ultrasonic Taggin of Light: Theory.* Proc Natl Acad Sci U S A, 1998. **95**: p. 14015-14019.

98. Gamelin, J., et al., *A real-time photoacoustic tomography system for small animals.* Optics Express, 2009. **17**(13): p. 10489-10498.
99. Zackrisson, S., S.M.W.Y. van de Ven, and S.S. Gambhir, *Light In and Sound Out: Emerging Translational Strategies for Photoacoustic Imaging.* Cancer Research, 2014. **74**(4): p. 979-1004.
100. Wang, L.V. and S. Hu, *Photoacoustic Tomography: In Vivo Imaging from Organelles to Organs.* Science, 2012. **335**(6075): p. 1458-1462.
101. Raman, C.V., and N.S. Nath, *The diffraction of light by high frequency sound waves: Part I.* Proc Ind. Acad. Sci., 1935. **2**: p. 406-420.
102. Raman, C.V. and N.S. Nagendra Nath, *The diffraction of light by sound waves of high frequency: Part II.* Proceedings of the Indian Academy of Sciences - Section A, 1935. **2**(4): p. 413-420.
103. Raman, C.V., and N.S. Nath, *The diffraction of light by high frequency sound waves: Part III.* Proc Ind. Acad. Sci., 1936. **3**: p. 75-84.
104. Raman, C.V., and N.S. Nath, *The diffraction of light by high frequency sound waves: Part IV.* Proc Ind. Acad. Sci., 1936. **3**: p. 119-125.
105. Raman, C.V., and N.S. Nath, *The diffraction of light by high frequency sound waves: Part V.* Proc Ind. Acad. Sci., 1936. **3**: p. 459-465.
106. Debye, P. and F.W. Sears, *On the Scattering of Light by Supersonic Waves.* Proceedings of the National Academy of Sciences, 1932. **18**(6): p. 409-414.
107. Bragg, W.L., *The diffraction of short electromagnetic waves by a crystal.* Proceedings of the Cambridge Philosophical Society, 1913. **17**: p. 43-57.
108. Lucas, R. and P. Biquard, *Propriétés optiques des milieux solides et liquides soumis aux vibrations élastiques ultra sonores.* J. Phys. Radium, 1932. **3**(10): p. 464-477.
109. Berry, M.V., *The diffraction of light by ultrasound*. 1966, New York: Academic Press.
110. Wang, L.V., *Mechanisms of ultrasonic modulation of multiply scattered coherent light: a Monte Carlo model.* Optics Letters, 2001. **26**(15): p. 1191-1193.
111. Kobayashi, M., et al., *Fluorescence tomography in turbid media based on acousto-optic modulation imaging.* Applied Physics Letters, 2006. **89**(18): p. 181102.
112. Kobayashi, M., et al. *Fluorescence Tomography of Biological Tissue Based on Ultrasound Tagging Technique*. in *Biophotonics 2007: Optics in Life Science*. 2007. Munich, Germany: Optical Society of America.
113. Huynh, N.T., et al., *Ultrasound modulated imaging of luminescence generated within a scattering medium.* J Biomed Opt, 2013. **18**(2): p. 20505.
114. Lévêque, S., et al., *Ultrasonic tagging of photon paths in scattering media: parallel speckle modulation processing.* Optics Letters, 1999. **24**(3): p. 181-183.
115. Wang, L.V., *Ultrasound mediated biophotonic imaging A review of acousto-optical tomography and phot-acosutic tomography.* Disease Markers, 2004. **19**: p. 123-138.
116. Bossy, E., et al., *Transient optoelastography in optically diffusive media.* Applied Physics Letters, 2007. **90**(17): p. -.
117. Bossy, E., et al. *Imaging of optically diffusive media by use of opto-elastography*. 2007.
118. Li, R., et al., *Effects of acoustic radiation force and shear waves for absorption and stiffness sensing in ultrasound modulated optical tomography.* Optics Express, 2011. **19**(8): p. 7299-7311.
119. Li, S., et al., *Tracking shear waves in turbid medium by light: theory, simulation, and experiment.* Optics Letters, 2014. **39**(6): p. 1597-1600.
120. Jensen, H.W., et al., *A practical model for subsurface light transport*, in *Proceedings of the 28th annual conference on Computer graphics and interactive techniques*. 2001, ACM. p. 511-518.

121. Frisvad, J.R., et al., *Computing the scattering properties of participating media using Lorenz-Mie theory*, in *ACM SIGGRAPH 2007 papers*. 2007, ACM: San Diego, California. p. 60.
122. Sandell, J.L. and T.C. Zhu, *A review of in-vivo optical properties of human tissues and its impact on PDT.* Journal of Biophotonics, 2011. **4**(11-12): p. 773-787.
123. Jacques, S.L., *Optical properties of biological tissues: a review.* Phys. Med. Biol., 2013. **58**(11): p. R37-R61.
124. Resink, S.G., A.C. Boccara, and W. Steenbergen, *State-of-the art of acousto-optic sensing and imaging of turbid media.* J Biomed Opt, 2012. **17**(4): p. 040901.
125. Karu, T.I., ed. *Low power laser therapy*. Biomedical Photonics Handbook, ed. T. Vo-Dinh. 2003, CRC Press: Boca Raton.
126. Yuan, B., J. Gamelin, and Q. Zhu, *Mechanisms of the ultrasonic modulation of fluorescence in turbid media.* J Appl Phys, 2008. **104**(10): p. 103102.
127. Cobbold, R.S.C., *Foundations of Biomedical Ultrasound*. 2007, New York: Oxford University Press, Inc.
128. Smith, R.C. and K.S. Baker, *Optical properties of the clearest natural waters (200?800 nm).* Applied Optics, 1981. **20**(2): p. 177-184.
129. Brillouin, L., *La Diffraction de la Lumiere par des Ultra sons".* Atual. Sci. Ind., 1933. **59**.
130. Korpel, A., *Acousto-Optics*. Optical Engineering, ed. B.J. Thompson. 1988, New York, NY: Marcel Dekker, Inc.
131. Schiebener, P., et al., *Refractive index of water and steam as function of wavelength, temperature and density.* Journal of Physical and Chemical Reference Data, 1990. **19**(3): p. 677-717.
132. Benchimol, M.J., et al., *Phospholipid/carbocyanine dye-shelled microbubbles as ultrasound-modulated fluorescent contrast agents.* Soft Matter, 2013. **9**(8): p. 2384-2388.
133. Yuan, B. *Ultrasound-switchable fluorescence imaging*. in *Optics in the Life Sciences*. 2013. Waikoloa Beach, Hawaii: Optical Society of America.
134. Pei, Y., et al., *High resolution imaging beyond the acoustic diffraction limit in deep tissue via ultrasound-switchable NIR fluorescence.* Sci. Rep., 2014. **4**.
135. Bingbing, C., et al., *Development of Ultrasound-Switchable Fluorescence Imaging Contrast Agents Based on Thermosensitive Polymers and Nanoparticles.* Selected Topics in Quantum Electronics, IEEE Journal of, 2014. **20**(3): p. 67-80.
136. Hill, C.R., Bamber, J.C., and ter Haar, G.R.,, ed. *Physical Principles of Medical Ultrasonics*. Second Edition ed. 2004, John Wiley & Sons Ltd.
137. Marinesco, N.a.T., J.J., *Action of supersonic waves upon the photographic plate.* Pro. R. Acad. Sci, 1933. **196**: p. 856-860.
138. Frenzel, H., and Schultes, H.,, *Lumineszenz im ultraschallbeschichten Wasser.* Z. Physik. Chem., 1934. **27B**: p. 421-424.
139. Putterman, S.J., and Weninger, K.R.,, *Sonoluminescence: How bubbles turn sound into light.* Annu. Rev. Biomed. Eng., 2000. **32**: p. 445-476.
140. Oncley, L.A.P.a.P.B., *Detection of Ultrasound with Phosphorescent Materials.* Transactions of the IRE Professional Group on Ultrasonics Engineering, 1956. **4**(1): p. 42-52.
141. Kodama, T., Ohtani, H., Arakawa, H., and Ikai, A., *Mechanical perturbation-induced fluorescent change of green fluorescent protein.* Applied Physics Letters, 2005. **86**.
142. Gao, Q., Tagami, K., Fujihira, M., and Tsukada, M.,, *Quenching Mechanisms of Mechanically Compressed Green Fluorescent Protein Studied by CASSCF/AM1.* Japanese Journal of Applied Physics, 2006. **45**(33): p. L929-L931.
143. Scheyling, C.H.e.a., *Temperature-Pressure Stability of Green Fluorescent Protein: A fourier transform infrared spectroscopy study.* Biopolymers, 2002. **26**: p. 244-253.

144. Medintz, I.e.a., *Quantum Dot Bioconjugates for imaging, labeling and sensing.* Nature Materials, 2005. **4**(June): p. 435-446.
145. SH, T. and A. AP, *High-Pressure Structural Transformations in Semiconductor Nanocrystals.* Annu. Rev. Phys. Chem., 1995. **46**: p. 595-625.
146. SH, T., et al., *Pressure-induced structural transformations in Si nanocrystals: Surface and shape effects.* Phys Rev Lett, 1996. **76**(23): p. 4384-4387.
147. Clegg, R.M., *Fluorescence resonance energy transfer.* Current Opinion in Biotechnology, 1995. **6**(1): p. 103-110.
148. Nielsen, T.e.a., *Compounds and Methods for Combined Optical-Ultrasound Imaging*, U.S.P. Office, Editor. 2008, Koninklijke Philips Electronics, N.V.,: United States.
149. Forster, T., *Intermolecular Energy Migration and Fluorescence.* Ann. Phys, 1948. **2**: p. 55-75.
150. Pham, W., et al., *A near-infrared dye for multichannel imaging.* Chemical Communications, 2008(16): p. 1895-1897.
151. Nickels, M., et al., *Functionalization of iron oxide nanoparticles with a versatile epoxy amine linker.* Journal of Materials Chemistry, 2010. **20**(23): p. 4776-4780.
152. Qin, S., C.F. Caskey, and K.W. Ferrara, *Ultrasound contrast microbubbles in imaging and therapy: physical principles and engineering.* Physics in Medicine and Biology, 2009. ***54***(6).
153. van der Ende, A., et al., *Tailored polyester nanoparticles: post-modification with dendritic transporter and targeting units via reductive amination and thiol-ene chemistry.* Soft Matter, 2009. **5**(7): p. 1417-1425.
154. Ostrovskii, I.V. and O.A. Korotchenkov, *Sonoluminescence effects in ZnS materials.* Journal of Physics and Chemistry of Solids, 2000. **61**(8): p. 1321-1330.
155. Korotchenkov, O.A. and T. Goto, *Sonoluminescence in granular media.* Physical Review B, 1997. **56**(21): p. 13646-13649.
156. Leistner, M. and L. Herforth, *Changes in the Luminescence of Continuously Excited Zinc Sulfide Screens under Ultrasonic Action.* Naturwissenschaften, 1957. **44**(59).
157. Schreiber, H. and W. Degner, *Methods of Making Ultrasonic Waves Visible.* Naturwissenschaften, 1950. **37**(358).
158. Berger, H. and R. Dickens, *A Review of Ultrasonic Imaging Methods with a Selected, Annotated*. 1963, Argonne National Laboratory.